Numerical and Experimental Investigation of Bio-Inspired Robot Propulsion and Manoeuvring

A thesis submitted in fulfilment of the requirements
for the degree of Doctor of Philosophy

By: Marvin Wright

Supervisor: Professor Qing Xiao
2nd Supervisor: Dr Hong Yue
3rd Supervisor: Dr Mark Post

Department of Naval Architecture, Ocean and Marine Engineering
Glasgow G4 0LZ, United Kingdom

Declaration

This thesis is the result of the author's original research. It has been composed by the author and has not been previously submitted for examination, which has led to the award of a degree. The copyright of this thesis belongs to the author under the terms of the United Kingdom Copyright Acts as qualified by University of Strathclyde Regulation 3.51. Due acknowledgement must always be made of the use of any material contained in, or derived from, this thesis.

Name: Marvin Wright Date: 29/02/2024

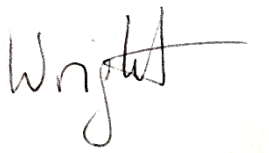

Acknowledgements

My heartfelt gratitude goes to my first supervisor Professor Qing Xiao for her personal and professional guidance. I deeply appreciate her continuous support and all the opportunities she has provided me with as part of, and beyond, my PhD studies. I would also like to extend my gratitude to my second and third supervisors, Dr Hong Yue and Dr Mark Post, for their invaluable guidance and encouragement.

I would like to extend my deepest thanks to Verlume Ltd and the University of Strathclyde John Anderson Research Award for making this PhD pursuit possible through their generous financial support.

A special mention goes to members of the Kelvin Hydrodynamics Laboratory: Dr Saishuai Dai for his friendship and invaluable advice, as well as technicians Steven Black, Grant Dunning and Bill Wright for their indispensable assistance during lab testing. I would also like to thank Professor Qiang Zhu at UC San Diego for his guidance and contributions to our joint research as well as current and former research group colleagues Dr Wendi Liu, Dr Guangyu Shi, Dr Zhao Zhenkai, Dr Zhou Yang, Dr Luo Yang, Dr Yang Huang, Xiang Li and Zhongsheng Deng.

I want to express my special appreciation to my friends at the university Dr Prapatsorn Wejprasit and Dr Pitpimon Choorod for their limitless and loyal friendship.

I am also grateful to my friends and colleagues at the department of Naval Architecture, Ocean and Marine Engineering: Alexander Senss, Dr Hongbo Hour, Dr Mohammed Baba Shehu, Dr Onder Canbulat, Huang Yi and many others who I had the pleasure of meeting during this PhD journey.

I would like to further acknowledge the cleaning, security, administrative and IT staff at the university. Their dedication allows the university to function seamlessly, enabling research staff and students to focus on their academic pursuits.

Finally, I would like to thank my family, my mother and father, sister Louise and brother Christopher who have always supported me - thank you for everything. My time in Glasgow has been one of the best times of my life, I would like to thank my Glasgow aunties, Maggie, Liz and Dot as well as Gordon and Max for making me feel at home.

List of publication and research output

M Wright, Q Xiao, and Q Zhu. “Hydrodynamics and control of Body Caudal Fin manoeuvring.”, *Transactions of the Japan Society for Computational Engineering and Science* (2024) (Submitted to Journal on 26/02/2024).

M Wright, Q Xiao, and Q Zhu. “Combined hydrodynamic and control analysis on optimal kinematic parameters for bio-inspired autonomous underwater vehicle manoeuvring.”, *Frontiers in Physics*11 (2023).
DOI: 10.3389/fphy.2023.1220596

M Wright, Q Xiao, S Dai, M Post, H Yue, B Sarkar “Design and development of modular magnetic bio-inspired autonomous underwater robot–MMBAUV.”, *Ocean Engineering* 273 (2023): 113968.
DOI: 10.1016/j.oceaneng.2023.113968

Y Luo, **M Wright**, Q Xiao, H Yue, G Pan. “Fluid–structure interaction analysis on motion control of a self-propelled flexible plate near a rigid body utilizing PD control.”, *Bioinspiration & Biomimetics* 16.6 (2021): 066002.
DOI: 10.1088/1748-3190/ac1cee

Conference Publications

M Wright, W Gorma, Y Luo, M Post, Q Xiao, A Durrant et al. “Multi-actuated AUV body for windfarm inspection: lessons from the bioinspired RoboFish field trials.”, *2020 IEEE/OES Autonomous Underwater Vehicles Symposium (AUV)*. IEEE, 2020.
DOI: 10.1109/AUV50043.2020.9267931

M Wright, Y Luo, Q Xiao, M Post, W Gorma, A Durrant, H Yue et al. “CFD-FSI analysis on motion control of bio-inspired underwater AUV system utilizing PID control.”, *2020 IEEE/OES Autonomous Underwater Vehicles Symposium (AUV)*. IEEE, 2020.
DOI: 10.1109/AUV50043.2020.9267933

Poster, presentation and awards

M Wright, Q Xiao, S Dai, M Post, H Yue, B Sarkar. “Modular magnetic bio-inspired autonomous underwater vehicle.”, Poster at *The European Robotics Forum 2023 (ERF2023)*. 2023.

M Wright, Q Xiao. “Modelling and control of bio-inspired autonomous underwater vehicles.”, Keynote presentation at Computational Fluid Conference (CFC) 2023, Cannes, France.

M Wright. Award Finalist for Future Game Changer Award at the British Renewable Energy Awards 2023 hosted by Supergen Offshore Renewable Energy Hub, Supergen Bioenergy Hub Network & The Association for Renewable Energy & Clean Energy (REA)

Patent

M Wright, Q Xiao, “University of Strathclyde - Robot Fish” Application number: PCT/GB2023/051804, filing date of 7 July 2023.

Abstract

Continuously growing interest in discovering, developing and exploiting offshore resources requires efficient, reliable and cost-effective robotic operations underwater. To ensure human safety and enable automated robotic intervention of offshore assets, including Inspection, Maintenance and Repair (IMR), future robotic systems will be required to be more efficient, manoeuvrable and resilient. Bio-inspired underwater vehicles are designed to mimic the excellent swimming abilities of natural swimmers.

To enhance the understanding and implementation of bio-inspired locomotion and to address gaps in the knowledge of bio-inspired locomotion hydrodynamics, control and robotic design, this thesis investigates several key aspects relating to the propulsion, manoeuvrability and power of Body Caudal Fin (BCF) locomotion by means of numerical simulations, prototype design and hydrodynamic lab testing. This thesis is organised in two parts: numerical studies and experimental investigations.

Numerical simulations are established through coupling a numerical fluid solver, a body dynamics model and feedback control. A single-body and a multi-body fish model, which are implemented within User Define Functions (UDF) and coupled to Ansys Fluent, are presented in detail and reference is given to a Fluid Structure Interaction (FSI) solver used to simulate elastic structures. Linear feedback control is represented by means of a Proportional, Integral and Derivative (PID) control algorithm. Adding linear feedback control to CFD simulations makes it possible to simulate unsteady swimming manoeuvres at a set point and make a comparison across parameter spaces under quasi-steady state conditions.

Three control strategies are derived by defining feedback control error logics that are applied in three numerical studies. The first investigation focusses on optimal curvature distribution of a manoeuvring BCF swimmer. Results show energetic benefit for swimmers turning with greater body curvature towards the tail. The second numerical simulation considers the thrust performance of a fixed and pitching elastic plate of different material stiffnesses and pitching frequencies over a parameter space. The results provide insights into the instantaneous hydrodynamics and thrust performance of flexible appendages, such as a BCF and the differences in performance for various material properties and actuation parameters. The third numerical

investigation studies the energetic performance of an actuated elastic plate swimming in front of a cylinder while holding its position. The results identify any interaction between a freely moving plate and a cylinder as well as the energetic benefit of smaller distances towards the low-pressure zone at the leading edge of the cylinder.

The experimental part of the thesis introduces a new modular robotic design that incorporates a novel approach to achieve static watertight torque couplings and mechanical modularity. The key innovation lies in the application of a synchronous magnetic coupling, which replaces traditional methods, such as dynamic seals and flexible covers used in existing modular robotic designs. This magnetic coupling provides a sole magnetic connection between neighbouring body elements, eliminating the need for mechanical connections between modules and addressing potential weaknesses associated with fixed connections.

The rotational degree of freedom afforded by the magnetic coupling enables the robot to form a traveling body wave within a continuum space, facilitating thrust generation and manoeuvring. All mechanical parts, including the enclosure, shaft and gears, have been custom CAD designed and created through additive manufacturing techniques including Fuse Deposition Modelling (FDM) and Stereolithography (SLA). The untethered robot can move freely in a plane just below the water surface and is controlled through Bluetooth Low Energy (BLE) communications between each module and a central pc.

Extensive hydrodynamic testing has been conducted at Strathclyde University's Kelvin Hydrodynamics Laboratory to confirm the basic swimming abilities of the robot prototype and assess its performance. Two separate investigations of thrust generation and free-swimming performance are conducted. Thrust measurements are taken applying different undulation frequencies and amplitudes with a constant amplitude envelope at a custom-made testing stand. Motion capturing is utilised to record the motion of the robot in three and six degrees of freedom during free-swimming tests. Free-swimming measurements are taken with a constant amplitude envelope of the manoeuvring robot and straight forward swimming velocity with different undulation frequencies and amplitudes. Finally, experimental measurements are compared with the results of a CFD multi-body simulation.

Table of Contents

List of Figures

List of Tables

Nomenclature

i, j, k	Numbering index
$n, n+1, n-1$	Numbering index
$\square^{x}$	Nondimensionalised variable
$\overline{\square}$	Mean value
$\square_0$	Reference variable
$\dot{\square}, \ddot{\square}, \dddot{\square}$	First, second and third time derivative
$\square^{*}$	Chapter 3 Generalised variable Chapter 4 Nondimensionalised value
$\hat{\square}$	Skew matrix of vector
ϕ	Scalar quantity
ρ	Density
S_ϕ	Source term of scalar quantity
V	Volume
$\mathbf{A}$	Face area vector
t	Time
t_s	CFD time step
t_k	Controller sampling time
$\mathrm{t_l}$	Controller update time
$t_{0,1}$	Controller transition time
k_{ij}	Mesh spring stiffness
$\boldsymbol{u_g}$	Mesh node velocity vector
L	Swimmer total length
l	Swimmer body section length

U	Free stream velocity
ν	Kinematic viscosity
$y(t,s)$	Periodic angular or lateral displacement
$A(s)$	Amplitude envelope
f	Frequency
$T = 1/f$	Cycle period
T_h	Selected reference period of plate positioned close to target position
T_s	Time to swim distance L
$\varphi(s)$	Phase distribution
$C(s)$	Curvature envelope
κ	Curvature
$w(s)$	Body node position
w_0, w_1	Body geometry coefficients
dx_s, dy_s	Single body model node displacement increment
x_{cg}, y_{cg}	Single body model total centre of gravity
$x_{s_{cg}} y_{s_{cg}}$	Single body model body section centre of gravity
A	Single body model section area
I	Mass moment of inertia
m	Mass
r	Radius
$\boldsymbol{a} = [a_x, a_y]$	Linear acceleration vector
$\boldsymbol{x} = [u, v]$	Linear displacement vector
α	Angular acceleration

ω	Angular velocity
θ	Angle
$\mathcal{F}$	Multi-body local coordinate frame
B	Multi-body element
a, s, n	Multi-body local coordinate axis
X_e, Y_e	Multi-body global coordinate axis
O_e	Multi-body global coordinate frame
$\boldsymbol{T}$	Transformation matrix
$\boldsymbol{R}$	Rotational matrix
$\boldsymbol{P}$	Position vector
$\boldsymbol{Ad}$	Adjoint operator
$\boldsymbol{X}_{state}$	Current system state vector
$\boldsymbol{Q}$	Quaternion vector
$\boldsymbol{r}$	Joint rotation position vector
$\boldsymbol{\eta}$	Velocity vector
$\mathbf{U}$	Unit vector
$\mathbf{M}$	Body mass tensor matrix
$\mathbf{MS}$	First inertia moment tensor matrix
$\mathbf{I}$	Angular inertia tensor matrix
$\boldsymbol{\mathcal{M}}$	Inertia tensor matrix
$\boldsymbol{\beta}$	Inertial force vector
$\boldsymbol{\zeta}$	Acceleration vector of only velocity elements
$\boldsymbol{F}$	Force vector array
F_x, F_y	Force

M	Moment
E	Young's modulus
K	Dimensionless stiffness
d_0	Distance between swimmer TE and cylinder
z	Distance between magnets
d_e	Magnet force coefficient
L_1, L_2	Magnet dimension
$\mathrm{K_p}$	Proportional gain
K_I	Integral gain
K_D	Derivative gain
c_{control}	Control variable
c_a	Amplitude control variable
c_s	Offset control variable
$e()$	Control error
$c_1, c_2, c_3, c_4, c_5, c_6$	Kinematic coefficients
s_1, s_2, s_3	Joint positions along the robot
c_D	Drag coefficient
c_{D_f}	Friction drag
c_{D_p}	Pressure drag
c_L	Lift coefficient
c_T	Thrust coefficient
c_P	Power coefficient
Re	Reynolds number
St	Strouhal number

CoT	Cost of Travel
CoM	Cost of Manoeuvring
P_{in}	Input Power

Hydrodynamic and performance coefficients

The Reynolds number Re is a non-dimensional coefficient used to predict the flow regime. The Reynolds number is given by

$$Re = \frac{LU}{\nu}. \tag{1.1}$$

The Strouhal number St is a non-dimensional coefficient used in the analysis of unsteady and oscillatory flow. The Strouhal number is given by

$$St = \frac{fA(L)}{U}. \tag{1.2}$$

The Cost of Manoeuvring CoM is a newly introduced dimensional coefficient. It is related to the popular Cost of Travel coefficient and provides information on the energy expenditure per unit rotation and is given by

$$CoM = \frac{\bar{E}}{\theta} = \frac{\overline{P_{in}}}{\omega_{global}} = \frac{\overline{P_{in}}}{\frac{U_s}{r}}. \tag{1.3}$$

The thrust coefficient c_T is used to assess the ability of a system to generate thrust and is given by

$$c_T = -\frac{F_x}{\frac{1}{2}\,\rho_f\,U^2\,L}. \tag{1.4}$$

The power expenditure coefficient assesses the efficiency of a system and its ability to convert input power into thrust. The coefficient is given by

$$c_p = \frac{M_0 \dot{\theta}}{\frac{1}{2}\,\rho_f U^3 L}. \tag{1.5}$$

The overall energy expenditure coefficient c_{Ps} assesses a swimmer's power performance of swimming a defined length L in time T_s. The overall energy expenditure coefficient is defined by

$$c_{Ps} = -\frac{\int_0^{T_s} P_{in} dt}{\frac{1}{2}\rho_f U^2 L}. \tag{1.6}$$

The mean energy expenditure assesses the power performance of a swimmer dynamically holding position around a target position over a period T_h.

$$c_{Ph} = -\frac{\int_t^{t+T_h} P_{in} dt}{T_h \frac{1}{2}\rho_f U^3 L}. \tag{1.7}$$

Chapter 1 Introduction

1.1 Fish swimming

Fish are thought to continuously adapt to their environment through a process of evolution to develop optimal combinations of physique and behaviour more suited to their local conditions. Depending on their usage of median paired fins or body undulation as the main thrust generating mechanism, fish are generally categorized as Median Paired Fin (MPF) type and Body Caudal Fin (BCF) type (Breder, 1926). The two categories differ significantly in terms of which part of the body generates thrust, maintains stability and enables manoeuvrability. These kinematic mechanisms are also reflected in fish physiology, allowing for efficient swimming within their respective environments. BCF represents the largest group with approximately 85% of the fish observed being in this category (Wang et al., 2020).

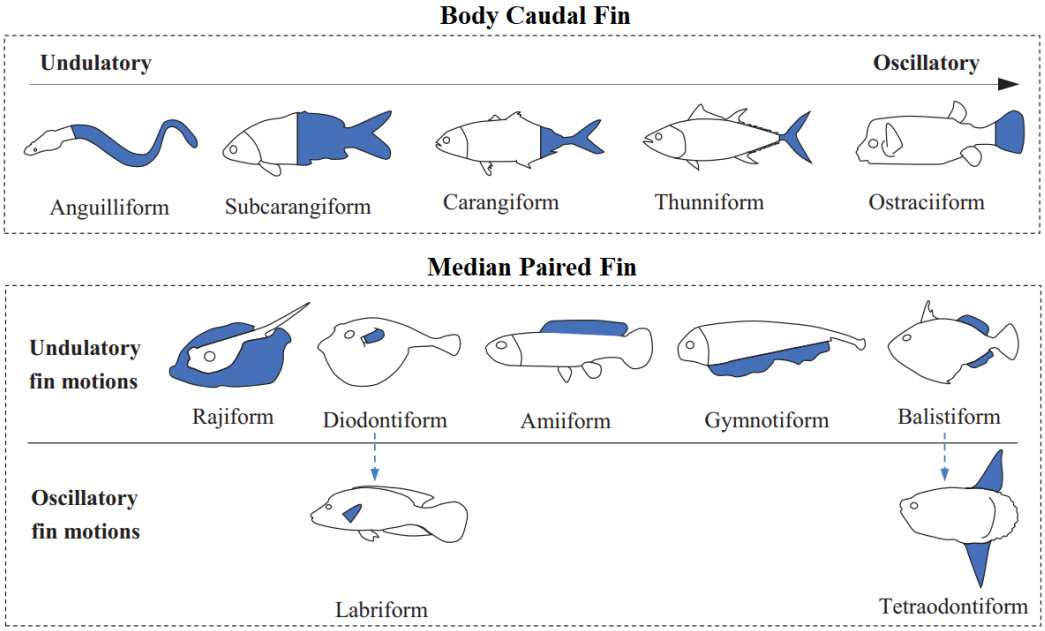

Figure 1.1 Overview of Body Caudal Fin and Median Paired Fin fish locomotion categories (Li et al., 2022).

As presented in Figure 1.1**Error! Reference source not found.**, BCF fish are further categorised into anguilliform, subcarangiform, carangiform, thunniform and ostraciiform, depending on the proportion of the central spine used in undulation or oscillation motion. These categories have been generally accepted (Sfakiotakis et al.,

1999;Blake, 2004); however, the latest research by Di Santo et al. (2021) suggests less significant differences between the categories and a higher convergence of body motion across different species. In particular, the assumption of reduced head amplitude of thunniform swimmers compared to anguilliform swimmers has not been confirmed.

Figure 1.2 (a) presents an example of a BCF swimmer, the Skipjack Tuna fish. The streamlined body uses the caudal fin as the main propulsor. Evolved to perform fast rectilinear swimming it can achieve swimming speeds of up to 2.1 body lengths per second at a maximum body length (fork length) of circa 108 cm and a maximum weight of circa 34.5 kg (Gooding et al., 1981). The median fins (pelvic, pectoral, anal and dorsal) contribute to both manoeuvring and stability, and were found to be actuated by a hydraulic mechanism that may provide advantages during predation through fast and precise actuation (Pavlov et al., 2017)

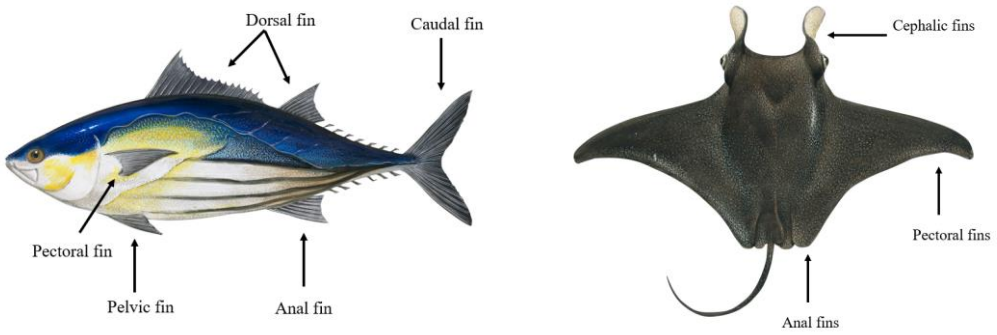

(a) (b)

Figure 1.2 Annotated image of (a) Body Caudal Fin category Skipjack Tuna (Britannica, 2023) and (b) Median Paired Fin category Mata Ray (Britannica, 2023).

To highlight the significant difference in physique, Figure 1.2 (b) presents an example of an MPF swimmer, the Manta Ray. Immediately obvious are the significantly larger median fins used as the main source of propulsion and manoeuvring. Synchronised spanwise wave motion and simultaneous flapping motion (Dewey and Smits, 2023) allow the Batoid category fish to swim large distances efficiently and at speeds of up to 24km/h (Chew et al., 2015). The propulsor allows the Manta Ray to perform looping and backward somersaults, which have been observed during feeding and mating (Fish et al., 2018). The largest recorded wingspan is 8.8 meters at a weight up to 2.4 tonnes. Both fish in Figure 1.2 are examples of specialised fish within the categories of BCF

and MPF, however, some fish are observed to switch between MPF and BCF locomotion behaviours (Gerstner, 1999). Species of fish that switch locomotion behaviours, known as decoupled locomotors, usually live in complex environments where agile acceleration change and obstacle avoidance are necessary. Elsewhere, coupled locomotors are observed to inhabit relatively simple environments (Blake and Chan, 2006). The clown fish represents an example of a decoupled locomotor that is known to live around coral reefs (Jones et al., 2005).

Figure 1.3 Clown fish, an example for a decoupled locomotor, swimming close to coral reef. (Britannica, 2024)

Shown in Figure 1.3, clown fish possess the ability to utilise their pectoral fin and central line body to generate thrust. MPF swimming is generally considered to be superior in manoeuvring tasks including the ability to swim backwards, supported by its ability to carefully vector thrust using its median fins. BCF swimmers typically have a streamlined body shape coupled with a powerful caudal fin propulsor to enable higher speeds. A study analysing the coupled locomotor species, Schlegel's parrotfish and Picasso trigger fish, found that these fish switch to BCF swimming for higher speeds and burst (Korsmeyer et al., 2002).

Fish apply various active and passive means to reduce drag, the force opposing the swimming direction, to increase swimming efficiency. For example, the discontinuous surface of scales creates small turbulences close to the fish surface leading to a delay of flow separation and thinning of the wake structure, fork shaped caudal fins create higher thrust without increasing drag, muscle adjusted stiffness of fins enables higher

tailbeat frequencies and elasticity provides springiness for potential energy to be periodically recaptured (Liao, 2022).

Figure 1.4 shows a schematic of the unsteady fluid acceleration of BCF swimming. Passing fluid is accelerated due to the pressure difference around the undulating swimmer. At the trailing edge the vortices are shed periodically in alternating directions, represented in the figure by different coloured arrows, leading to a cycle-averaged mean forward jet (Koochesfahani, 1989) that leaves a resulting reversed Karman vortex street in the wake. The vortex shedding frequency characterised by the nondimensional Strouhal number St has been found to be typically in the range of $0.2 < St < 0.4$ (Yen and Azwadi, 2015).

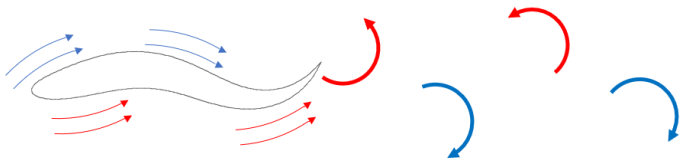

Figure 1.4 Schematic of unsteady acceleration of fluid during BCF thrust generation. Arrows indicate fluid acceleration and periodically shed vortices of alternating swirl direction.

Calculating the efficiency of self-propelled undulating swimmers remains challenging, as discussed later in this section. For general estimation, experiments of heaving foils have shown propulsion efficiencies of up to 87% at Strouhal Number St =30 (Read et al., 2003). In contrast, the thrust efficiency of small propellers remains below 40%, partly because of the energy lost in accelerating the fluid rotationally (Triantafyllou and Triantafyllou, 1995). Fish may also swim together with other fish, known as fish schools. Swimming within a collective enables fish to form a higher order swarm intelligence. Next to benefits such as predatory defence, fish may also achieve hydrodynamic benefit from swimming within the wake of other fish. A fish may achieve hydrodynamic benefit by varying its relative distance and position, amplitude envelope, undulation frequency and phase to adjust to the incoming vortex stream. Numerous research efforts continue to investigate related fluid phenomena, such as the numerical studies by Martens et al. (2017) and Gao and Triantafyllou (2018) and the experimental study by Li et al. (2021).

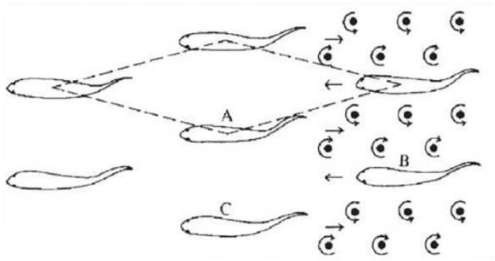

Figure 1.5 Schematic of multiple fish swimming within a school. (Weihs, 1973)

1.2 Experimental and computational investigations of fish swimming

To improve understanding of fish swimming and related fluid mechanisms, early experimental investigations were conducted including a study by Gray (1933). Figure 1.6 shows the experimental setup and the recorded image by Liao (2003) of a fish swimming within alternating flow conditions exhibiting the Karman gait, a distinct and low power swimming pattern to hold station.

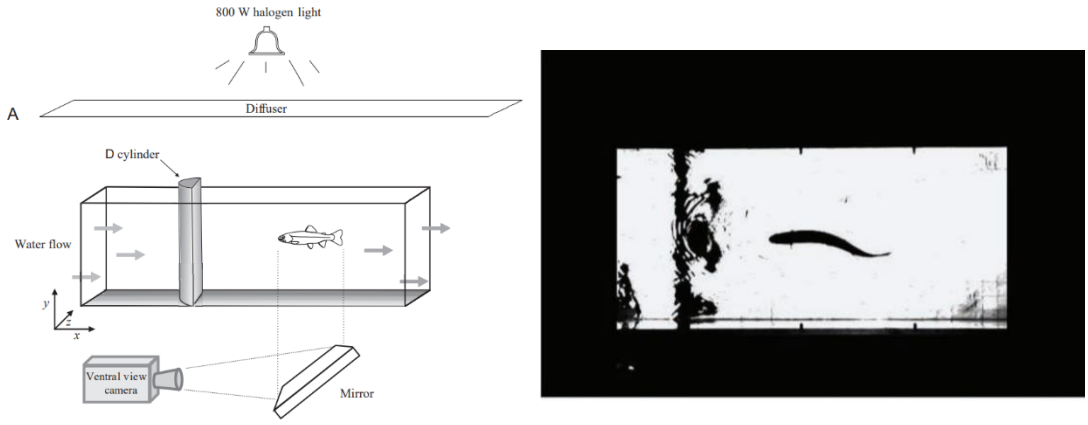

(a) (b)

Figure 1.6 (a) Experimental setup to study fish motion in alternating flow (Liao et al., 2003) (b) recorded image of fish performing Karman gait (Shell, 2012).

Modern experimental techniques, such as Particle Image Visualisation, allow the visualisation and measurement of flow structures, however, experiments remain challenging due to the need to control live fish in addition to sensing, repeatability and uncertainty requirements. Established by Lighthill, the Slender Body Theory (1960) (1971) enabled the first mathematical analysis of the hydrodynamic performance of an undulating body. In the same time span, work by Wu (1971a) (1971b) (1971c)

analysed the hydrodynamic performance of wavy plates with focus on kinematics and geometry.

Bio-inspired robotic systems may also be used as a validation or experimental platform (Ijspeert, 2014;Rezapour et al., 2014;Kelasidi et al., 2015;Tian et al., 2020). For example, using bio-inspired robots in lab experiments also makes it possible to measure the motor power and other parameters to assess the thrust efficiency.

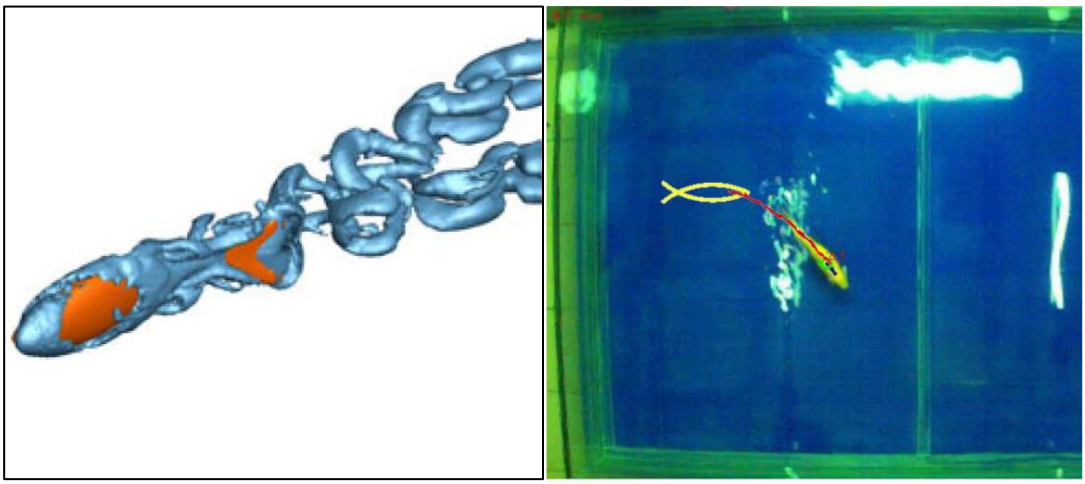

(a) (b)

Figure 1.7 (a) Snapshot of 3D flow structure from CFD simulation of undulating fish (Maertens et al., 2017) (b) Robotic fish experiments conducted by Tian et al (2020).

With the development of Computational Fluid Dynamics (CFD) and the availability of computational power, numerical analysis opened up new possibilities to study undulating bodies. It is now an established tool, next to experimental and theoretical analyses, to study fluid dynamic problems. Detailed and time discrete simulations make it possible to simulate over a large parameter space at different scales, under defined conditions and at reduced cost compared to experimental studies. The application of numerical analysis to the study of fish allows the temporal and spatial analysis of flow structures and flow properties. CFD has prompted a wide range of research work focusing on analysing and optimising fish-like body shapes and swimming motion (Kern and Koumoutsakos, 2006) (Tokić and Yue, 2012), (Maertens et al., 2017).

1.3 Bio-inspired underwater robotics

Bio-inspired underwater vehicles feature biologically inspired mechanisms, materials and other means to replicate the excellent swimming abilities of underwater creatures. Importantly, bio-inspired designs selectively incorporate elements inspired by nature and are therefore distinctly different to biomimetic devices that aim to fully replicate nature. A wide range of ingenious bio-inspired designs are presented in literature to improve upon conventional thruster propelled underwater robots, which generally have a rigid torpedo shaped or open frame structure.

In the following, only a brief introduction is offered to what is a wide and active field of research. Recent and comprehensive reviews are available, for example by Low (2011), Scaradozzi et al. (2017), Salazar et al. (2018), Wang et al. (2020) and Li et al. (2022). The terminology varies within literature when denoting a design as a vehicle, drone or robot and may be used interchangeably in the following. A key area of inspiration is the integration of natural swimming mechanics such as MPF and BCF mechanisms to replace conventional propeller-based systems.

MIT's Robotuna (Tolkoff, 1999) shown in Figure 1.8 is one of the first bio-inspired underwater robots. The tethered system enabled early experimental investigations of robotic fish swimming mechanics, fluid structure interaction and energetics. The robotic structure, covered with Lycra, consists of an aluminium frame actuated via pulleys and wires that convey motor power to rotational links.

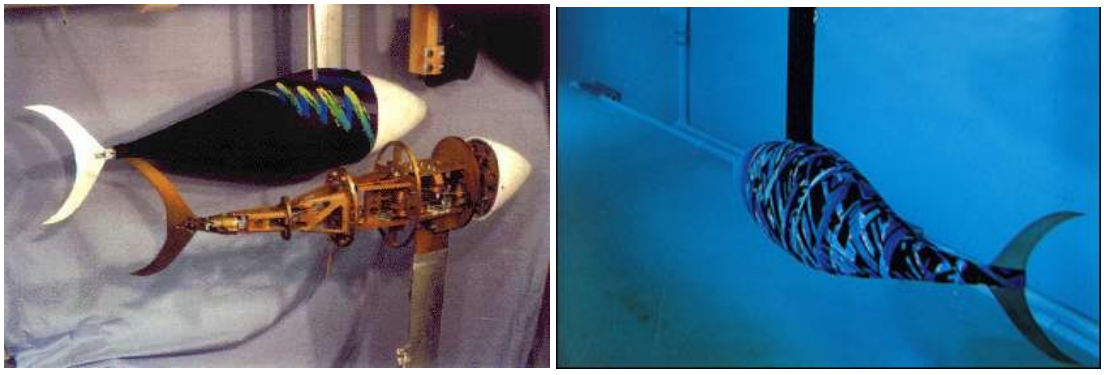

(a) (b)

Figure 1.8 Photo of Robotuna (©MIT Robotuna Project, 1994) (a) with and without a flexible cover and (b) inside a towing tank. (Triantafyllou and Triantafyllou, 1995).

In the following years, a large number of designs were developed inspired by different species to showcase innovative mechanisms, materials and more. Next to the Robotuna, notable examples include a design led by Huosheng Hu et al. (2006) and the soft robotic fish SoFi published by Katzschmann et al. (2018), both shown in Figure 1.9. Strikingly, both designs show a fish like appearance, mimicking not only central line displacement but also showing a streamline shape and passive elastic fins.

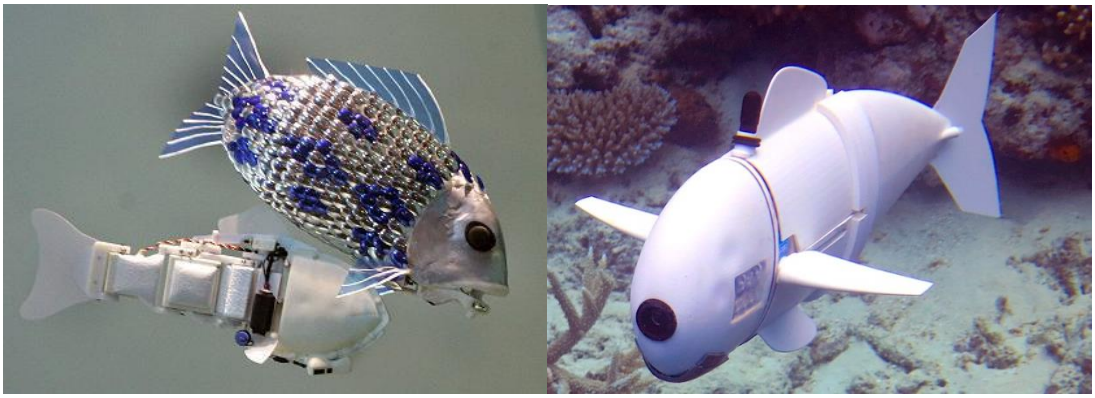

(a) (b)

Figure 1.9 Robotic fish designs created by (a) Huosheng Hu et al. (2006) (b) and Katzschmann et al. (Ackerman, 2018)

Notable designs within the category of MPF include the MantaDroid (Arastehfar et al., 2019), which achieves effective propulsion utilising passive deformation of a pectoral fin sheet, the BOSS manta ray (Glushko et al., 2018) with a highly detailed pectoral fin actuation mechanism, and the commercially developed Velox (Piliantenergy, 2023), which can be considered an amphibious design as it is able to utilise fin undulation to move on land and in water. All MPF examples share the common design feature of a rigid central compartment storing electronics and actuation elements to enable motion of the pectoral fins. BCF designs show a more diverse design approach including bulk bodies containing all necessary equipment with dedicated flexible appendages or a modular design of distributed electronic and mechanical equipment along the length of the body.

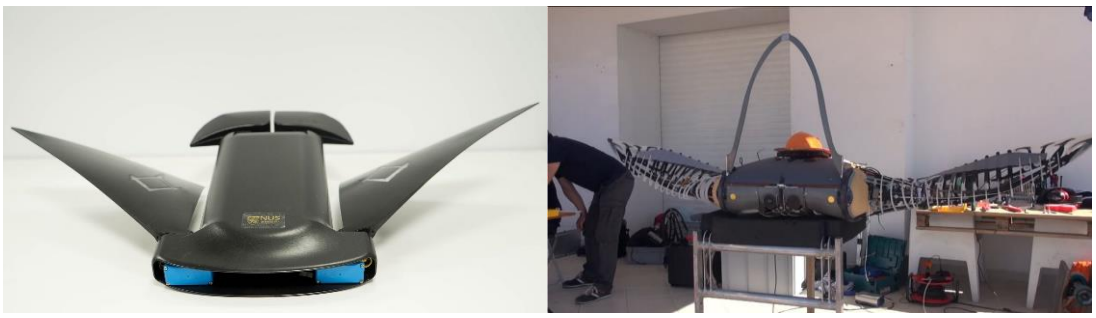

(a) (b)

Figure 1.10 (a) MantaDroid (Natashah Hitti, 2023) (b) (Evologics GmbH, 2023).

A modular design provides the ability to flexibly configure and re-configure the number and type of modules and, therefore, adapt and shorten or lengthen the robot structure in response to different task requirements. It also increases reliability through redundancy of function across similar modules and shows high potential for cost reduction through repeatedly applying a common modular structure with common interfaces.

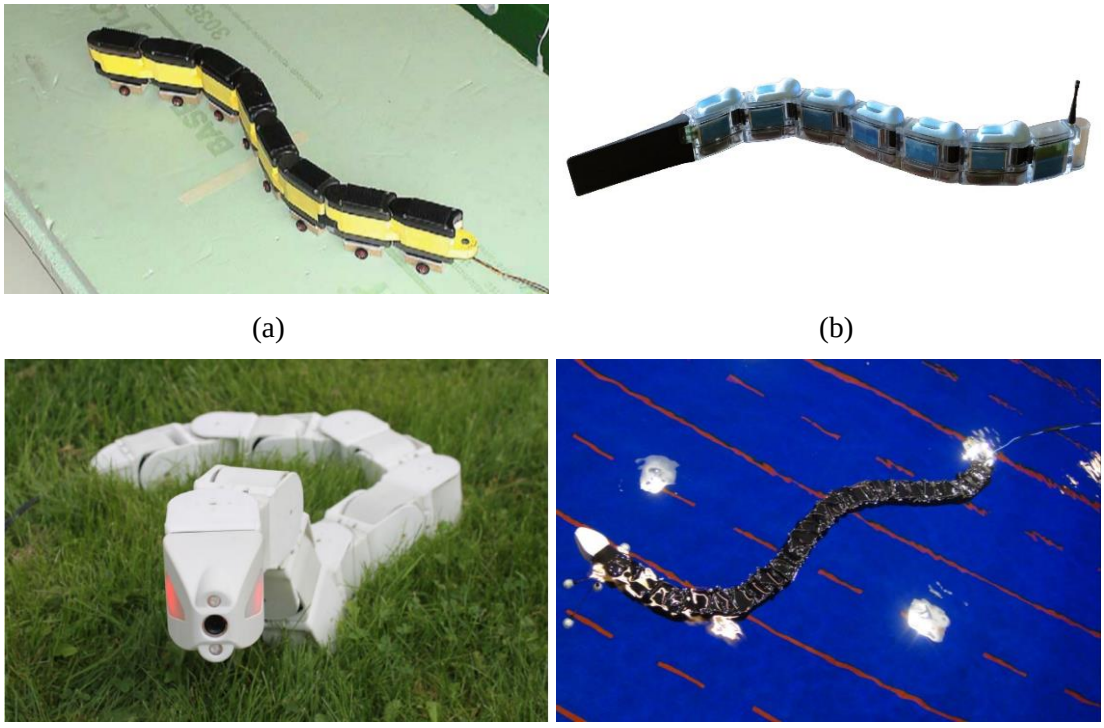

(a) (b)

(c) (d)

Figure 1.11 (a) Amphibot I (Crespi et al., 2005) (b) Envirobot (Bayat et al., 2016) (c) Mamba (Liljebäck et al., 2014) (d) Mamba with a waterproof flexible cover. (Qualisys)

The capabilities of such robot designs can also be efficiently extended and enhanced through the addition of new modular segments using these common interfaces without

having to replace the entire robot. Several modular robots have their origins in snake and amphibious designs, such as the snake robot Amphibot I (Crespi et al., 2005) that was later developed into the underwater robot Envirobot. Another example is the snake robot Mamba (Liljebäck et al., 2014), which is fitted with a watertight cover to swim underwater (Kelasidi et al., 2018), all shown in Figure 1.11.

Control of a multi-linked robot to mimic efficient biological inspired locomotion requires synchronised low-level control. The topic extends beyond fish undulating as other vertebrae also apply rhythmic locomotion coordinated via the central spinal cord. Various approaches have been developed to replicate vertebrae locomotion, including the Finite-State Machines (Lee and Yannakakis, 1996), the Sine-Generators (Gómez, 2008) and the Central Pattern Generators (CPG) (Ijspeert, 2008). All have the purpose of centrally manipulating multiple actuators to create rhythmic motion without the need for sensory feedback (Ijspeert, 2014). As an example, in a fish the central control coordinates the motion of individual muscles to shape a travelling wave. The control signals of each muscle, in robotics typically operated through a motor, are the pitching amplitude, frequency and phase. By varying these activities, it is possible to represent the different swimming gaits of the fish categories depicted in Figure 1.1.

1.4 Industry application of bio-inspired underwater robotics

Offshore operations such as the extraction of hydrocarbons, renewable energy harvesting and related decommissioning of underwater plant infrastructure as well as ocean exploration, science and defence research drive interest in reliable, clean, low cost and safe robotic systems. Future systems will be required to autonomously conduct inspection, maintenance and repair tasks to avoid the need to deploy large ships and their crew and to overcome labour shortages. Envisaged capable robotic systems promise to reduce costs through reliable and repeatable task execution while being deployed continuously with the ability to recharge and exchange information at a local dock. As a result, human presence can be reduced, mitigating the dangers to human life of operating in harsh sea environments. Underwater resident systems reduce human intervention, which greatly reduces costs and risks to human safety. It further supports continuous monitoring of offshore assets supporting reliable and

continuous operation through early fault detection and shorter repair times. Robots may operate in sea conditions considered unsafe for human intervention (Song et al., 2020).

To enable future autonomous AUVs, current research focusses on the development of underwater sensing and control as well as trustworthiness and ethical behaviour of autonomous systems. Current systems are either technically unsuitable or struggle to operate in high sea conditions due to the need to deploy human operators to ensure system recovery. In addition, there are challenges with regard to underwater sensing, communications and control as well as increased structural integrity, thrust and manoeuvring challenges.

Numerous industry and academic led efforts have been conducted to achieve reliable underwater docking solutions. A dock is a physical station to which a free-swimming robotic system connects. Most systems include physical guidance, such as a cone, to support final positioning of the robot. Data and energy may be transferred via inductive interfaces. Such pin-less interfaces greatly reduce the required position and orientation accuracy compared to pin connectors. The dock may be approached horizontally or vertically. General challenges to docking include robust autonomous control, accurate sensing and localisation as well as safe and efficient manoeuvring in unsteady fluid flow conditions. Current designs lack either manoeuvrability (torpedo shaped AUVs) or efficiency (open frame ROVs and AUVs). By taking inspiration from fish body flexibility, bio-inspired robotic systems will be able to access shape restricted spaces and show improved ability to adapt to complex environments.

For successful application and acceptance by industry, designs are required to be sufficiently robust and need to avoid complexity and fragility. Further crucial factors for successful industry acceptance are availability, repair and replacement time. Bio-inspired features may be applied selectively to robot designs with industrial applications in mind. Hybrid systems may offer enhanced performance in underwater industrial operations. Precisely this is demonstrated by the commercially available Eelume robot (Liljebäck and Mills, 2017) that combines body flexibility with the certainty of thruster systems.

(a) (b)

Figure 1.12 (a) Open frame ROV/AUV by Oceaneering, (b) bio-inspired multi-actuated hybrid ROV/AUV Eelume (Eelume AS, 2023).

1.5 Study objectives

Over the past decades engineers and scientists have studied the excellent swimming abilities of aquatic animals to understand their underlying mechanisms and apply this knowledge to the design of bio-inspired underwater vehicles. Robot designs inspired by nature promise to exceed conventional thruster propelled vehicles in efficiency, manoeuvrability as well as adaptability and resilience. The desire to build more advanced underwater robots is accelerated by the need for resilient, adaptable and efficient underwater robotic solutions to fully establish autonomous systems. Although various ingenious designs have been created, currently no bio-inspired underwater robot comprehensively achieves the swimming abilities of their natural inspiration. Shortcomings may originate from a lack of understanding and challenges in the implementation during the design, construction and operation.

Besides common challenges all underwater robots face, such as underwater sensing and intelligent autonomous decision making, improving the propulsion and manoeuvring ability of bio-inspired underwater robots is a key enabler to achieve autonomous operation with minimal or no human intervention. As highlighted during the introduction, bio-inspired designs mimic fish and other natural swimmers to achieve superior manoeuvrability, efficiency and the ability to operate and adapt to complex environments. Therefore, this work sets out to enable a better understanding of bio-inspired robotic hydrodynamics and control for improved implementation and operation.

This work aims to contribute to increasing knowledge of the fundamental mechanisms of fish swimming as well as practical knowledge with regard to the design, construction and control of bio-inspired underwater robots.

The presented research work is guided by the following research questions:

- How do fish swim efficiently and what are the characteristics and operation parameters of an efficient bio-inspired underwater vehicle?

To answer this questions the following specific research questions are approached in this thesis

- What is the optimal body curvature of a manoeuvring Body Caudal Fin swimmer to achieve low power, low radius turns?
- How does the caudal fin material affect propulsion efficiency?
- Can a swimmer draw energetic benefit from swimming near a bulk body during dynamic position holding?

Further, this work presents the design, construction and lab testing of a novel, modular bio-inspired autonomous underwater prototype.

In the following, a literature review will assess current state-of-the-art in modelling bio-inspired underwater vehicles, performing fluid and control-coupled simulations, fish manoeuvrability, fish energetics, as well as bio-inspired designs and specifically modular bio-inspired designs.

1.6 Outline of thesis

This thesis is organised in 7 Chapters plus a reference list and an appendix.

Chapter 1 provides a general introduction to relevant topic areas of this thesis, including fish swimming, experimental and computational investigations of fish swimming, bio-inspired robotics and industry applications of bio-inspired underwater robots.

Chapter 2 presents a critical literature review on modelling of bio-inspired robotics, control-coupled fluid simulations, fish manoeuvrability, a bio-inspired underwater robot design, modular bio-inspired robotics research and energetics as well as measurements of fish locomotion. In the following, concluding remarks are made and this outline of the thesis is given.

Chapter 3 introduces the numerical models and control algorithms applied in this study. After a brief introduction to relevant CFD theory, a single-body and a multi-body algorithm are described and a reference is given to a CFD-FSI model. Three linear feedback control strategies are developed for the analysis of unsteady fish manoeuvring.

Chapter 4 applies the developed control strategies in three feedback control-coupled numerical investigations. The studies focus on the optimal curvature envelope for BCF manoeuvring, an investigation into the thrust generation of a flexible plate of different material stiffness and frequencies as well as the hydrodynamic performance of a flexible plate within incoming flow and in front of a cylinder.

The second part of this thesis focusses on the design, construction and lab testing of a novel and modular bio-inspired underwater swimmer.

Chapter 5 describes the design and construction of a new modular bio-inspired robot prototype. The design includes the novel application of a synchronous magnetic coupling. This chapter includes a description of the complete design process including mechanical and electrical design, prototyping as well as analytical and numerical results of the magnet coupling strength.

Chapter 6 presents hydrodynamic lab test results of the created robot prototype that were conducted at the Hydrodynamics Laboratory at Strathclyde University. Tests are presented for thrust measurement, using a custom-made testing stand, and free-swimming tests, measuring the trajectory of the robot through motion capturing.

Chapter 7 concludes the thesis by summarising the presented work, the achieved novelty and contributions to knowledge and provides an outlook into continuing research questions.

Finally, after a reference list, the appendix includes the User Defined Function of the presented single-body model of Chapter 3 to highlight the implementation and function of the applied Ansys Fluent UDF coupling methodology.

Chapter 2 Literature review

2.1 Manoeuvrability of BCF fish locomotion

Most previous studies have focused on steady fish locomotion, but fish spend the majority of their time performing unsteady locomotion (Drucker and Lauder, 2001).

An early study of unsteady locomotion is the experimental investigation by Gray (1933), who recorded fish utilising body curvature to generate a turning momentum.

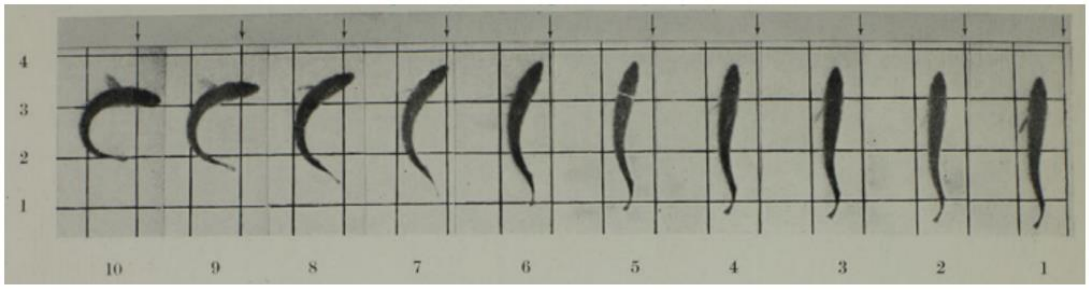

Figure 2.1 Turning Whiting fish recorded by Gray (1933).

Gerstner (1999) measured the trajectory of fish during feeding and agnostic interaction of coral fish who are known to be decoupled locomotors and utilise both MPF and BCF techniques. Analytical studies have been conducted by Weihs (1972) on the hydrodynamics of fish turning manoeuvres and Tan et al. (2010) on robotic fish turning. More recently, new numerical techniques enabled free-swimming CFD simulation of fish manoeuvring, such as the work by Hess et al. (2020) on manoeuvring of an elastic plate and Tian (2020) on robotic fish turning and CFD simulation comparisons.

The term *manoeuvrability* is used to describe a range of unsteady locomotion, such as C and S starts and turning manoeuvres (Drucker and Lauder, 2001). For example, the agile manoeuvrability of a fish is displayed during C-starts when the fish accelerates from a stationary state by means of a single large sweep of its tail fin to create two

distinct vortices that define the momentum and impulse at which the fish turns and accelerates (Epps and Techet, 2007).

Streamlined BCF fish moving at an initial velocity can perform unpowered turns, in other words, turning without increasing its momentum due to their high fitness, characterised by the body length to thickness ratio, while unstreamlined MPF fish have to continuously generate thrust during turning manoeuvres due to their low fitness (Blake, 1977). Unpowered turns may lead to smaller turning radii (Fish, 2002); large animals with large inertia may prefer unpowered turns (Blake and Chan, 2006). A simple relationship between turning radius R and body mass m, $R \propto m^{0.37}$, as well as a linear relationship $R \propto L$ between R and the body length L, has been reported (Blake and Chan, 2006).

Fish gain their high manoeuvrability from their inherently unstable motion. The quasi-steady state of straight swimming of a BCF swimmer relies on force symmetry over a full actuation cycle. Small perturbations of fluid flow or body motion lead to loss of force equilibrium and a change in heading direction (Webb and Weihs, 2015). During turning manoeuvres fish may also use fins as control surfaces to generate turning moment (Drucker and Lauder, 2001) or to balance forces (Weihs, 1972).

Robotic fish may perform turns with variable curvatures across multiple links (Yu et al., 2008). Compared with conventional rigid torpedo or open frame shape Remote Operated Vehicles (ROVs) and AUVs, bio-inspired underwater robots and vehicle platforms may feature significantly enhanced efficiency and manoeuvring capacity. Indeed, tests of a free-swimming tuna robot demonstrated turning rates of up to 75 degrees per second (Anderson and Chhabra, 2002), exceeding the turning rate of 25-35 degrees per second of a modern enhanced rigid hull AUVs (Randeni et al., 2022).

2.2 Energetics of fish locomotion

Measuring and quantifying the energetics of fish locomotion is a key enabler to understand bio-inspired locomotion and replicate this natural ability in human made machines. Determining the efficiency of a fish remains challenging and highly

complex, especially under unsteady conditions. The following literature review aims to highlight current standard practices and remaining challenges.

The Froude efficiency describes the useful output power in relation to the input energy and is often used to assess engineering systems. With respect to the simplified BCF fish swimming scenario, it describes the relationship between the energy required to realise body undulation and swimming work. Here, the swimming work is defined as the product of longitudinal force acting on the body and the swimming velocity. For a fish following a straight trajectory at a constant speed, in other words, moving at a quasi-steady state, the cycle-averaged longitudinal force is zero due to the balance between thrust and drag. The resulting Froude efficiency is zero and, therefore, not applicable. First mentioned as Self-Propelled Fitness (Barrett, 1996) and later proposed as an efficiency measure (Maertens et al., 2015), the quasi-propulsive efficiency is defined as $\eta_{QP} = RU_s/\overline{P_{in}}$, where the output power of a swimming fish is approximated by the product of the swimming speed U_s and the resistance force R acting on a rigid body towed at the same speed. $\overline{P_{in}}$ is the cycle-averaged input power to realise the undulation motion. Alternatively, the Cost of Travel (CoT), the ratio of the energy spent per unit distance travelled is often used in life science as a quantitative measure of energetics in locomotion.

The performance of turning fish is evaluated based on the minimum turning radius derived from the trajectory of the centre of mass (Drucker and Lauder, 2001). Importantly, for identical centre of mass trajectories the required turning space may differ depending on the body flexibility of the swimmer (Walker, 2000).

The Linear Manoeuvrability Number (LMN), first mentioned to assess the manoeuvrability of a land-based hexapod (Jindrich and Full, 1999), has also been used to quantify fish manoeuvrability (Drucker and Lauder, 2001). The LMN is defined as the ratio of the time integral of the force impulse perpendicular to the forward momentum.

Ideally, a quantitative measure of manoeuvrability must provide a combined assessment of power expenditure as well as linear and angular displacement. In that sense, neither the CoT nor LMN are a suitable measure of fish manoeuvrability.

Recent investigations on the energetics of fish locomotion utilise bio-inspired robotics to benefit from the controllability and measurability of the engineered system. In Lu et al. (2023), the authors propose a cost-and-energy-saving analysis and a power cost optimisation method. The analytical and experimental work compares the swimming efficiency of a robotic fish with a caudal fin made up of two active and two passive joints and another robotic fish consisting of 4 actuated joints. Inspired by the flexible material structure of fish, the design of the passive joints is proposed to reduce the moment of inertia of the caudal fin and the required active torque of the joints. Results show a reduction of Cost of Travel up to 75% through the use of passive joints.

Anastasiadis et al. (2023) present an analysis of the swimming efficiency of a multi-actuated eel-like robotic fish and identify trade-offs between swimming efficiency and swimming speed. The parametric study of different undulation amplitudes, wave lengths and frequencies show that the swimming speed of the robotic fish increases for higher amplitudes and wave lengths, however, higher efficiency is achieved at medium amplitudes and wave lengths. Changes to the frequency modulate the swimming speed while maintaining efficient locomotion.

2.3 Modelling and simulation of fish locomotion

In the past, simulating bio-inspired propulsion around wings and fins was often modelled as a single body system (Combes and Daniel, 2003;Akhtar and Mittal, 2005;Spagnolie et al., 2010;Mountcastle and Combes, 2013). However, such approaches may only model part of the fish body, for example, the caudal fin, and neglect complex internal dynamics of the fish physique. A fish may be modelled as a multi-body system in which active muscle actuation and passive deformation of appendages are represented by active and passive rotational joints respectively. The resolved internal dynamics provide insights into the muscle behaviour and torque, which also benefits the development of bio-inspired robotic systems. Various multi-body simulations with active prescribed joint motion and passive spring like deformation may be found in literature (Farnell et al., 2004;Akhtar and Mittal, 2005;Kajtar and Monaghan, 2010).

Recent multi-body models have mainly been developed for control purposes and include simplified fluid models that enable fast computation. Boyer et al., (2006) and Khalil et al. (2007), presented models for a 3D eel-like robot based on the Newton-Euler equations and a semi-empirical fluid equation. As noted by Kelasidi (2014), both models require numerical computation of the drag forces.

Kelasidi et al. (2014) presented a multi-body dynamics and hydrodynamics model based on the semi-empirical Morrison's equation in closed form that mitigates the need to numerically compute the drag forces.

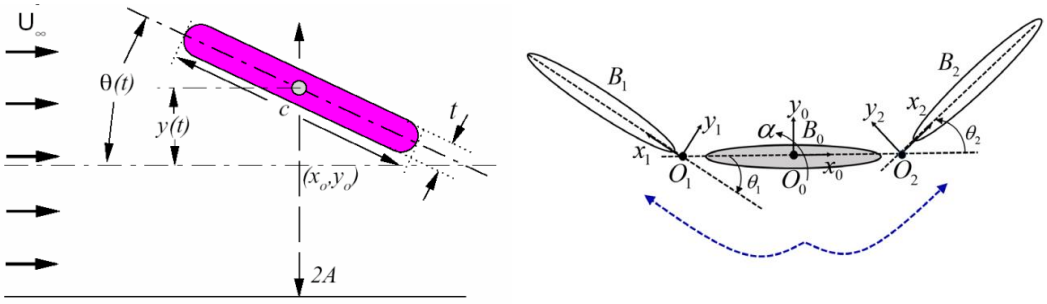

(a) (b)

Figure 2.2 Exemplary schematics of simulated simplified rigid single body fish (Akhtar and Mittal, 2005) and (b) multi-body systems (Li et al., 2018).

As noted by Porez et al. (Porez et al., 2014), to create an accurate model that describes the relationship between local and global motion and external forces requires the solution of the Navier-Stokes equations which cannot currently be resolved in real time. Simplifications, such as the assumption of inviscid flow may be compensated with models of specific flow features, yet many remain too computationally expensive for real time calculations. Popular analytical fluid models in the robotics community include Morrison's equation (1950) and Large Amplitude Elongated Body Theory (LAEBT) by Lighthill (1971) as well as their evolutions and extensions. Simplifications and inaccuracies of analytical fluid dynamic models lead to inaccuracy and increasing error over time. In terms of analysis, derived results may no longer represent the real world.

Implementing body dynamics algorithms within numerical simulations makes it possible to resolve the Navier-Stokes equations and gain detailed insights into the fluid

flow and fluid structure interaction. Although slower in comparison with traditional models for controller development and analysis, this approach provides important insights into the fluid structure interaction and may also support faster computing simulations in that it is able to calculate the fluid coefficients required in simplified models. CFD simulations coupled with dynamics models allow the simulation of self-propulsion, which is important in capturing instantaneous forces and moments. For self-propelled swimmers, the incoming velocity may no longer be a predefined constant but instead a result of the fluid structure interaction. Li et al., (2018) presented a multi-body CFD tool that is able to simulate serial and tree-like multi-body structures. Their multi-body algorithm coupled with a Navier-Stokes solver is able to resolve the internal and external dynamics of the multi-body system via three recursive calculations.

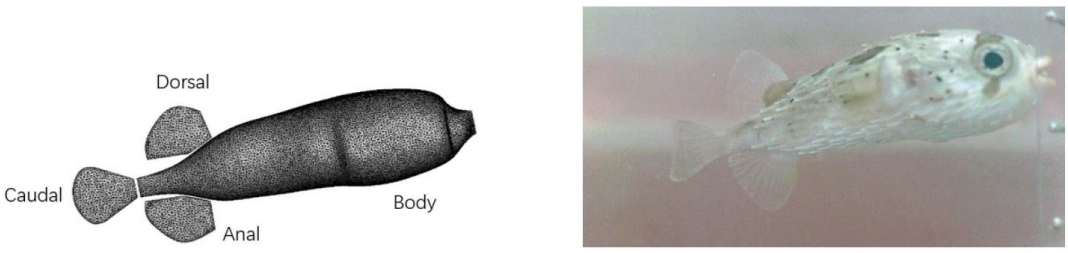

(a) (b)

Figure 2.3 Presented by Li et al. (2018), a simulation of a Puffer fish: (a) surface meshed CFD model and (b) live photo

To solve the Navier-Stokes equations in a discretised domain, the commonly applied numerical techniques are the finite difference, finite element and finite volume methods. The three techniques may show different applicability and individual benefits and drawbacks, depending on the simulated case. The finite difference method is the oldest method and was developed by Euler in 1768. It may only be applied to a structured mesh, where it describes the fluid domain at each grid point. The finite volume method, characterised by the integral formulation of the Navier-Stokes equations, directly utilises the conservation laws of mass, moment and energy. This technique may be applied to more complex and dynamic meshes. The majority of commercial fluid solvers are finite volume based.

Mesh generation is highly individual to the simulated problem and remains challenging for complex objects. A numerical method not requiring a body conforming mesh is the Immersed Boundary (IB) method, first developed by Peskin (1972). This method remains a highly attractive tool due to the relative ease of modelling moving boundaries and complex geometries as well as the relative speed of computation, and has been used in several studies of fish swimming (Zeng et al., 2023). Mittal and Iaccarino (2005) discuss the IB method, its implementation and the differences between conform and non-conform body mesh methods. The body conform methods such as the finite volume method, sees the geometrical grid information incorporated in the discretisation of the governing equations. In the IB method, the simulated flexible or rigid body is placed on top of a Cartesian grid, where both object boundaries are not conformed. This significantly simplifies grid generation and avoids coordinate transformation and complex discretisation operators yet requires modification of the governing equation close to the body boundary. Regardless of the required higher mesh scaling around boundary layers for non-conform grids and higher Reynolds numbers, the use of a Cartesian grid significantly reduces computational expense; however, the special treatment around the boundaries may deteriorate the stability, accuracy and conservation properties compared to body-conform mesh schemes (Mittal and Iaccarino, 2005). Huang and Tian (2019) describe different remaining major challenges of the IB method, including improving boundary layer modelling and improving related computational expense.

Advances in artificial intelligence (AI) and machine learning (ML) have also been applied to the field of fluid mechanics and fluid dynamics simulations of bio-inspired locomotion, including fish swimming. The term machine learning includes different approaches such as deep neural networks as well as reinforcement learning and deep reinforcement learning (Wang et al., 2022). Reinforcement learning describes a repetitive learning process guided by a reward function to iteratively achieve an optimal solution. Neural networks are mathematical structures of connected nodes, inspired by the human neuro system, that are able to learn based on labelled data, so-called supervised learning, to make predictions that are also true based on provided input data or known laws of physics. Next to the application of ML techniques to optimise locomotion parameters, ML techniques may also be applied to solve the

governing Partial Deferential Equations (PDEs) of fluid flow. Ranade et al. (2021) presented an ML based solver able to solve the steady incompressible Navier-Stokes equations including the widely accepted reference case of flow past a cylinder. Successful ML techniques may be able to provide real time solutions of fluid flow to enhance in situ control algorithms with flow information for the solution of the dynamic equations. Something that is not possible in real time with current available methodologies.

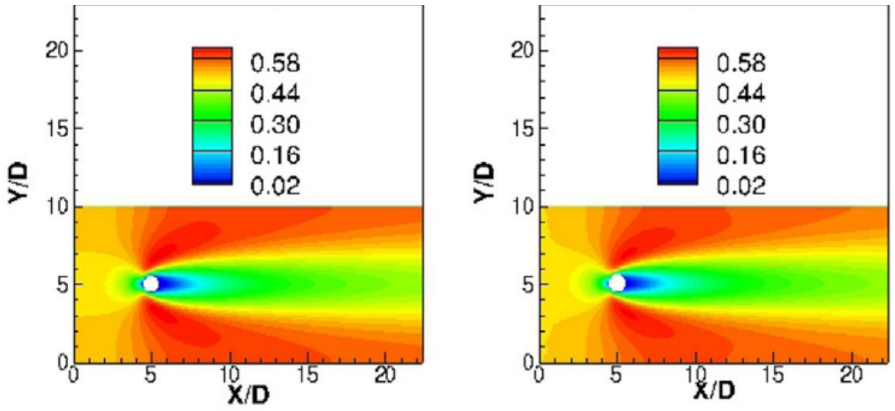

(a) (b)

Figure 2.4 Comparison of a velocity magnitude contour at Re = 10 between (a) ML-based fluid solver and (b) Ansys Fluent. (Ranade et al., 2021).

It may be said that the ML based fluid dynamics is still in its infancy. Despite promising early results, several challenges remain, especially at higher Reynolds numbers and turbulent flows (Duraisamy et al., 2019). A general challenge of ML models beyond the field of fluid mechanics is the acquisition, generation and quality control of input data. A solution to this may be provided by Physics Informed Neural Networks (PINN) that provide input information based on known laws of physics (Raissi et al., 2019).

2.4 Fluid and control design simulations

Significant progress in simulation tools and available computational power have enabled more and better analysis of fluid problems relating to fish hydrodynamics. In 1998, Carling et al. (1998) published work in which the swimmer moves freely and self-propelled by means of simultaneous solution of Navier-Stokes equations and Newton's Second Law. Compared to the previously made assumptions of a globally

fixed swimmer, the free moving solution makes it possible to capture instantaneous acceleration effects. Many studies focused on the analysis of steady fish locomotion in uniform water conditions (Kern and Koumoutsakos, 2006) (Tokić and Yue, 2012) (Eloy, 2013); however, fish spend the majority of their time performing unsteady locomotion (Drucker and Lauder, 2001) and experience unsteady flow (Liao et al., 2003). Feedback control plays a key role in unsteady swimming locomotion, such as manoeuvring, through proper sensing and actuation techniques.

Maertens et al. (2017) applied a PID controller in a CFD study investigating optimal amplitude functions of a 2D and 3D fish-like body and optimisation of two fish-like bodies swimming in tandem. Their study compares different combinations of amplitude envelope functions and function variables and uses the quasi-propulsive efficiency as criteria of energy efficiency. Investigated amplitude envelope functions are linear, quadratic and Gaussian exponential. Each combination of amplitude function and function variables generates a different level of thrust force. The fluid governing equations are solved using the second-order boundary data immersion method (BDIM) published by Maertens and Weymouth (2015). To compare the different amplitude combinations, a PID controller is setup to scale the amplitude magnitude so that the generated thrust force is matched with the incoming velocity drag force. The controlled system results in the fish-like body swimming at quasi-steady state at a Reynolds number 5000, where the input power is measured to calculate the quasi-propulsive efficiency. The initial transition to undulation motion results in a momentum and subsequent heading change away from the horizontal direction. To maintain a horizontal swimming position, a second PID controller is applied to scale the fish-like body curvature that controls the turning momentum to counteract any divergence from the horizontal heading. The controller gains were determined ad hoc. For 2D gait optimisation, a globally fixed NACA0012 hydrofoil is set to adjust its thrust and heading by varying its amplitude and curvature magnitude respectively. The study achieves carangiform gait optimisation for 2D swimmers from 35% to 50% and for 3D swimmers from 22% to 34% quasi-propulsive efficiency.

Gao and Triantafyllou (2018) applied two independent PID controllers to scale the amplitude magnitude and control the tail pitch bias on a fish-like body to study the

optimal hydrodynamic interaction between two fish-like bodies swimming in tandem. The applied fluid solver and PID controllers correspond to those of Maertens et al. (2017). In both studies the undulation cycle-averaged linear momentum in x and y are used as control errors for speed and steering respectively. The authors noted that for converging control parameters, the hydrodynamics parameters also converge over one undulation cycle, resulting in a consistent Karman vortex street over multiple undulation periods. Figure 2.5 shows the used NACA0012 geometry with an independent caudal fin, which provides an additional degree of freedom but remains kinematically and dynamically coupled to the main body.

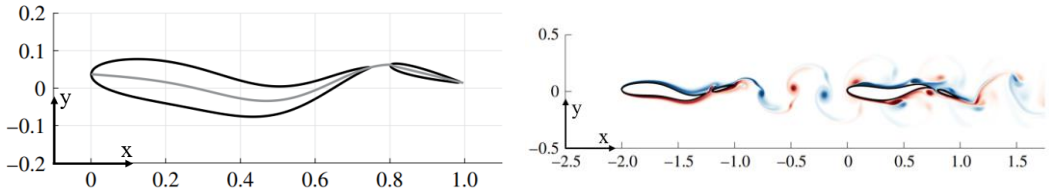

(a) (b)

Figure 2.5 (a) NACA0012 geometry with independent caudal fin (b) vorticity schematic highlighting the influence of the caudal fin on the vortex street in the wake and interaction between two fish like bodies swimming in tandem. (Gao and Triantafyllou, 2018).

Controlling the caudal fin independently improves fluid structure interaction at the upstream swimmer and downstream swimmer, interacting with incoming vortices.

The study of Gao and Triantafyllou (2018) finds that energy savings may surpass 50%, resulting in a quasi-propulsive efficiency rising from 60% to 90% only when the caudal fin is allowed to pitch independently. Results show a high sensitivity of caudal fin parameters on the efficiency, from which the importance of accurate flow sensing and feedback control is concluded.

Tian et al. (2020) applied feedback control known as Active Disturbance Rejection Control (ADRC) within a numerical fluid simulation to create a virtual platform to find optimal controller gains. As with PID control, ADRC is driven by tracking error and is a model free control strategy in that it does not require a detailed model of the systems dynamics but is simply applied on the input and output of a system. In contrast, Model predictive control (MPC) requires a detailed dynamics model to predict the state of the system at a future time. Both control strategies also share

simplicity in implementation and application to a wide range of problems. Han (2009) speculates that ADRC may reduce PID application dominance by addressing four limitations of PID control. The improvements inherent in ADRC include the following: the differential equation used as a transient profile to avoid a stepwise error function, a noise tracking differentiator to avoid instability related to the sensitivity of the derivative term, a nonlinear feedback control law to replace a simple three term sum and total disturbance estimation and rejection to mitigate instability of the integral term. Tian et al. (2020) applies ADRC control, shown in Figure 2.6, for the 2D orientation control (yaw) of a fish robot swimming between two arbitrary points at an assumed constant speed.

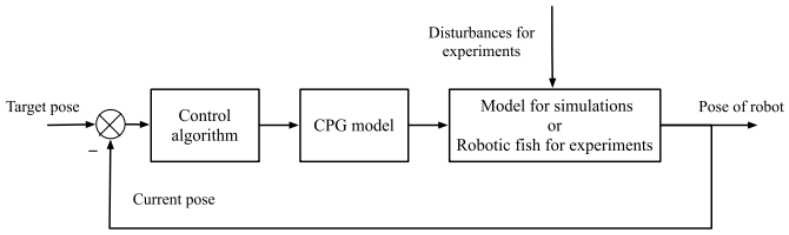

Figure 2.6 ADRC feedback control block diagram as implemented by Tian et al. (2020) and Li et al. (2019).

With reference to Li et al. (2019), the study considers the three control scenarios of 1) target position control, 2) target pose control, in other words, heading control without transfer orientation and 3) target pose with transfer orientation. Combined control of a target position and orientation is achieved by defining the initial control input as the sum of the weighted difference between a target angle and an auxiliary angle of a transition point and an observer variable respectively. The key novelty of the study is the integration of the control algorithm within a CFD environment that is used to simulate and identify optimal control gains of the ADRC controller. The 2D numerical results are successfully matched with a physical 3D prototype in terms of trajectory, swimming efficiency and power cost. The use of an ADRC controller is justified by potential disturbances, such as water ripples, yet the authors do not quantify such disturbances and fail to show the benefit of using ADRC over PID control. The described cases published by Maertens et al. (2017), Gao and Triantafyllou (2018) and Tian et al. (2020) all apply prescribed body kinematics; hardly any work has coupled

control FSI simulation that simultaneously solves the fluid and structure governing equations.

Hess et al. (2020) apply two PID controllers on a self-propelling soft robot-like swimmer to achieve the desired swimming speed and trajectory tracking. The soft robot is represented by a 2D elastic plate with finite thickness. The plate is actuated by means of active contractile strains on both sides. The PID controller independently scale the actuation strength and bias of the active material strains for thrust and orientation variation respectively. The simulation is set within a novel Fictious Domain FSI solver that efficiently deals with coupled computation of non-linear structures and flow dynamics (Lin et al., 2019). Figure 2.7 (a) shows an instantaneous vorticity contour of the swimming plate including reversed Karman vortex street. Figure 2.7 (b) shows the trajectory and radii of the turning plate as a result of different factors of strain bias denoted as β by the authors.

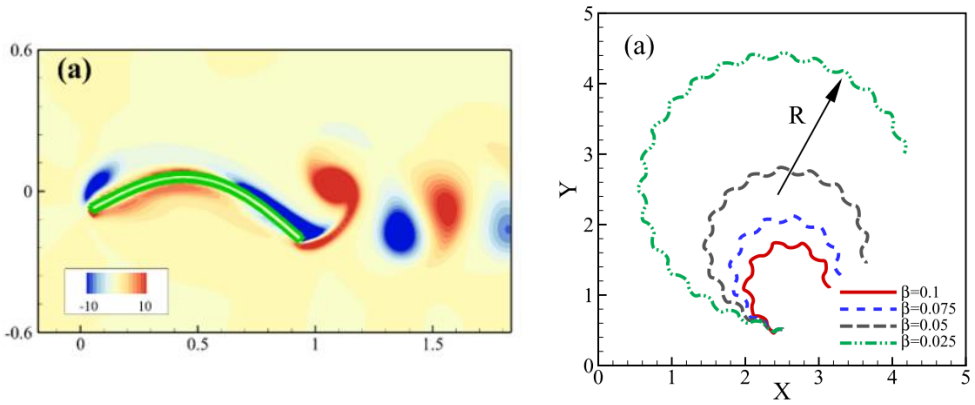

(a) (b)

Figure 2.7 (a) Instantaneous vorticity contour (b) turning trajectories and turning radii for changes of strain bias β (Hess et al., 2020).

Using the established CFD-FSI and control environment, Hess et al. (2020) employed a multi-object evolutionary method to find the optimal feedback controller for manoeuvring. In detail, control parameters were optimised for a number of moving target trajectories at different Reynolds numbers as well as straight and sinusoidal paths. Figure 2.8 shows two trajectories of the optimised path following control (red: lowest average error, blue: lowest combination of error and elastic energy). A multi-objective evolutionary algorithm is applied that uses an evolutionary process to find solutions that balance multiple, often conflicting objectives simultaneously.

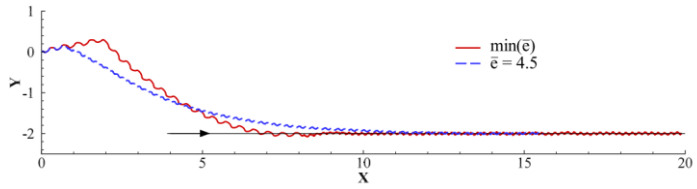

Figure 2.8 Straight line trajectory tracking optimisation results of minimum average error (red) and minimum average error and lowest elastic energy (blue) (Hess et al., 2020)..

2.5 Bio-inspired robot design review

A key feature of BCF bio-inspired propulsion is structural flexibility along the central line. Limited by the inability to manufacture natural muscles and soft tissue, scientists and engineers have developed ingenious approaches to recreate the oscillation and undulation motion of body caudal fin fish.

Elastic bending in smart materials is triggered by electrical and temperature stimulation. By applying and removing external signals according to a time profile, periodic motion is introduced (Ma et al., 2023). Examples of smart materials and their application in bio-inspired propulsion are Piezoelectric Ceramics (Cha et al., 2016), Shape Memory Alloy (SMA) (Coral et al., 2018), Ionic Polymer Metal Composites (IPMC) (Chen, 2017), Dielectric Elastomers (DE) (Shintake et al., 2018) and Super Coiled Polymers (SCP). An SMA based design created by Coral et al. (2018) and an SCP based design created by Rajendran (2022) are presented in Figure 2.9.

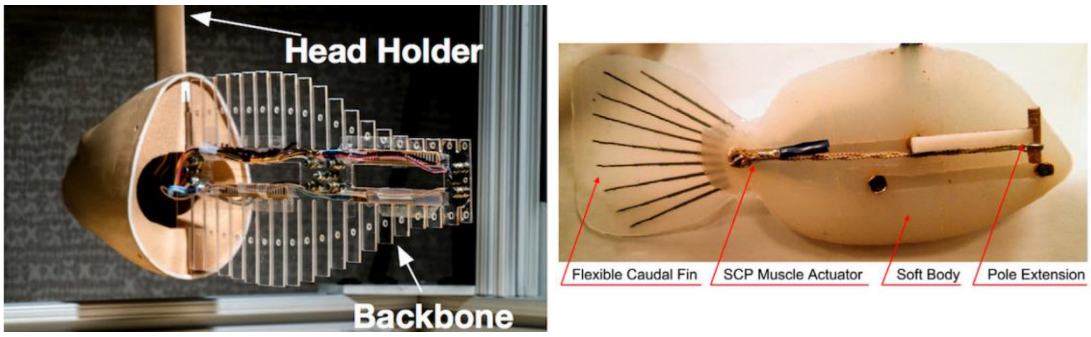

(a) (b)

Figure 2.9 Examples of robotic fish designs using smart materials based on (a) Shape Memory Alloy (SMA) (2018) and (b) Super Coiled Polymers (SCP) (2022).

Hydraulic and pneumatic actuators achieve periodic motion via pressure difference of internal cavities. Developed at MIT the Soft Fin Robot (SoFi) (Katzschmann et al., 2015) utilises a hydraulic pump to move water between two cavities. A Pneumatic

actuation mechanism applies an identical methodology but uses air as the pressure medium. Examples of pneumatic actuators used in robotic fish are presented by Wolf and Lauder (2022) and Yu-Hsiang (2023). Motors transform electrical energy into mechanical energy and play a crucial role in many applications. Direct current motors, servo motors and stepper motors are used in various bio-inspired robotic designs. Presented by Chen and Jiang (2019), a servo motor is used to drive a tensegrity structure. Rubi at al. (Parra Rubio et al., 2023) developed a modular and scalable robotic fish structure that is made up of a number of voxels actuated by a servo motor pulling tendons.

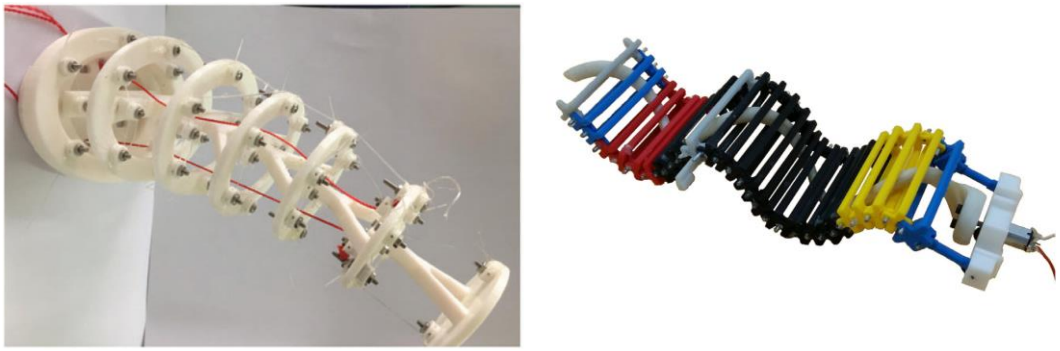

(a) (b)

Figure 2.10 Undulation actuated mechanical designs of (a) tensegrity structure by Chen and Jiang (2019) and (b) rotation helix by Struebig et al. (2020).

Struebig et al. (2020) presented a design in which a helix is continuously rotated by a DC motor. The horizontally rotating helix moves laterally connected discrete panels to create a periodic moving surface. In addition to single actuator designs, various designs apply multiple actuators in a serial arrangement to achieve elongated multi-actuated structures. The design investigated by Yu (2008) connects two servo motors in series, which enables the variation of gait kinematics via direct control of the individual servo input signal. Liljebäck et al. (2014) and Bayat et al. (2016) individually presented modular robotic designs in which modules housing electronic equipment are connected in series.

2.6 Modular bio-inspired robotics review

Modular snake or eel-like bio-inspired robotics is a branch within bio-inspired robotics with strong research interest. This may be due to the early interest in the distinct

locomotion of snakes (Liljebäck et al., 2013) and their ability to travel both on land and in water as amphibians (Ijspeert et al., 2007), but may also be the logical extension to early designs of in series connected actuators or a result of the appealing benefits of a modular configurable, extendable and redundant design.

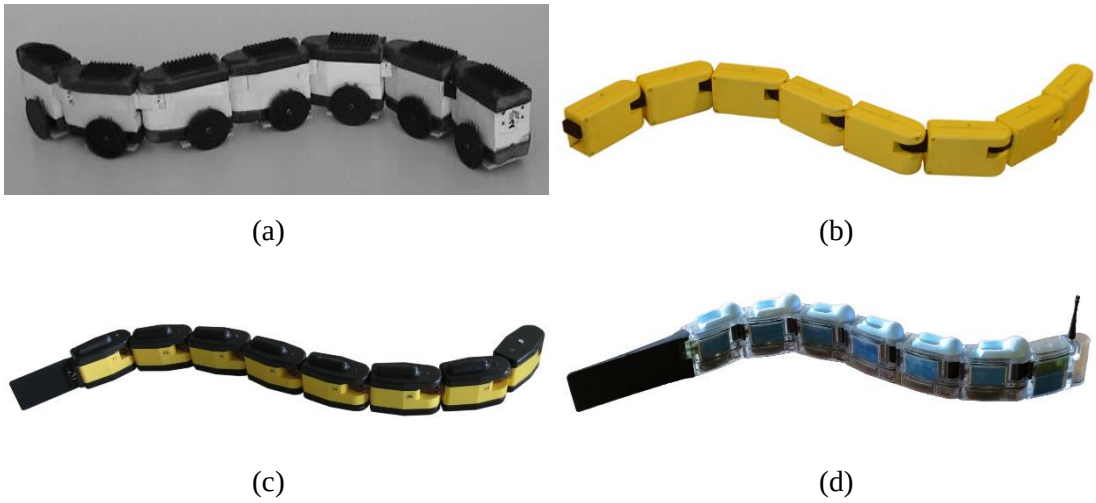

(a) (b)

(c) (d)

Figure 2.11 Modular snake / eel like robot design (a) Amphibot I (Crespi et al., 2005), (b) Amphibot II (Crespi and Ijspeert, 2006), Amphibot III (Porez et al., 2014), (d) Envirobot (Bayat et al., 2016).

The first iteration of the Amphibot was described in (Crespi et al., 2005). The modular robot that took inspiration from snakes and amphibians was designed to crawl on land and swim in water. The tethered design consists of 7 actuated elements constructed using a polyurethan cast mould and O-rings for watertightness, with each module measuring 7x3.3x5 cm (LxWxH). Each joint provided one rotational degree of freedom in yaw. Each module housed a 3.7 V battery with 600mAh to drive a 0.75W motor at 3.6V and electronics at 5V. The battery capacity allowed for 2hrs continuous use and an LTC 1733 control chip enabled recharging when activated. The DC motor of circa 60% efficiency is connected to a shaft via gears with a reduction factor of 400, which resulted in a maximum oscillation frequency of 0.3 Hz at 45 degrees amplitude. The robot is controlled via a CPG system and a PD controller is applied to achieve the required joint torques. The maximum measured crawling speed was 0.035 m/s at a wave frequency of 0.25 Hz, a phase lag of 0.5 and an amplitude of 45 degrees.

In 2006, Crespi and Ijspeert (2006) published the second generation design of the Amphibot. The design also has 7 elements but could theoretically incorporate up to 127 segments into the chainlike structure. Each module has a dimension of 9.4x5.5x3.7

cm (LxWxH). Compared to the first iteration, the design improves the mechanical design, motor power, communications capabilities, added an onboard CPG to remove the tether and enhanced waterproofing. The top crawling and swimming speeds were measured to be 0.4 m/s and 0.23 m/s respectively. The actual swimming locomotion speed is notably lower than the result of a presented Webots based simulation of 0.87 m/s. After applying the gradient-free optimisation method, Powell's method, the undulation frequency was confirmed as the simplest parameter for controlling the locomotion speed. Further, it was found that the optimal locomotion gaits are not the same for crawling and swimming and that the optimal gait performance deteriorates rapidly when small changes are made to kinematic parameters (Crespi and Ijspeert, 2008).

The third iteration of the Amphibot was detailed by Porez et al. (Porez et al., 2014). The design shows an updated casing consisting of three elements (top, bottom and central) and each assembled module has dimensions of 9.7x5.7x4 cm (LxWxH). Similar to previous designs, waterproofing is achieved by means of an O-ring around a moving shaft. The presented robot configuration consists of 8 actuated elements with a density of 1 kg/m^3 to swim just below the water surface. Each module houses an identical set of electronics including a 0.57 Nm DC gear motor, a PD position controller and a water ingress detector. The upgraded joint design includes a spring connected between the drive shaft and a neighbouring segment to form a serial elastic actuator. Experimental swimming results show a significantly improved maximum locomotion speed of 0.59 m/s.

The modular design of the Amphibot has further been used in the Boxybot (Lachat et al., 2006). In this case, a robot is fitted with two pectoral fins and a caudal fin with general inspiration from the boxfish and the Envirobot (Bayat et al., 2016) fitted with water sampling sensors.

Designed originally as a crawling snake robot, the Mamba was first published in 2014 (Liljebäck et al., 2014). The presented design consists of 12 jointed modules housed in a 3D printed casing produced using selective laser sintering. Each joint module weighs 310g and measures 70x70 mm (WxH) and measures 89 mm between the joint axes. The joints provide one degree of freedom at a max amplitude of 90 degrees. The

2.3 Nm DC motor torque achieves a no-load max turning speed of 428 degrees per second. Connected joints may be rotated so that the joint rotation is in yaw or pitch. The modules are waterproofed by means of an O-ring around the rotating shaft connection. Watertightness during swimming tests was achieved by a flexible cover (Kelasidi et al., 2018). The robot is powered and can communicate via a tether and Wi-Fi is also available. Experimental tests were conducted to investigate the locomotion efficiency and path following ability of the Mamba robot with and without a passive caudal fin (Kelasidi et al., 2018).

(a)

(b)

Figure 2.12 (a) Mamba Underwater Snake Robot, fitted with a watertight flexible cover, during experimental testing (Kelasidi et al., 2018), (b) CGI graphic of commercial bio-inspired AUV Eelume (Eelume AS, 2023).

Results confirmed the importance of the caudal fin that led to a forward velocity increase of 88% with relatively low change to the required input power. The maximum measured forward velocity was circa 0.26 m/s. Following the Mamba research, a commercial multi-actuated hybrid design, called the Eelume, was presented (Liljebäck and Mills, 2017). Taking a different approach to other modular designs, the modular structure includes thrusts achieving a maximum forward velocity of 2 m/s. The

medium size model weighing 75kg and operating at 300V has a depth rating of 150 mm. The joints are waterproofed by flexible covers and may also be oil filled to prepare for greater water depths. The system continues to be developed as an autonomous resident system (Eelume AS, 2023).

In 2009, the ACM-R5 was published by Yu and Wang (2009). The presented design consists of 9 body modules that each house an identical set of electronics. The DC motor driven joints each provide two degrees of freedom in coupled or decoupled yaw and pitch. The system includes wheels on the outside of modules to enable crawling on land and is made watertight by O-rings and a flexible cover around the joints for swimming in water. The battery powered system has two separate 5V power sources for the control boards and the motors. The crawling and swimming speeds of the robot were recorded at 0.15 m/s and 0.07 m/s respectively.

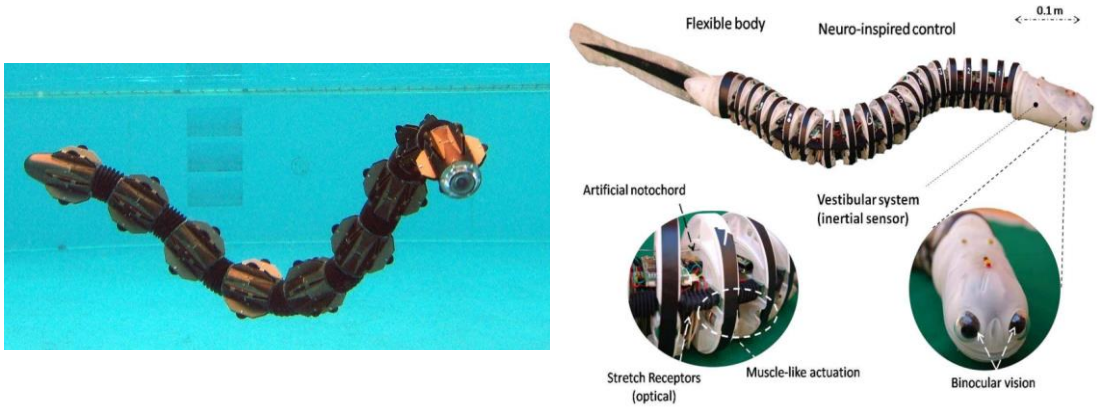

(a) (b)

Figure 2.13 (a) ARCM swimming underwater (Guizzo, 2013) (b) LAMPETRA – modular design using magnetic actuation (Stefanini et al., 2012).

A further notable design is the LAMPETRA published by Stefanini et al. (2012). A key novelty of the design is the magnetically actuated joints. Body undulation is achieved via magnets arranged laterally on either side of the robot that are rotated to attract and repel to enable the robot to curve locally. According to the authors, the use of magnets enables it to capture the passive dynamics in fish swimming. The presented design consists of 21 segments with a total robot length of 99 cm. The maximum recorded swimming speed is circa 0.6 m/s and the maximum body curvature has a radius of 75 mm for manoeuvring and obstacle avoidance.

Work by Mintchev et al. (2012) presents a modular bio-inspired autonomous vehicle where the individual modules are design to be able to decouple and couple to either swim independently or docked together. The systems, shown in Figure 2.14, presents a novel hybrid joint design consisting of small permanent magnets for 3D alignment underwater and a mechanical screw connection.

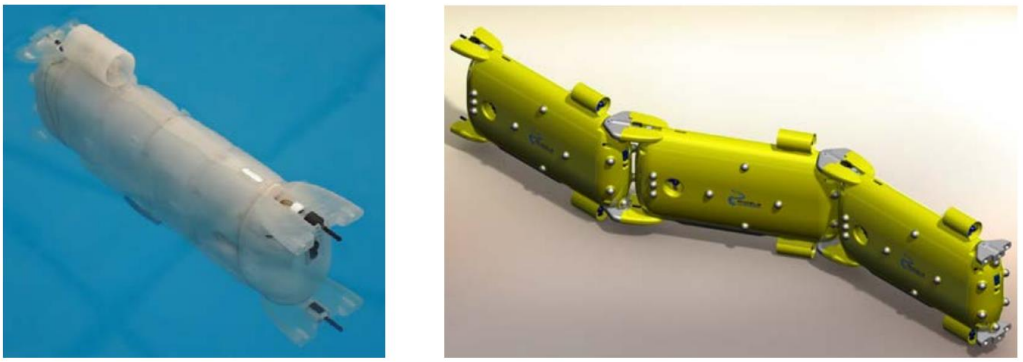

Figure 2.14 Modular anguilliform AUV design able to couple and decouple body modules (Mintchev et al., 2012).

2.7 Concluding remarks

The literature review highlights the interdisciplinary nature of understanding how fish swim efficiently and how to build efficient bio-inspired underwater robots. Current designs continue to fall short of performances exhibited by their natural inspiration and more research work is needed. A wide variety of simulation tools have been developed to simulate fish locomotion, including a Volume of Fluid (VoF) based solver, the Immersed Boundary Method and an ML based solver. Overall, CFD provides an excellent research platform for improved understanding of fish related fluid mechanics. Coupling CFD simulations with multi-body dynamics remains a novel approach to study multi-body systems with active and passive joints, such as bio-inspired fish-like robots. Adding feedback control provides further novelty to enable new dynamic simulations of steady and unsteady swimming. The CFD multi-body and control high-fidelity environment is capable of capturing both the hydrodynamics and robotic control of fish-inspired robots. Enhanced control of the swimmer's motion within the simulation supports analysis of unsteady swimming, an area of fish swimming with significant knowledge gaps. A few early studies combining CFD simulation with feedback control have shone a light on the great potential this

field of research has to offer. However, more research work is required for a better understanding of efficient fish propulsion and manoeuvrability.

This literature review shares examples of the wide range of bio-inspired underwater robots that have been built in the past. A detailed review of eel or snake-like modular bio-inspired robots highlights the specific interest in anguilliform swimming and the mechanical aspects of this locomotion category. The majority of designs achieve watertightness using O-rings and/or flexible covers. These are subject to wear and tear and may provide insufficient protection in deep waters. Moreover, it may prove challenging to access, repair and replace individual modules. More work is required to mature designs and optimise swimming performance.

Bio-inspired robotics have shown superior manoeuvrability compared to conventional rigid systems. However, knowledge gaps require further research into optimal body curving of manoeuvring BCF swimmers.

In summary the following gaps have been identified:

- Few studies have coupled numerical simulations with feedback control.
- Few studies have combined high fidelity hydrodynamic control and analysis.
- No study has focused on the optimal body curvature envelope of BCF manoeuvring.
- No performance coefficient for manoeuvring that includes the turning radius has been proposed.
- Few studies have focused on unsteady swimming locomotion.

As a result, this work has the following objectives*:*

Numerical investigation:

- Establish linear feedback control logic for bio-inspired swimmer control scenarios.
- Establish CFD simulation coupled with linear feedback algorithms to model a modular bio-inspired underwater vehicle.

- Apply control strategies in numerical investigations related to bio-inspired underwater locomotion.

Experimental investigation:

- Design and build of a bio-inspired robot prototype.
- Experimental hydrodynamic lab testing of a bio-inspired robot prototype.

Chapter 3 Numerical modelling and control of BCF swimmers

3.1 Computational Fluid Dynamics

Computational Fluid Dynamics describes the field of solving fluid governing equations numerically to study and understand fluid flow related problems. Compared to experimental studies it requires less effort to investigate large parameter spaces and models at different scales. The significant computational cost is compensated by highly detailed, transient, discrete flow information that is essential to solving modern fluid dynamics optimisation and design engineering challenges.

Mathematically, fluid flow may be described by a set of partial differential equations that are derived from the conservation laws of mass, momentum and energy (Ferziger et al., 2019). Analytical solutions to these equations may only exist for simplified assumptions (Lighthill, 1971) (Wu et al., 2014) and non-complex geometries which lead to inaccuracies. CFD combines mathematics, physics and computer science to create powerful algorithms to simulate fluid dynamic systems with high spatial and temporal resolution to a high degree of accuracy (Ansys Fluent, 2021). This work focuses on the investigation of the fluid structure interaction of feedback controlled, multi-actuated, bio-inspired underwater robots and the combined hydrodynamic and control analysis to determine optimal parameters for bio-inspired underwater propulsion. To model such a complex system, both the fluid dynamic system and the body dynamic system need to be resolved in a coupled computational platform.

This work uses the commercial CFD package Ansys Fluent (Ansys Fluent, 2021) in combination with User Defined Functions (UDF). Throughout this work various versions of Ansys are used from version 17.2 to 22.2. The UDF interface makes it possible to integrate self-developed algorithms that describe the dynamics of a robot-like, bio-inspired flexible structure in combination with the fluid domain solver.

In the following, the fluid governing equations, a mesh quality and dynamic meshing strategy as well as the applied solver scheme and UDF coupling are explained. Further,

algorithms of single and multi-body systems are introduced in detail and a reference is given to a coupled fluid and structure solver.

3.1.1 Fluid dynamics governing equations

Based on the work by Ferziger and Peric (2019), the transportation equation describes the transport mechanism of a scalar quantity ϕ within a fluid. The general form of the transportation equation is given by

$$\frac{\partial}{\partial t}\int_V (\rho\phi)dV + \int_V (\rho\phi\boldsymbol{u})\cdot d\boldsymbol{A} = \int_V (\Gamma \operatorname{grad}\phi)\cdot d\boldsymbol{A} + \int_V S_\phi\, dV, \qquad (3.1)$$

$$\underset{\text{derivative term}}{\text{Time}} + \underset{\text{time}}{\text{Convective}} = \underset{\text{term}}{\text{Diffusive}} + \underset{\text{term}}{\text{Source}}$$

where V is an arbitrary fixed control volume, t is the time, $\boldsymbol{u} = (u, v, w)^T$ is a velocity vector, ρ is the fluid density and may be neglected according to the assumption of the incompressibility of water, $\boldsymbol{A}$ is the face area vector, Γ is a diffusion coefficient for ϕ, S_ϕ is the source term, and grad ϕ is the gradient of ϕ. From Equation (3.1) the mass and momentum conservation equations can be derived for $\phi = 1$ and $\phi = \boldsymbol{u}$ respectively. These equations are also known as the Naiver Stokes equations.

The general form of Equation (3.1) may be adjusted to represent the simulated case. Water is considered an incompressible and viscous Newtonian fluid. Therefore, the density term may be removed due to the incompressibility assumption of water. Combined with the assumption of mass conservation, this concludes to a divergent-free velocity field, meaning no source or sink. A detailed derivation of governing equations is available in the relevant literature.

3.1.2 CFD mesh and dynamic meshing

Mesh quality is of critical importance to achieve accurate and precise results in CFD simulations. Local solutions are calculated at the control volume centre; hence, a refined mesh increases the solution resolution and reduces the discretisation error. Extensive refinement leads to excessive computational cost. Instead, local grid refinement, such as those close to surface boundaries and other areas of interest,

provides local accuracy in areas of interest. A mesh dependency study compares simulation results for different levels of refinement to identify an optimal mesh in terms of mesh quality and computational cost.

Mesh quality criteria include the control volume aspect ratio (the ratio between the longest and the shortest edge), skewness (deviation from an ideal shape), orthogonality (angle between adjacent cell faces) and the expansion ratio between adjacent cells (rate of control volume increase between neighbouring cells).

Dynamic meshing allows for mesh adaptation and refinement around moving boundaries during the simulation to maintain high mesh quality. Mesh motion may appear in simulations of moving objects due to prescribed motion or, as presented in this work, as a result of fluid -swimmer interaction.

Mesh smoothing and remeshing options within Ansys Fluent are used throughout this work. For example, the Spring-Based Smoothing Method (Ansys Fluent, 2021) considers the mesh edges as springs. The spring force is given by Hook's law and is calculated as follows

$$\boldsymbol{F}_i = \sum_{j}^{n_i} k_{ij}\left(\Delta \boldsymbol{x}_j - \Delta \boldsymbol{x}_i\right), \tag{3.2}$$

where $\boldsymbol{F}_i$ is the spring force vector of the i-th mesh node, $\Delta \boldsymbol{x}_i$ and $\Delta \boldsymbol{x}_j$ are the displacements of node i and its neighbouring nodes numerated from index j to n_i. The spring stiffness is represented between node i and node j by k_{ij}. At equilibrium, in other words, the initial condition, the net spring force acting on the nodes is zero. To account for mesh node motion, the integral form of the incompressible, unsteady transport equation without source or sink is given by

$$\frac{\partial}{\partial t}\int_V (\rho\phi) dV + \int_{\partial V} (\rho\phi(\boldsymbol{u} - \boldsymbol{u_g})) \cdot d\boldsymbol{A} = \int_{\partial V} (\Gamma \operatorname{grad} \phi) \cdot d\boldsymbol{A} + \int_V S_\phi \, dV \tag{3.3}$$

where $\boldsymbol{u_g}$ is the mesh displacement velocity vector (Ansys Fluent, 2021).

The updated cell volume between the current and next time level, n and $n+1$ is calculated by

$$V^{n+1} = V^n + \frac{\partial V}{\partial t}\Delta t. \tag{3.4}$$

For the mesh to maintain the conservation law, the rate of volume change dV/dt is calculated by

$$\frac{\partial V}{\partial t} = \int_{\partial V} \boldsymbol{u_g} \cdot \partial \boldsymbol{A} = \sum_{j}^{n_f} \boldsymbol{u}_{g,j} \cdot \boldsymbol{A}_j, \tag{3.5}$$

where n_f denotes the count of faces within the control volume, $\boldsymbol{A_j}$ the area vector of the j face and $\boldsymbol{u}_{g,j}$ the mesh volume face velocity vector of node j.

3.1.3 Solver scheme & user defined functions

Solutions to the discretised Naiver Stokes equations can be obtained using iterative or non-iterative algorithms. Iterative numerical solvers approximate solutions to mathematical problems through a series of refinements, improving accuracy with each iteration until convergence is achieved. Direct numerical solvers, on the other hand, aim to find the exact solution in a finite number of steps, typically using methods like Gaussian elimination for systems of linear equations. To resolve the equations, the velocity field may be corrected by the pressure field using the so-called pressure-velocity coupling. Popular solver algorithms that employ a pressure-velocity coupling include the iterative algorithm, the Semi-Implicit Method for Pressure Linked Equations (SIMPLE), and the non-iterative algorithm Fractional Step.

Iterative and non-iterative solver time advancement schemes have their respective benefits and drawbacks, depending on the simulated case. Non-iterative solver algorithms are considered easier to implement and may provide faster and stable solutions. Figure 3.1 shows a combined process diagram of the fractional step solver including UDF macros in Ansys Fluent. Notable is the absence of outer iterations in contrast to the presence of inner iterations around the velocity solution and pressure correction.

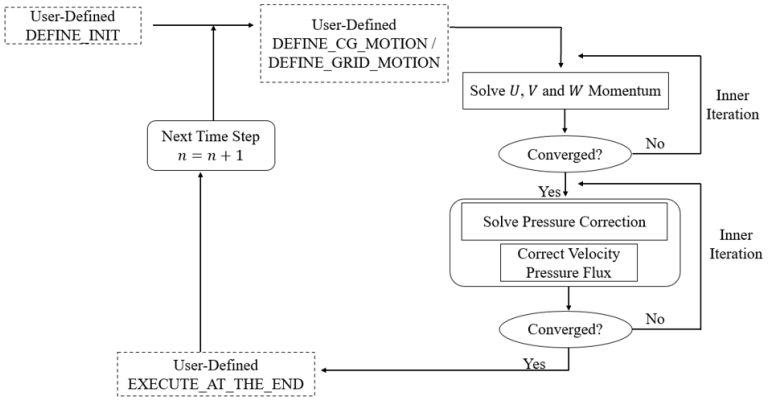

Figure 3.1 Ansys Fluent Fractional Step including a User Defined Function process diagram.

UDF macros enable online communication between a user created code and Ansys Fluent. Within the boundaries of the macros, users may create code that alters boundary conditions or moves surface nodes individually or groups of surface nodes. As shown in Figure 3.1 the macros DEFINE_INIT and EXECUTE_AT_THE_END are used to define the initial conditions at the beginning of the simulation and update calculations at the end of each time step respectively. The macros DEFINE_CG_MOTION and DEFINE_GRID_MOTION are used to define the motion of a centre of gravity of a rigid body and the movement of individual nodes of a flexible body.

3.2 Body dynamics models

Simulating a BCF swimmer in a virtual environment requires a mathematical description of the swimmer's body motion and dynamics. In this Section, mathematical models are introduced for self-propelled BCF swimmers. Coupling these models with feedback control achieves dynamic simulations of unsteady swimmer manoeuvres.

In addition to a single body algorithm, a more detailed multi-body algorithm is introduced; the latter is able to solve the internal and external dynamics including information on the torque of each joint. Reference is given to a coupled fluid and structure solver applied in the simulation of flexible structures present in bio-inspired robots as in, for example, caudal fins. Finally, time-discrete Proportional Integral and

Derivative (PID) control is introduced, and three different control strategies, used in the analysis of unsteady swimming, are introduced in Section 3.3.

BCF swimming is characterised by its periodic body motion. For a swimmer of total length, L, and $s \in [0, L]$ being the position along its central spine, it is possible to describe the periodic body angular or lateral displacement $\mathrm{y(t, s)}$ by

$$\mathrm{y(t,s)} = A(s)\sin(2\pi\,(-\mathrm{f\,t} + \varphi(\mathrm{s})) + C(s), \tag{3.6}$$

where $A(s)$ and $C(s)$ are the respective amplitude and curvature envelope functions, $\varphi(\mathrm{s})$ is the phase distribution defining the represented wavelength, f is the frequency and t is the time. Defining $A(s)$ makes it possible to represent different BCF swimming gaits, such as those shown in Figure 3.2. The definition of $\varphi(\mathrm{s})$ makes it possible to vary the represented different wavelengths as observed in nature, for example, for anguilliform $\varphi(\mathrm{s}) \geq 2\pi$ leads to an undulating body and thunniform $\varphi(\mathrm{s}) < 2\pi$ leads to a tail oscillating body.

Equation (3.6) describes the body motion of a continuous swimmer, so that s assumes the normal position of the surface nodes or a discrete multi-body swimmer where s assumes the value of the joint location. In the case of a single pitching or heaving foil, the amplitude function becomes the constant value of the trailing edge amplitude $A(s) = A_{TE}$.

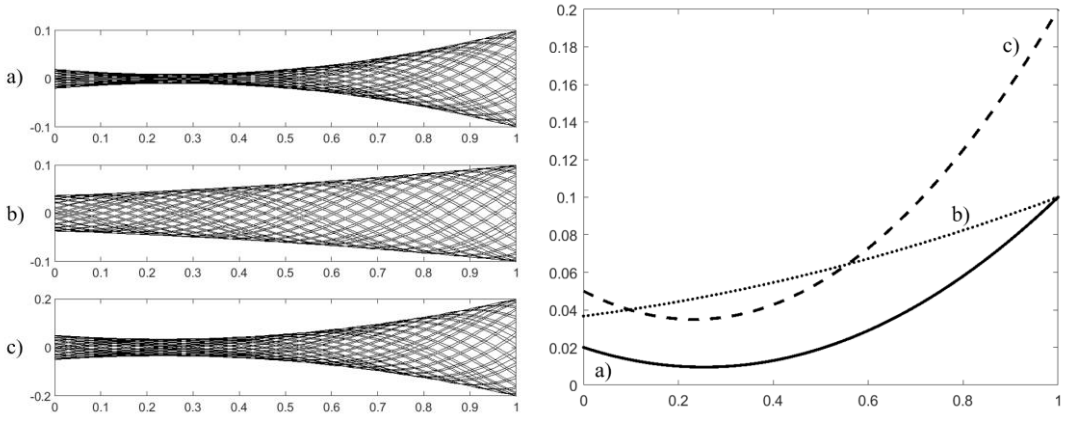

Figure 3.2 Author created graph of experimentally identified amplitude envelopes published by a) (Hess, 1983), b) (Tytell and Lauder, 2004), c) (Di Santo et al., 2021).

Figure 3.2 plots amplitude envelope functions of linear and quadratic orders derived through experimental observation by Hess (1983), Tytell and Lauder (2004) and Di Santos et al (2021).

An extensive numerical parametric study of a fish-like body by Maertens et al. (2017) found an exponential equation to be energetically optimal. Their findings highlight kinematic parameters to be highly affected by the swimmer's species, physique and behaviour, so it is not possible to make a general statement on the optimal kinematic parameters. No clear definition of a curvature envelope $C(s)$ was found by the authors. The curvature envelope of bio-inspired robot fish is addressed in a numerical investigation in Section 4.1.

3.2.1 Single body model

The presented 2D single body model is based on a publication by Carling et al. (1998). The model considers a fish like swimmer as a single body entity, in which body flexibility is established through coordinated motion of surface nodes. The model captures body shape related changes to the centre of mass as well as the mass moment of inertia coupled with a CFD environment. It is also able to capture the 2D linear and angular global motion as a result of fluid structure interaction due to body shape changes. Figure 3.3 shows the trapezoid shaped swimmer within the local (x_s, y_s) and global (x, y) coordinate systems.

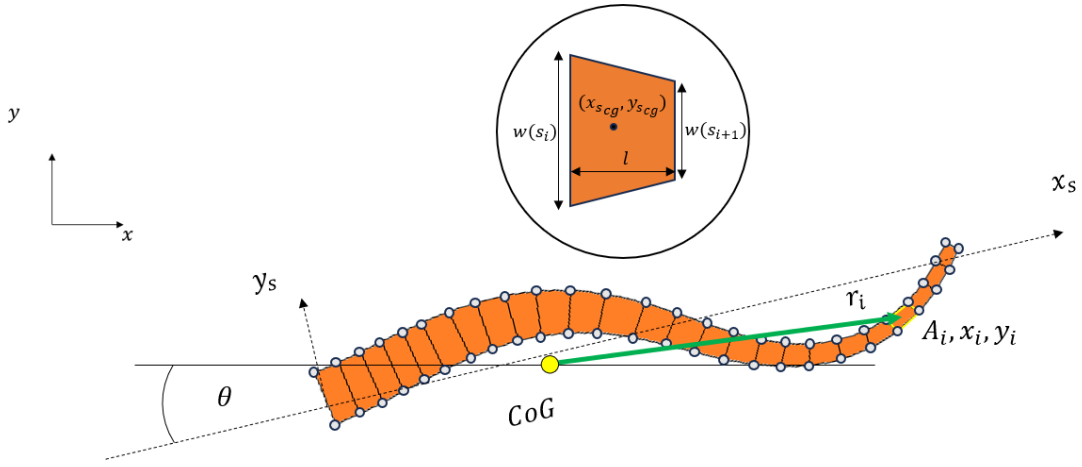

Figure 3.3 Single Body model according to Carling et al. (1998).

All trapezoidal elements are of equal height, denoted as l, corresponding to equally spaced surface mesh nodes. According to Carling et al. (1998), a trapezoidal body geometry is described by

$$w(s) = w_0 - (w_0 - w_1)\left(3 - \frac{2s}{L}\right)\frac{s^2}{L^2}, \tag{3.7}$$

with coefficients $w_0 = 0.64$ and $w_1 = 0.16$ and an overall length of $L = 1$.

By changing Equation (3.7), it is possible to represent other geometries, including the NACA0012. To maintain mass conservation, the horizontal node motion Δx_s is calculated by

$$\Delta x_s = \sqrt{l^2 - y(s,t)^2} \tag{3.8}$$

The swimmer's total centre of mass coordinates are calculated by

$$x_{cg} = \frac{\sum A_i \, x_{s_{cg}}}{\sum A_i} \tag{3.9}$$

$$y_{cg} = \frac{\sum A_i \, y_{s_{cg}}}{\sum A_i} \tag{3.10}$$

where A_i, $\mathrm{x}_{s_{cg}}$ and $\mathrm{y}_{s_{cg}}$ are the trapezoid centre of gravity coordinates, which are calculated by

$$x_{s_{cg}} = \frac{(w(s_i) + w(s_{i+1}))}{3(w(s_i) + w(s_{i+1}))}\, l, \tag{3.11}$$

$$y_{s_{cg}} = y_s(s_i), \tag{3.12}$$

$$A_i = \frac{(w(s_i) + w(s_{i+1}))}{2}\, l. \tag{3.13}$$

Variables $w(s_i)$ and $w(s_{i+1})$ are the trapezoid base values and l is considered the trapezoid element height. The mass moment of inertia is given by

$$I = m\,r^2 = A\,\rho\,r^2 = \sum A_i\,\rho\,r_i^2, \tag{3.14}$$

where m is the mass that can also be written as the product of Area A and density ρ, and r is the radius of gyration calculated by

$$r_i = \sqrt{\left(x_{s_{cg}} - x_{cg}\right)^2 + \left(y_{s_{cg}} - y_{cg}\right)^2}. \tag{3.15}$$

Global motion in the plane and one degree of rotation is then calculated by solving Newton's second law, using the force and moment calculated by the CFD simulation, and integrating the linear and angular acceleration terms using the Euler integration method.

Linear acceleration vector $\boldsymbol{a}$, velocity vector **u** and displacement vector $\boldsymbol{x}$ at time step t+1 are derived through Euler integration as follows

$$\boldsymbol{a_t} = \frac{\boldsymbol{F}}{m}, \qquad \boldsymbol{u_{t+1}} = \boldsymbol{u_t} + \boldsymbol{a_t}\Delta t, \qquad \boldsymbol{x_{t+1}} = \boldsymbol{x_t} + \boldsymbol{u_t}\Delta t, \tag{3.16}$$

and angular acceleration α, velocity ω and displacement θ are given by

$$\alpha_t = \frac{M_{z,t}}{I}, \qquad \omega_{t+1} = \omega_t + \alpha_t\Delta t, \qquad \theta_{t+1} = \theta_t + \omega_t\Delta t \tag{3.17}$$

The implementation within a UDF is given in APPENDIX A.

3.2.2 Single body model validation

The established coupled single body CFD simulation is validated against the reference case published by Carling et al. (1998). This publication has been used as a reference case by different researchers, such as Kern and Koumoutsakos (2006) using the commercial solver Star CCM+ and Bhalla et al. (2013) and Zhang et al. (2018) using the immersed boundary solver method. Notably, the work of Carling et al. (1998), Kern and Koumoutsakos (2006), Zhang et al. and Bhalla et al. (2018) all show minor differences in the used geometry function and actuation function, which may be explained by the different solver methods employed.

In this work, the numerical setup consists of a swimmer moving through still water by means of self-propulsion through a walled virtual tank represented by the CFD computational domain. The swimmer is set up according to the geometry function described in Zhang et al. (2018) and has a total length of $L = 0.01$ m and the CFD domain dimensions are 0.32x2m (HxW). The Reynolds number is equal to $Re = 52$.

Figure 3.4 shows the $30\ L$ by $8\ L$ mesh domain discretised into 35967 triangular cells. A time step of $\Delta t = T/250$, with T being the undulation cycle period, was selected to satisfy the Courant–Friedrichs–Lewy (CFL) criteria, defined as the ratio between flow speed times fluid velocity over mesh spacing (De Moura and Kubrusly, 2013). The CFL number ensures that the scalar information travelling distance over one time step is shorter than the smallest mesh distance, which provides feedback on the suitable mesh dimension and time step selection. Vertical domain boundaries are defined as velocity inlet and pressure outlet and the horizontal boundaries are set with a symmetry condition. The inlet velocity is zero.

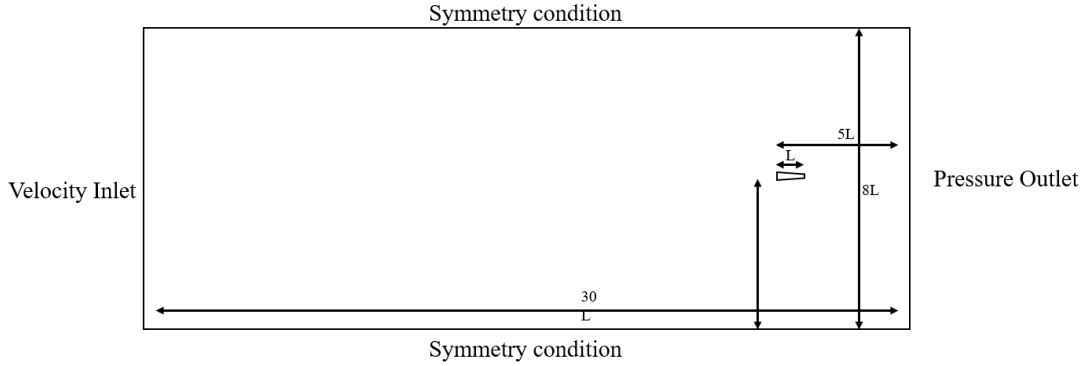

Figure 3.4 Schematic of the single body validation case CFD domain setup.

The solution is calculated using the NITA pressure-velocity coupling Fractional Step. A least-square-cell-based approach is selected for spatial discretization, and a second-order upwind scheme for discretization of the diffusive term. A second-order pressure interpolation is selected for improved accuracy.

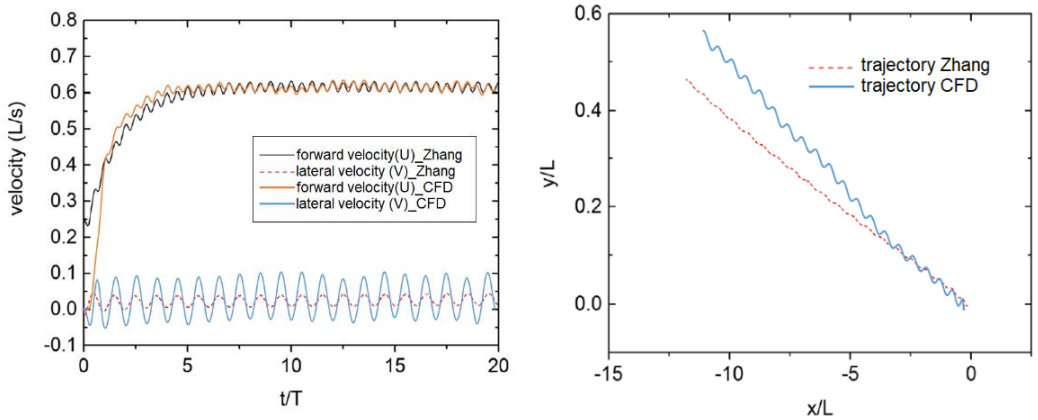

(a) (b)

Figure 3.5 Validation against (Zhang et al., 2018) for (a) an instantaneous forward and lateral velocity comparison and (b) displacement.

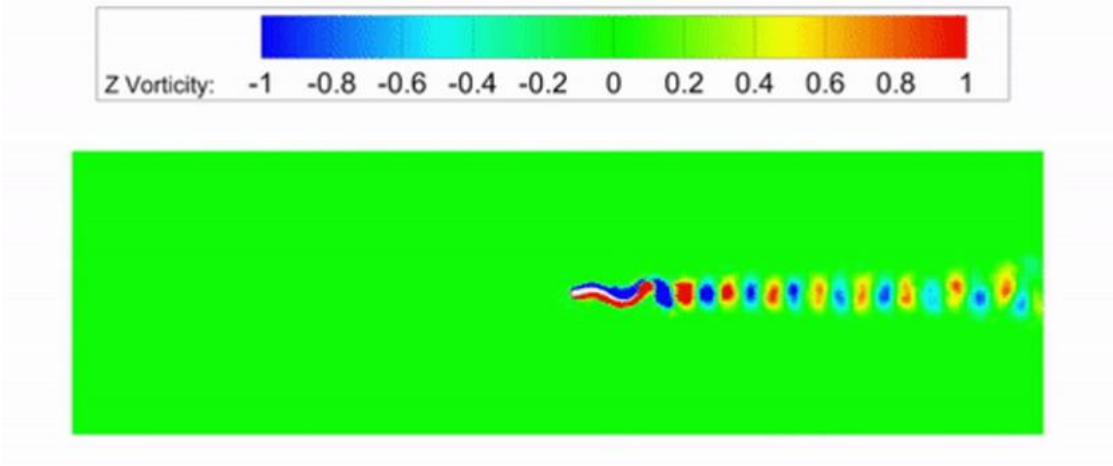

Figure 3.6 Section of the simulation domain showing a z-vorticity contour at T= 9 showing the forward displaced swimmer and reversed Karman vortex street in its wake.

Figure 3.5 (a) shows an overlay between the simulation results and the results of the instantaneous velocities published by Zhang et al. (2018).The simulation results achieve overall good agreement with the reference cases in terms of the predicted horizontal and vertical velocity. Comparison of the centre of gravity displacement, in Figure 3.5 (b), exhibits an overall good agreement between the simulation and the reference case. While an exact match is given up to $x/L = -4$ before diverging slightly from the reference trajectory.

Figure 3.6 plots the Z-vorticity, clearly showing the displaced swimmer and the reversed Karman vortex street in the swimmer's wake.

3.2.3 Multi-body model

The single body model does not capture any of the internal dynamics relating to muscle actuation in real fish or the joint and motor actuation of engineered systems. In the following, a more detailed approach to modelling a bio-inspired swimmer is presented that was first published by Porez et al. (2014) and later adopted into a CFD environment by (Hu, 2016) and further developed by (Li et al., 2018). Note, it is possible to apply the presented system to a three-dimensional problem; however, due to computational expense constrains it is applied in 2D problems throughout this work. To highlight the significant computational expense of the conducted CFD simulations, the simulation of Section 3.2.2 requires around 6-7 hours simulation time. Expanding this simulation into three-dimensional space significantly increases the number of mesh cells and dynamics equations, which would result in significant more simulation time of several days to potentially weeks.

The multi-body actuated robotic structure consisting of n+1 elements and n rotating joints are modelled in the Newton-Euler form, which covers the translational and rotational dynamics of a connected multi-body structure. The presented algorithm can accommodate serial and tree-like structures, but sole focus is placed on serial structures in this document. Figure 3.7 shows a process diagram of the recursive algorithm, which is explained in detail in the following.

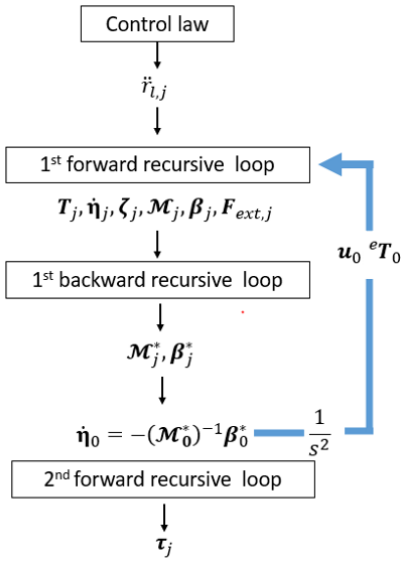

Figure 3.7 Flow chart of the multi-body algorithm

As shown in Figure 3.8, the multi-body arrangement consists of a fixed global coordinate system O_e (X_e, Y_e) and n local coordinate systems $\mathcal{F}(O, a, s, n)$, with the 2D base plane formed by $\mathcal{F}(O, a, s)$. By convention, the local frames are in front of each element at half distance between the body elements at mid height. In the case of a continuous body, the local coordinate systems are placed on the front boundary of the body element. The local frames are numbered starting from the first body B_0 with frame $\mathcal{F}_0$ that acts as the overall reference of the moving structure with respect to the global frame. The current frame is indicated by the upper left index of the variable and the acting body of the variable in the lower right index. In the case where they coincide, the upper left one is omitted. The currently viewed frame is denoted as j, with $j-1=i$ and $j+1=k$ being the ascending and descending bodies respectively. The global coordinate frame is denoted by index e. (Example: ${}^{e}\boldsymbol{u}_j$ is the velocity of body j projected in the global frame, $\boldsymbol{u}_j$ is the velocity body j projected in the local frame, ${}^{i}\boldsymbol{u}_j$ is the velocity body j projected in the ascending frame).

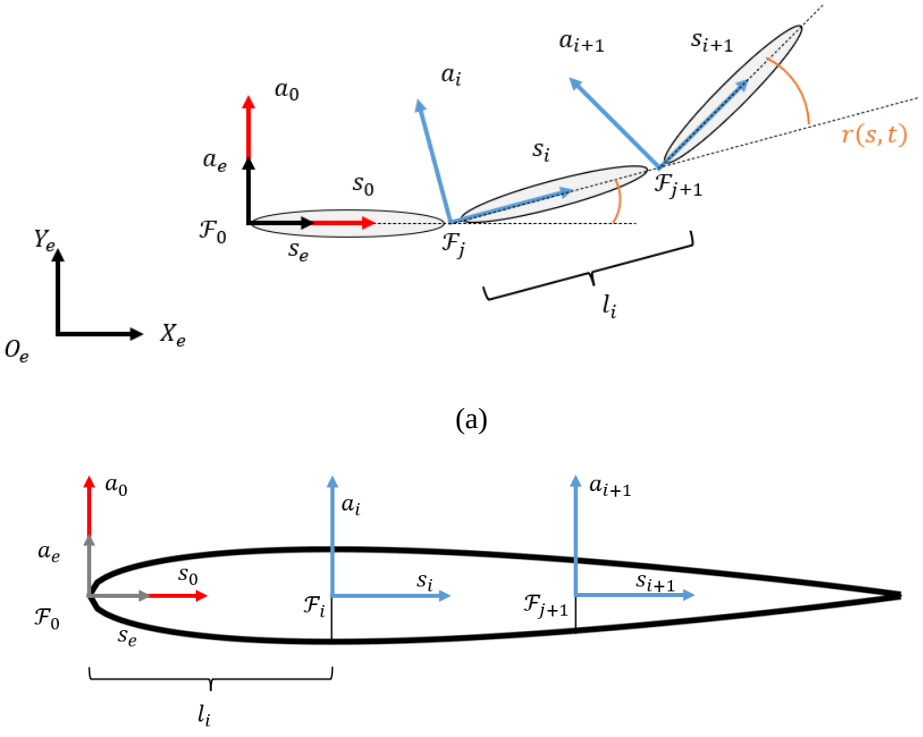

Figure 3.8 Relation between global, local and reference coordinate systems and the relative rotation between joints of (a) discrete and (b) continuous multi-body system

Transformation between global and local or neighbouring local coordinate systems is given by the relation in Equation (3.18). The 4x4 matrix ${}^{e}_{\square}\boldsymbol{T}_j$ of a three-dimensional Euclidean space $\mathbb{R}^3$ is a homogenous transformation matrix consisting of the orientation matrix $\boldsymbol{R}$ and position vector $\boldsymbol{P}$. The presented equation translates body *j* from the local coordinate system i to the global coordinate system

$$ {}^{e}\boldsymbol{T}_j = {}^{e}\boldsymbol{T}_i {}^{i}\boldsymbol{T}_j(r_j) = {}^{e}T_i \begin{pmatrix} {}^{i}\boldsymbol{R}_j(r_j) & {}^{i}\boldsymbol{P}_j \\ 0 & 1 \end{pmatrix}. \tag{3.18} $$

The orientation matrix $\boldsymbol{R}$ is composed of a rotation $\left(rot(n, r_j)\right)$ and a translation $\left(trans(s, l)\right)$ with reference to axis s and a.

$$ {}^{i}\boldsymbol{T}_j = trans(s, l) rot(n, r_j) = \begin{pmatrix} {}^{i}\boldsymbol{R}_j(r_j) & {}^{i}\boldsymbol{P}_j \\ 0 & 1 \end{pmatrix}. \tag{3.19} $$

The 6x6 adjoint map operator, given in Equation (3.20), is used to transform inertia, force and velocity from body $\mathcal{F}_i$ to $\mathcal{F}_j$. It contains the (3x3) skew matrix $\widehat{\boldsymbol{P}}$ of the position vector:

$$ \boldsymbol{Ad}_{j_{T_i}} = \begin{pmatrix} {}^{j}\boldsymbol{R}_i & {}^{j}\boldsymbol{R}_i {}^{i}\widehat{\boldsymbol{P}}_j^T \\ 0 & {}^{j}\boldsymbol{R}_i \end{pmatrix}. \tag{3.20} $$

The current state of the system is given by the state vector $\boldsymbol{X}_{state} = ({}^{e}_{\square}\boldsymbol{\eta}_0, {}^{e}_{\square}\boldsymbol{P}_0, \boldsymbol{Q}, \dot{\boldsymbol{r}}, \boldsymbol{r})$, which describes the state of the reference body including the velocity ${}^{e}_{\square}\boldsymbol{\eta}_0$, position ${}^{e}_{\square}\boldsymbol{P}_0$ and quaternion orientation $\boldsymbol{Q}$ as well as a vector of all joint rotation velocities $\dot{\boldsymbol{r}}$ and joint rotation angle $\boldsymbol{r}$.

As presented in a flow chart in Figure 3.7 and starting from initial conditions, the state vector $\boldsymbol{X}_{state}$ is updated at each time step through three recursions along the element structure and a numerical integration at the end. The presented equations apply active joint actuation.

The dynamics equation of the current body *j* in the NE frame is given by

$$ \boldsymbol{F}_j = \boldsymbol{\mathcal{M}}_j \dot{\boldsymbol{\eta}}_j + \boldsymbol{\beta}_j + \boldsymbol{F}_{ext,j} + \sum_k \boldsymbol{Ad}^T_{k\,T_j} \boldsymbol{F}_k \tag{3.21} $$

The frame transformation matrix variables ($\overset{i}{\square}\boldsymbol{R}_j$, $\overset{i}{\square}\boldsymbol{P}_j$, $\overset{e}{\square}\boldsymbol{T}_j$, $\overset{i}{\square}\boldsymbol{Ad}_{j_{T_i}}$), the velocity vector ($\boldsymbol{u}_j$), the acceleration term containing only velocity elements ($\boldsymbol{\varsigma}_j$), the inertia tensor matrix ($\boldsymbol{\mathcal{M}}_j$), the inertia force vector ($\boldsymbol{\beta}_j$) and the external force vector ($\boldsymbol{F}_{ext,j}$) are updated in the first recursion starting from the reference element B_0 along the body. Here, $\boldsymbol{F}_{ext,j}$ is determined through the coupling with the CFD environment.

The inertia tensor matrix $\boldsymbol{\mathcal{M}_j}$ is calculated by

$$\boldsymbol{\mathcal{M}_j} = \begin{pmatrix} \boldsymbol{M_j} & -\boldsymbol{MS_j} \\ \boldsymbol{MS_j} & \boldsymbol{I_j} \end{pmatrix}, \tag{3.22}$$

Where $\boldsymbol{M_j}$ is the body mass tensor, $\boldsymbol{MS_j}$ is the tensor of the first inertia moments, and tensor of angular inertia $\boldsymbol{I_j}$.

The combined inertia tensor $\boldsymbol{\mathcal{M}}_i^*$ and the cumulated force vector $\boldsymbol{\beta}_i^*$ of two neighbouring bodies B_i and B_j are calculated using the Equations (3.23) and (3.24).

$$\boldsymbol{\mathcal{M}}_i^* = \boldsymbol{\mathcal{M}}_j^* + \boldsymbol{Ad}_{i\ T_j}^T \boldsymbol{\mathcal{M}}_j^* \boldsymbol{Ad}_{i_{T_j}}, \tag{3.23}$$

$$\boldsymbol{\beta}_i^* = \left(\boldsymbol{\beta}_j + \boldsymbol{F}_{ext,i}\right) + \boldsymbol{Ad}_{i\ T_j}^T \left(\boldsymbol{\mathcal{M}}_j^* \left(\boldsymbol{U_j}\ddot{\boldsymbol{r}}_j + \boldsymbol{\zeta}_j\right) + \boldsymbol{\beta}_j^*\right). \tag{3.24}$$

Here, $\boldsymbol{U}_j$ is a (6x1) unit vector. The second recursion from the end of each branch back to the reference body establishes a combined inertia tensor $\boldsymbol{\mathcal{M}}_j^*$ and the cumulated force vector $\boldsymbol{\beta}_j^*$ of the reference body. Both terms establish an expression for the acceleration of the reference body in the local coordinate system of the overall structure

$$\dot{\boldsymbol{\eta}}_0 = -\left(\boldsymbol{\mathcal{M}}_0^*\right)^{-1} \boldsymbol{\beta}_0^*. \tag{3.25}$$

The third recursion, starting from the reference body along each branch, calculates the required joint torque

$$\boldsymbol{\tau}_j = \boldsymbol{U}_j\left(\boldsymbol{\mathcal{M}}_j^*\dot{\boldsymbol{\eta}}_j + \boldsymbol{\beta}_j^*\right). \tag{3.26}$$

Both the external and internal states of the system are stored in the state vector X_{state}. The external state is defined by its global orientation and position. The internal state is given by the joint velocities and angle after the first two recursions $\dot{\boldsymbol{X}}_{state}=\left({}^{e}\dot{\boldsymbol{\eta}}_0, {}^{e}\dot{\boldsymbol{P}}_0, \dot{\boldsymbol{Q}}, \ddot{\boldsymbol{r}}, \dot{\boldsymbol{r}}\right)$ are known. The 4th order Runge-Kutta method is used to find the internal and external states of the system at the next time step $t + \Delta t$

$$\begin{aligned}\boldsymbol{X}_{state}|_{t+1} = \boldsymbol{X}_{state}|_t \\ + \frac{\Delta \mathrm{t}}{6}\Bigg(\dot{\boldsymbol{X}}_{state}|_t^1 + 2\,\dot{\boldsymbol{X}}_{state}|_{t+\frac{\Delta \mathrm{t}}{2}}^2 + 2\,\dot{\boldsymbol{X}}_{state}|_{t+\frac{\Delta \mathrm{t}}{2}}^3 \\ + \dot{\boldsymbol{X}}_{state}|_{t+\Delta \mathrm{t}}^4\Bigg).\end{aligned} \tag{3.27}$$

3.2.4 Multi body algorithm validation

The presented multi-body CFD simulation setup has been used in different bio-inspired aquatic swimming simulations in the past (Hu et al., 2021;Li et al., 2018;Hu, 2016). To provide additional verification of the numerical method, a validation simulation was performed in line with the reference case published by Deng et al. (2007). Results are compared for predicted pressure and friction drag components of an undulating NACA0012 foil at Re = 500. The foil follows a prescribed motion according to Equation (3.6) with amplitude envelope $A(s) = 0.2s$ and frequency and phase distribution represented by the phase speed, in other words, $cp = 2\pi f/k$, where $k = 2\pi/\lambda$ is the wave number, λ is the wavelength and f is the frequency.

The model is setup up according to the reference case Reynolds number resulting in a swimmer length of $L = 1\,m$, inlet velocity of $0.5\frac{m}{s}$ and kinematic viscosity of $0.001003\frac{m^2}{s}$. The solver setup corresponds to the single body validation case in that the least-square-cell-based approach and the second-order upwind scheme are selected for spatial discretisation and discretisation of the diffusive term respectively. Also, a second-order pressure interpolation is selected for improved accuracy.

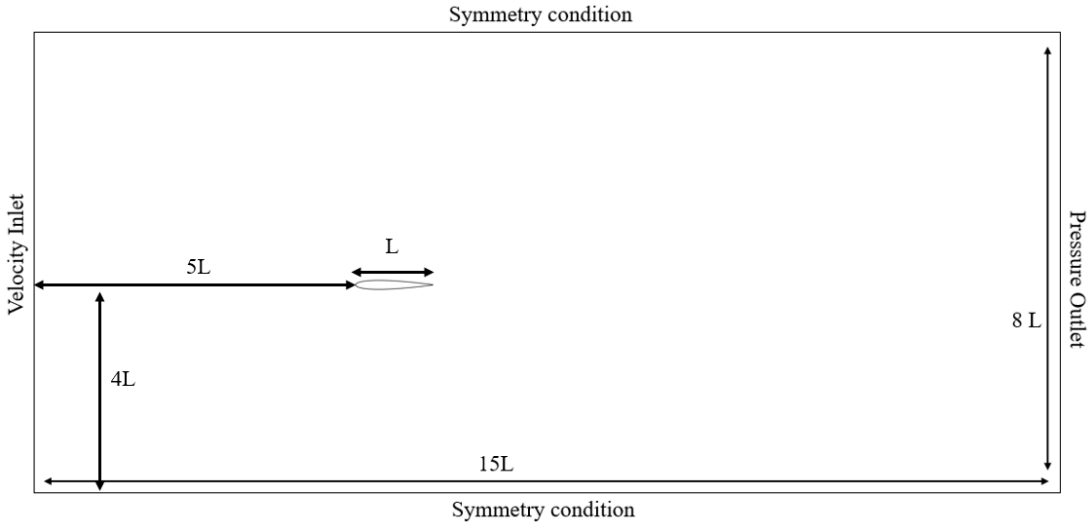

Figure 3.9 Schematic of the multi body validation CFD domain setup.

Figure 3.9 shows the setup CFD domain of size 15 L by 7 L and the swimmer positioned vertically centred 5L from the inlet boundary. The domain is discretised into 65309 cells and a timestep of $\Delta t = T/1000$, with T being the time period of one undulation. Figure 3.10 shows the comparison for the drag coefficient c_D as well as the pressure and friction drag coefficients. An overall good agreement is achieved. Results show an increase in negative drag coefficient, in other words, thrust, for increased foil phase speed. The dominant factor is the pressure drag, the friction drag is only slightly increased.

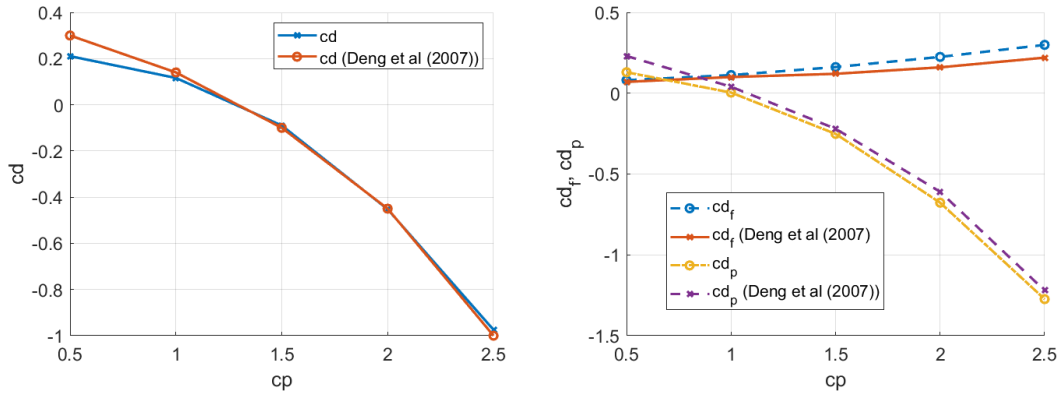

(a) (b)

Figure 3.10 Predicted results in comparison with data from Deng et al. (2007). (a) total drag coefficient. (b) pressure and friction drag coefficients.

3.2.5 CFD FSI model

The work presented in Section 4.2 and 4.3 applies PID control to a CFD FSI solver developed by Dr Luo Yang (2021) that combines an in-house developed CFD code with the open source structure Finite Element Analysis (FEA) solver CalculiX (Dhondt, 2017) via the coupling library preCICE (Bungartz et al., 2016). The author of this work was responsible for control design in full and result analysis in part. A schematic of partitioned multi-physics simulations is shown in Figure 3.11.

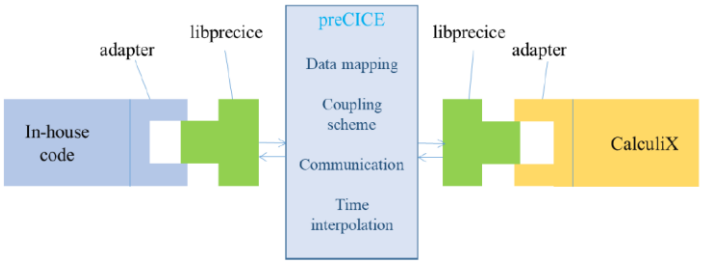

Figure 3.11 Schematic of coupling between in-house CFD code (Luo, 2021) and open-source structure solver CalculiX (Dhondt, 2017) using the coupling library preCICE (Uecker) (Uekermann et al., 2017).

For full details about the mathematical background, validation results and implementation, please refer to the PhD thesis by Luo Yang (2021). In the following, only a brief description of the methodology is given. The CFD FSI setup makes it possible to simulate non-prescribed elastic displacement, which is visible in nature in, for example, fish caudal or pectoral fins.

The two-dimensional simulations consist of a fluid and structure mesh domain connected through a common mesh interface. Each domain is governed by separate governing equations and is solved independently, yet solutions are communicated through a coupling library and convergence is ensured in an iterative process.

Figure 3.12 shows the general model setup, consisting of a two-dimensional quadrilateral cross-section of a truncated caudal fin viewed from the top. It is noted that although the considered geometry is two-dimensional previous studies indicated that the effect patterns of the stiffness on the propulsion performance are similar both in two- and three-dimensional models (Hoar and Randall, 1978).

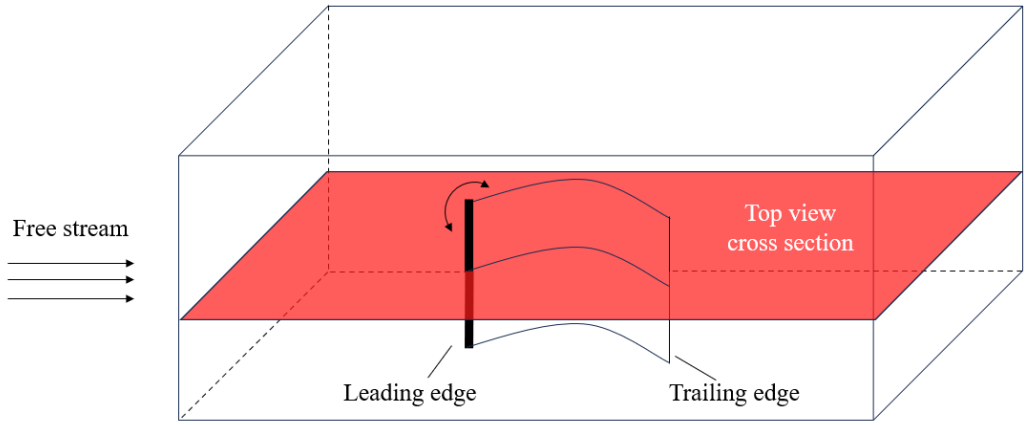

Figure 3.12 Simulation setup schematic showing the top view of the 2D cross section of a truncated caudal fin.

The fin is actuated to follow pitching motion at the leading edge according to Equation (3.30). and is allowed to move freely across the geometry including the trailing edge, subject to fluid structure interaction. The observed elastic displacement is influenced by pitching actuation amplitude and frequency as well as material characteristics such as the material density and stiffness. To be able to draw a general conclusion and enable the transferability of simulation results, dimensionless parameters governing this problem are defined as follows: the reduced frequency $f^* = fL/U$; the mass ratio $m^* = \rho_s h/\rho_f L$ with ρ_s and ρ_f the density of the structure and fluid respectively and h is the thickness of the fin; the dimensionless stiffness $K = EI/(\rho_s U^2 L^3)$where E is Young's modulus and $I = h^3/12$ is the area moment of inertia of the cross section.

3.3 Control design and strategies for BCF swimmers

3.3.1 BCF swimming feedback control

Robotic control describes the management and regulation of movements and actions. A robot, such as a bio-inspired robotic fish, relies on control input information to drive its actuators to perform tasks such as forward swimming and turning. It is possible to draw a general distinction between low level motor control and high-level motion control. Bio-inspired robots, including fish robots, mimic synchronised low-level

control of multiple actuators. Control commands are sent via remote control or derived within embedded autonomous control.

The most widely applied closed-loop control is the Proportional Integral and Derivative (PID) control (Bennett, 1993). The linear control method derives its name from dynamically calculating a control variable based on the proportional, integral, and derivative of a defined output tracking error signal. The classical PID controller was chosen for this work as it provides a robust choice of control, easy integration as well as low computation. Figure 3.13 shows a signal diagram of a PID feedback controller implemented in front of a CFD simulation. The feedback loop is created by feeding back output information of the plant, here represented by the CFD simulation. Within a feedback loop, the error signal is defined as the difference between the feedback signal and a setpoint. Based on the current error, the PID controller updates the control variable to control the system state within the CFD simulation.

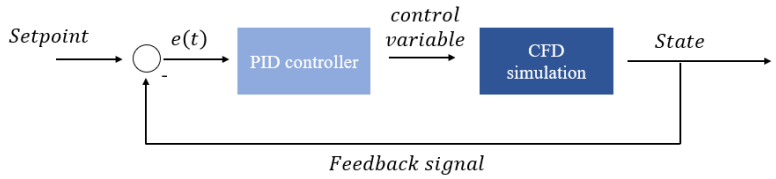

Figure 3.13 Signal flow diagram of the implemented feedback loop comprising the setpoint, PID controller and CFD simulation.

To couple a PID controller with a CFD simulated system, it must mirror the time discrete structure and be implemented as an additional calculation step at the beginning of each solver iteration. The discrete-time recursive PID is given by

$$u(t_k) = u(t_{k-1}) + \Delta u(t_k), \tag{3.28}$$

$$\begin{aligned}\Delta u(t_k) = K_p[e(t_k) - e(t_{k-1})] + K_I e(t_k) \\ + K_d[e(t_k) - 2e(t_{k-1}) + e(t_{k-2})].\end{aligned} \tag{3.29}$$

Here, K_P, K_I, K_D are the PID parameters, $e(t_k)$ is the control error at time k. The control parameters can be tuned to achieve the expected control response. Control parameters are hard to determine for complex systems, for example, for nonlinear, highly variable, high-order systems or systems with large uncertainties. For simple systems, the control parameters can be tuned using various methods, for example, ad-

hoc tuning gains are found through trial and error or the “Ziegler Nichols” tuning method, a heuristic method based on the system's response to a step input, aiming to achieve a desired balance between stability and performance (Ziegler and Nichols, 1942). Importantly, PID tuning can support the desired system response and ensure stability.

3.3.2 BCF swimming control strategies

High level motion control targets of a BCF fish robot may include a target position, orientation and their respective derivatives, which are achieved by means of low level control of the body motion. Synchronised low level control of bio-inspired motion may be achieved utilising a Central Pattern Generator (CPG) or a sine based approach (Crespi et al., 2008); the latter is applied in this work. Control variables of the sine-based approach are the amplitude $A(s)$, offset $C(s)$ and the arguments of the sine function determined by the phase φ(s) and the frequency f. Assuming a constant swimming gait function $A(s)$, the thrust and hence the speed may be controlled by scaling the amplitude magnitude by the factor $c_a \in [0,1]$. The heading direction can be changed by scaling a curvature envelope $C(s)$ by the factor $c_s \in [-1,1]$. A similar approach has been adopted by Martens et al. (2017). Adding the two scaling factors, the new input equation becomes

$$y(s,t) = c_a A(s) \sin\Big(2\pi\left(-ft + \varphi(s)\right)\Big) + c_s C(s). \tag{3.30}$$

Direct changes to the control variables $c_a$and c_s lead to unintended chaotic motion. In particular, changes to the sine arguments lead to an unsmooth transition when exceeding a change greater than π. To avoid dramatic changes and unintended chaotic motion, a cosine-based transition function is applied that provides smooth transitions over one oscillation period $\Delta t_l = T = \frac{1}{f}$ between different levels of c_a and c_s. Let $c_{control}$ represent either c_a or c_s

$$c_{\text{control}}(t_l) = c(t_{l-1}) - \frac{c(t_{l-1}) - c(t_l)}{2} \cdot \big(1 - cos\big(\pi \cdot t_{0,1}\big)\big), \tag{3.31}$$

where $c(t_{l-1})$ and $c(t_l)$ are samples of the control variable at the beginning of the previous transition period and at the beginning of the current transition period respectively. The time variable $t_{0,1}$ increments equal to the general time step but resets to 0 when reaching 1.

There are three individual time steps. Firstly, the numerical simulation time step denoted as $\Delta t_s = t_{s+1} - t_s$. Secondly, the controller sample time $\Delta t_k = t_k - t_{k-1}$. Thirdly, the controller update interval at $\Delta t_l = T = \frac{1}{f}$. Their values are defined so that $\Delta t_s \leq \Delta t_k < \Delta t_l$.

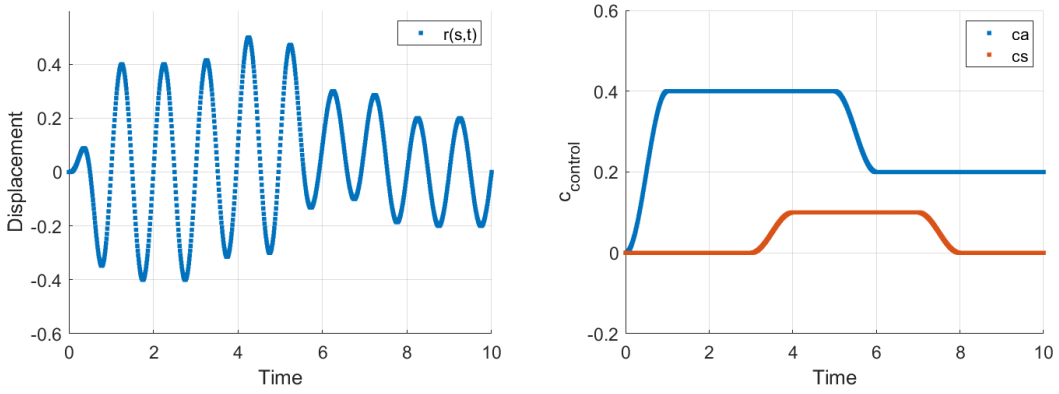

(a) (b)

Figure 3.14 (a) angular displacement and (b) corresponding $c_{control}$ function of c_a and c_s.

The curve in Figure 3.14 represents an example of the yaw displacement of a robotic joint. The figure shows a smooth transition for different levels of the amplitude coefficient c_a and the offset coefficient c_s.

Equation (3.30) does not require a global reference to produce motion; hence, it can be considered an open loop, where c_a and c_s are control inputs, because the control inputs are set without taking the systems current state into account. A PID controller enables setpoint tracking to calculate control inputs c_a and c_s to achieve, for example, a specified swimming speed and direction.

As can be seen in Figure 3.13, the PID controller calculates the control action based on the reference tracking error. By changing the definition of the error and setpoint it is possible to achieve different control targets. Generally, to compensate for periodicity

of the body undulation, the control error is averaged across all sampled values over one undulation cycle given by

$$e(t_n) = f \sum_{k=1}^{n} e(t_k)\,\Delta t_k. \tag{3.32}$$

Here, variables k and n describe the sample number from the first to the last sample within one undulation cycle period. In the following, three control scenarios are introduced with the aim of reducing the defined tracking error to zero. These control scenarios are applied in Section 4.

3.3.2.1 Scenario 1: velocity and thrust controller

Scenario 1 considers the scaling of the undulation amplitude by calculating the control variable c_a to adjust the generated thrust within calm water and against incoming velocity. For swimming in calm water, the control error may be defined as the difference between the current swimming velocity $\boldsymbol{u}(\boldsymbol{t})$ and the desired velocity $\boldsymbol{u}_{set}$

$$e(t) = \boldsymbol{u}_{set} - \boldsymbol{u}(t). \tag{3.33}$$

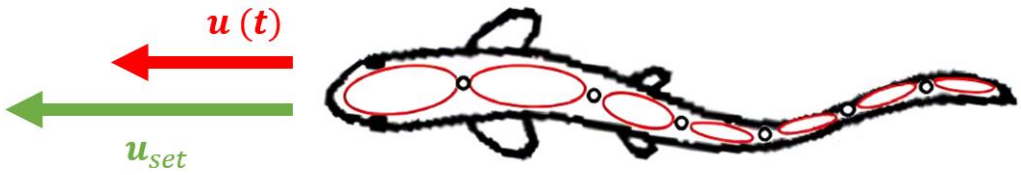

Figure 3.15 Control logic schematic of swimming velocity control.

Alternatively, when the swimmer is subject to incoming fluid flow it is possible to achieve a quasi-steady state swimming velocity by equalling the mean thrust and drag forces. Therefore, the scaling factor may be calculated by the PID controller by setting the control error to be the balance of thrust and drag force, also represented by the thrust coefficient.

$$e(t) = c_{T,set} - c_T(t) \tag{3.34}$$

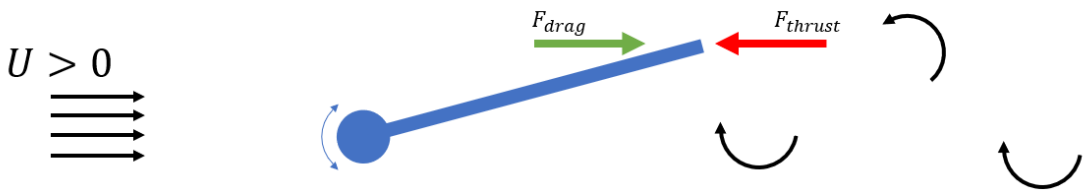

Figure 3.16 Control logic schematic of thrust coefficient equilibrium control.

3.3.2.2 Scenario 2: waypoint tracking

Body curvature is a mechanism of BCF manoeuvring. The second scenario considers the heading control and, therefore, the scaling of body curvature by calculating the control variable c_s. 2D waypoint tracking control is achieved by defining the control error $e(t)$ as the difference between the current heading angle ψ and the desired heading angle ψ_{wp}, expressed as

$$e(t) = \psi_{wp} - \psi(t). \tag{3.35}$$

In the case of the multi-body system, the desired angle towards the waypoint is calculated from the global coordinates of the local frames B_0 ($x_{\mathcal{F}_0}, y_{\mathcal{F}_0}$) and $B_1(x_{\mathcal{F}_1}, y_{\mathcal{F}_1})$ and the waypoint coordinates (x_{wp}, y_{wp}), expressed as

$$\psi_{wp}\,(\mathrm{t}) = \; atan\left(\frac{y_{\mathcal{F}_0}(\mathrm{t}) - y_{wp}}{x_{\mathcal{F}_0}(\mathrm{t}) - x_{wp}}\right), \tag{3.36}$$

and the heading of the fish $\theta(t)$ is calculated by

$$\psi(\mathrm{t}) = \; atan\left(\frac{y_{\mathcal{F}_1}(\mathrm{t}) - y_{\mathcal{F}_0}(t)}{x_{\mathcal{F}_1}(\mathrm{t}) - x_{\mathcal{F}_0}(t)}\right). \tag{3.37}$$

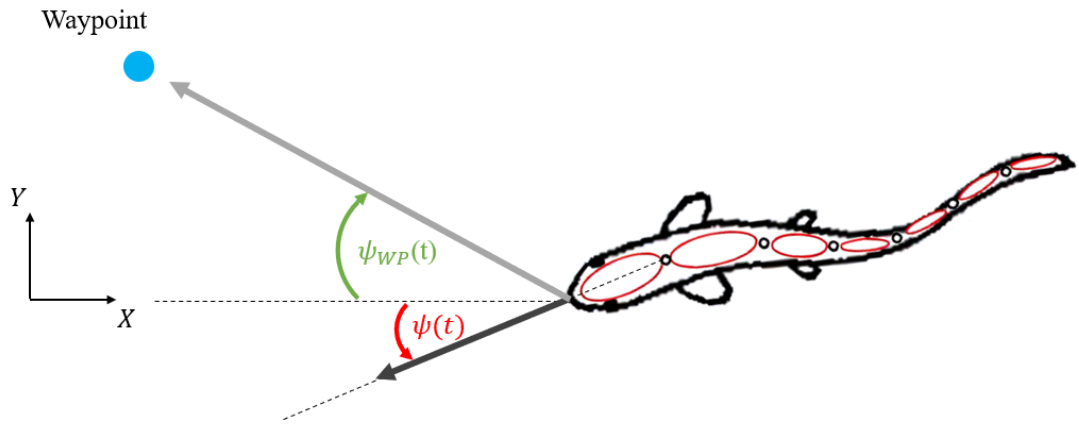

Figure 3.17 Schematic of waypoint tracking manoeuvring control.

3.3.2.3 Scenario 3: waypoint station holding within fluid stream

Scenario 3 considers approaching and station holding at a defined target position located in front of the swimmer facing incoming flow. It is possible to achieve two combined control targets of swimming towards and holding station at a target position by defining a single control error and calculating the amplitude scaling variable c_a.

Firstly, the control, similar to Scenario 1, is defined as the difference between the swimming velocity and a target velocity

$$e(t, x_{td}(t)) = u_{set}(x_{td}(t)) - u(t). \tag{3.38}$$

Further, the target velocity is defined dynamically based on the swimmer's distance to the target position, so that

$$u_{set}(x_{td}(t)) = -\frac{x_{td}\ (t)}{T_{set}}, \tag{3.39}$$

where $x_{td}(t) = x_{target} - x(t)$ defines the distance between the swimmer's position and the target position, while T_{set} denotes a time constant that makes it possible to tune the magnitude of u_{set}.

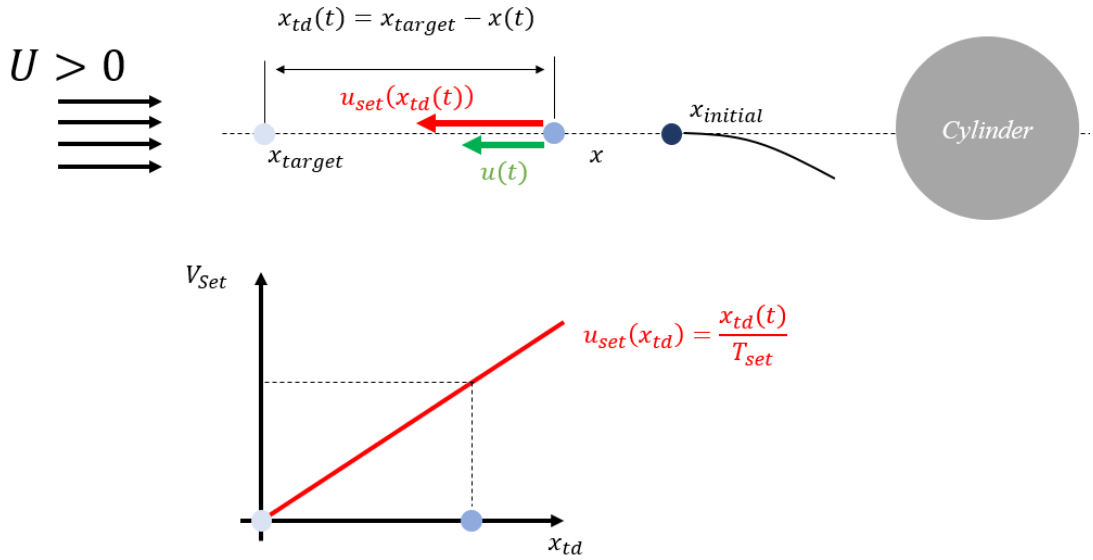

Figure 3.18 Schematic of swimming control to approach and hold a target position within incoming flow.

Figure 3.18 depicts the control error logic in which the target velocity of the swimmer is coupled to its relative position to the target. Starting from the initial position, the control error is reduced by the swimmer approaching the target position. By definition of the control error, the reference velocity reduces as the swimmer approaches the target, leading to a high acceleration at the start and a low velocity approach towards the target position. At the target position the swimmer achieves force equilibrium, in other words, it is balancing the drag of the incoming flow and the thrust generated from the pitching motion.

3.4 Conclusion on numerical modelling and control of BCF swimmer

To accurately model and predict the dynamics and fluid structure interaction of bio-inspired underwater robots or fish is a complex and challenging task. This work chooses to apply a numerical methodology because of its high detail, accuracy and information density to allow for detailed flow and control analysis.

This chapter starts with a general introduction of Computational Fluid Dynamics and the fluid governing equations. Next, key aspects important to the numerical

investigations in Section 4 are introduced, such as mesh generation and mesh quality as well as solver schemes and User Defined Function structure and coupling.

A single and multi-body algorithm to model the internal and external dynamics of an underwater swimmer are introduced in detail and reference is given to a CFD-FSI model.

A key novelty of this work is the integration of a control algorithm within CFD simulations to enable the modelling of unsteady swimming scenarios. Section 3.3.2 provides a general introduction to linear feedback control and its application in the control of Body Caudal Fin fish. Three control strategies for different swimming scenarios are derived by definition of the feedback control error.

Chapter 4 Numerical investigations

In the following, the control strategies derived in Section 3.3.2 are applied in three different investigations. Work presented in Sections 4.1, 4.2 and 4.3 have been published in (Wright et al., 2023b), (Wright et al., 2020b) and (Luo et al., 2021) respectively.

4.1 Velocity and heading feedback control for a combined hydrodynamic and control study of optimal BCF manoeuvring.

4.1.1 Problem description

A BCF swimmer accelerates against surrounding fluid in a periodic motion by means of lateral undulation. Straight swimming or cruising is achieved through lateral force symmetry over one undulation cycle. By curving the body asymmetrically, the force imbalance results in a turning moment acting on the swimmer. BCF swimmers move their anterior body (head) and posterior body (peduncle and caudal fin) independently during turning manoeuvres (Weihs, 1972). The turning moment may be a combination of a posterior reactive force on the tail fin, an anterior lift force as well as a reduced drag force by aligning towards the new swimming direction.

The curving of the central body line is a key mechanism of moment change in BCF manoeuvring (Gray, 1933). To understand BCF swimmer manoeuvring, the turning performance of BCF locomotion is investigated with different curvature envelopes. Here, a curvature envelope describes the curvature distribution along the central line. To investigate the self-propelled turning performance at different Reynolds numbers and curvature envelopes, the scenario in Figure 4.1 is selected. Two linear feedback controllers are used to reach the required speed and maintain straight-line swimming until the prescribed curvature is applied. From rest, the swimmer accelerates by means of undulation motion to reach a predetermined swimming speed corresponding to a desired Reynolds number. When this forward velocity is reached, the body curves following a prescribed curvature envelope. The investigation does not consider any behavioural factors and assumes that all body motions are focused on benefiting turning performance.

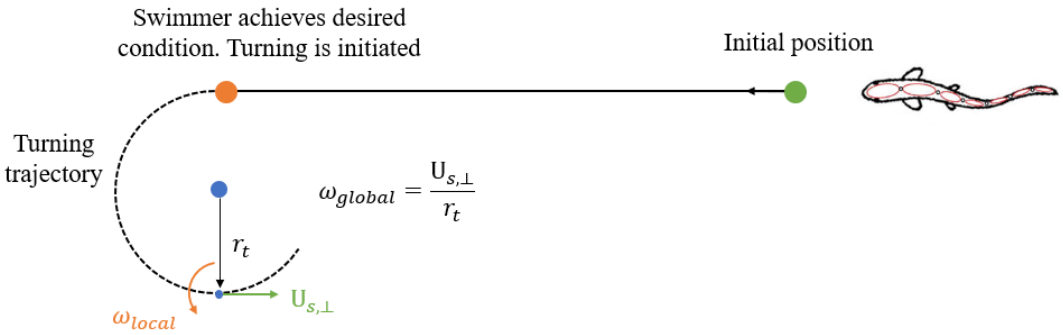

Figure 4.1 Simulation setup for swimmer to accelerate to achieve a desired condition (defined horizontal velocity) before initiating a prescribed turning manoeuvre. (Wright et al., 2023b).

In this work a coupled CFD multi-body simulation environment (Hu, 2016;Li et al., 2018) has been applied. The commercial CFD software package Ansys Fluent 22.1 is coupled with a multi-body dynamics algorithm utilising an in-house developed UDF. This method solves the internal and external dynamics of a multi-body system in a CFD environment at each time step through three recursions and one numerical integration. A linear feedback control algorithm completes the simulation setup. A detailed description of the CFD tool and validation results are given in Section 3.2.4 and in literature (Hu, 2016;Li et al., 2018).

A simplified fish geometry is considered as a multi-body system in the shape of a 2D NACA0012 foil comprising body segments connected via actuated links along the central line that resemble muscle actuation. The NACA0012 geometry is separated into 10 equal cord length body segments with 9 joints in between.

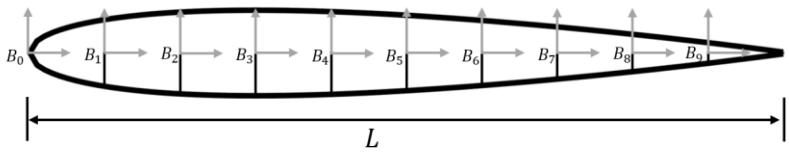

Figure 4.2 Simplified fish geometry modelled as a 2D NACA0012. (Wright et al., 2023b).

The local coordinate system B_0 is the starting point of the recursive loop. The undulation of the body is achieved through rotational motions around the joints (including a sinusoidal motion for undulation and an offset to curve the body with respect to the central line) shown in Figure 4.2. The length of the individual segments l_i is evenly distributed and fixed, resulting in a central line length of $L = 0.1\ m$.

The rotational motion of a segment around its front linkage at location s is given by Equation (3.30). The amplitude envelope $A(s)$ and wavelength $\varphi(s)$ are defined by

$$A(s) = c_1 \frac{\left({}^{s}/_{L} + c_2\right)}{c_3}, \tag{4.1}$$

$$\varphi(s) = 2\pi \frac{s}{L}, \tag{4.2}$$

with c_1, c_2, c_3 being kinematic coefficients. The offset term $C(s)$ is introduced to achieve the turning manoeuvre. The present study includes two curvature envelopes. Firstly, a constant curvature envelope (equal offset at all joints) is described by

$$C(s) = 0.15\ \mathrm{c}_4, \tag{4.3}$$

where c_4 is a magnitude coefficient. Secondly, a linear curvature envelope from the leading to the trailing edge is described by

$$C(s) = 0.15\, c_5 \frac{s}{L} + c_6, \tag{4.4}$$

where coefficients c_5 and c_6 define the slope and offset of the linear envelope. The total curvature of the swimmer is defined as the sum of the time independent joint displacement $\bar{r}$ of all joints $C(s)$ over the swimmer length

$$\kappa = \sum_{i=0}^{9} \bar{r}\ /l_i. \tag{4.5}$$

Table 4-1 and Table 4-2 summarise the total curvature and coefficient values used in an investigation into curvature magnitude and comparison of envelopes respectively. The coefficients c_5 and c_6 are chosen for linearly increasing and decreasing envelopes to observe performance differences of predominant head or tail curvings.

Table 4-1 Summary of coefficients used in a constant envelope.

Total curvature κ [rad/m]	2.7	5.4	8.1	10.8	4.6
c_4	0.2	0.4	0.6	0.8	1.0

Table 4-2 Summary of coefficients used in constant and linear curvature envelopes with the total curvature remaining constant.

Total curvature κ [rad/m]	Constant envelope [-]	Head turning envelope (lin_d) [-]		Tail turning envelope (lin_u) [-]	
8.1	$c_4 = 0.6$	$c_5 = -1$	$c_6 = 1.1$	$c_5 = 1$	$c_6 = 0.1$

In this study a modified Cost of Travel function for turning is proposed. This is denoted as Cost of Manoeuvring (CoM) and is defined as the ratio of undulation cycle-averaged input power $\overline{P_{in}}$ to the global angular velocity

$$CoM\ = \frac{\overline{P_{in}}}{\omega_{\text{global}}} = \frac{\overline{P_{in}}}{\frac{U_{s,\perp}}{r_t}}. \tag{4.7}$$

The average input power is calculated as the sum of all joints' cycle-averaged power (defined as the product of cycle-averaged torque and angular velocity):

$$\overline{P_{in}} = \sum_{j=1}^{9} \overline{\tau_j} \cdot \overline{\dot{r}_j}. \tag{4.8}$$

The turning radius is calculated within a MATLAB function developed by Mjaavatten (2021). To filter out the curvature of the instantaneous undulation trajectory, the curvature is calculated using points of the cycle-averaged trajectory sampled at an interval of one undulation cycle period *T*.

4.1.2 Simulation setup

As shown in Figure 4.3, the size of the computational domain is $25L$ by $8L$, in which the leading edge of the swimmer is originally located at a point $5L$ by $4L$ from the bottom right corner. Here, $L = 0.1\ m$ is the fish body length. The unstructured CFD

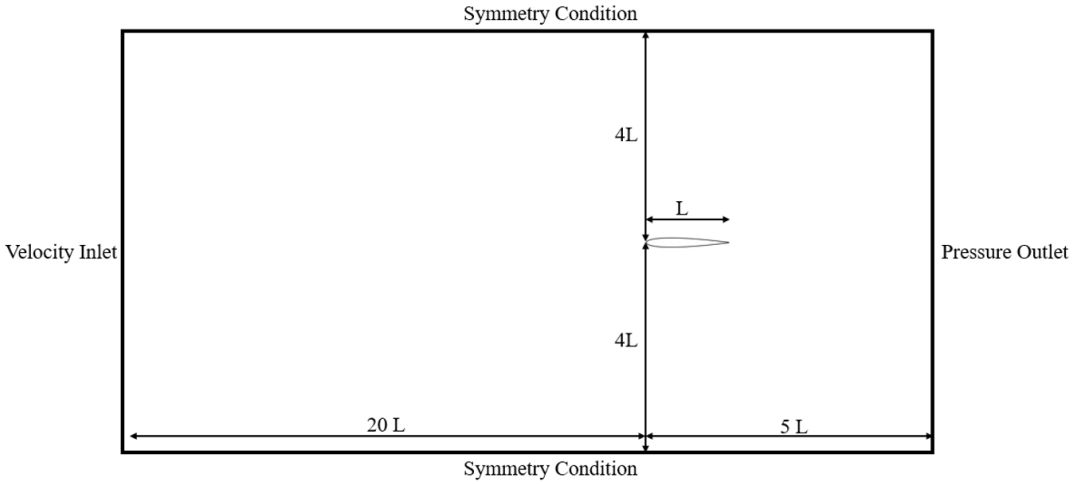

Figure 4.3 CFD computational domain setup and boundary conditions. (Wright et al., 2023b).

mesh sizing is $\Delta_{xy} = \frac{10}{3333} L$ at the swimmer boundary and increases to $\Delta_{xy} = \frac{10}{33} L$ in the far field. The time step is set to $\Delta t_s = T/250$, where T is the undulating period. Coefficients of the amplitude envelope are chosen to follow an anguilliform pattern described in (Kern and Koumoutsakos, 2006) with coefficients $c_1 = 0.125, c_2 = 0.0315, c_3 = 1.03125$. Initial control coefficients are chosen as $c_a(t_s = 0) = 0$, $c_a(t_s = 1) = 0.1$ and $c_s = 0.0$ for $t_s < 2T$. The maximum offset value is set as $c_{s,max} = 0.2$. The velocity inlet condition is set to zero so that the swimmer starts in still water.

This study applies a velocity controller as described in Section 3.3.2.1, and $\boldsymbol{u}_{set}$ is defined based on the desired Reynolds numbers to be $\boldsymbol{u}_{set}$= 0.02, 0.015 and 0.01 m/s for Re = 2000, 1500 and 1000 respectively. The second PID controller adjusted the curvature magnitude by calculating the control coefficient c_S based on the error between the current and desired heading angle. The control action is limited to $-0.2 \leq c_s \leq 0.2$. Both speed and steering controllers are tuned to achieve a damped response, in other words, control gains (K_P, K_I, K_D) are chosen by trial and error to achieve a fast-converging system response without significant overshoot. Initial control gains are found in Maertens et al. (2017). The tuned control gains implemented for speed and steering respectively are as follows: $K_P = 5\,, K_I = 5, K_D = 55$ and $K_P = 0.03, K_I = 0, K_D = 0.1$.

4.1.3 Results and discussions

4.1.3.1 Effect of added body curvature and quasi-steady turning state

Undulatory swimming shows a characteristic periodicity stemming from vortex shedding during the peaks and troughs of the body motion. Straight-line swimming at a constant cycle-averaged speed is described as the quasi-steady state at which body forces are in balance over one undulation cycle. To initiate turning, force symmetry is broken by curving the body's central line. Changes in the position of the centre of mass, moment of inertia and resulting biased cycle-averaged loads lead to a net moment and subsequent angular acceleration. Figure 4.4 plots the yaw moment of an accelerating and turning swimmer according to the setup in Figure 4.1 for Re=2000 and a constant curvature. Three distinct periods are visible, in other words, a transition period from a static state to a quasi-steady state (t=0 to 25 seconds), a transition period during which the central line curves into an equally distributed curvature of κ=8.1 rad/m at (t= 25 to 27 seconds) and, finally, a period of quasi-steady turning state (t = 27 to 35 seconds).

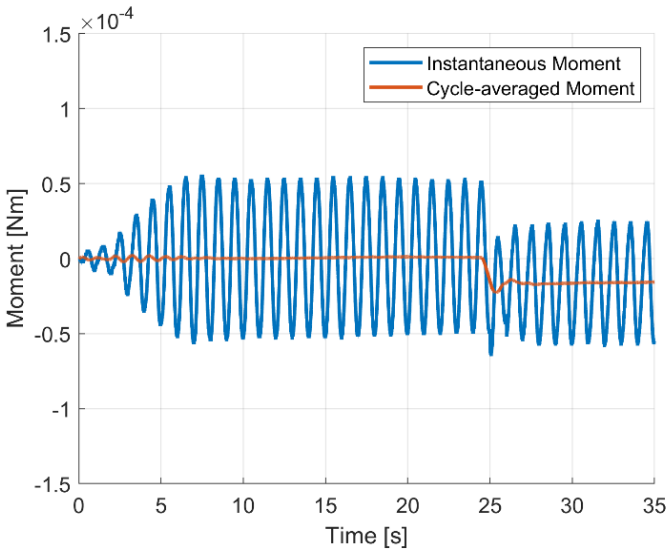

Figure 4.4 Instantaneous moment and cycle-averaged moment showing the three transition states. Re=2000. (Wright et al., 2023b).

The vorticity contour of each period is shown in Figure 4.5. Beginning at the quasi-steady state, the reverse Karman vortex street remains horizontal and periodically symmetric. During the transition stage the body curves and changes the heading direction. Meanwhile, vortices are shed at a non-zero angle. In the third stage, the re-oriented swimmer continues undulation around the curved central line and reaches the quasi-steady turning state. It is found that the time-averaged angular velocity appears to be zero during straight swimming ($t < 25$ s). After that the swimmer maintains a time-averaged angular velocity of 0.2 rad/s. Interestingly, for the selected parameters turning has only a negligible effect on the heading directed velocity, in other words, despite the change in heading direction the swimmer maintains a close to constant speed in the heading direction.

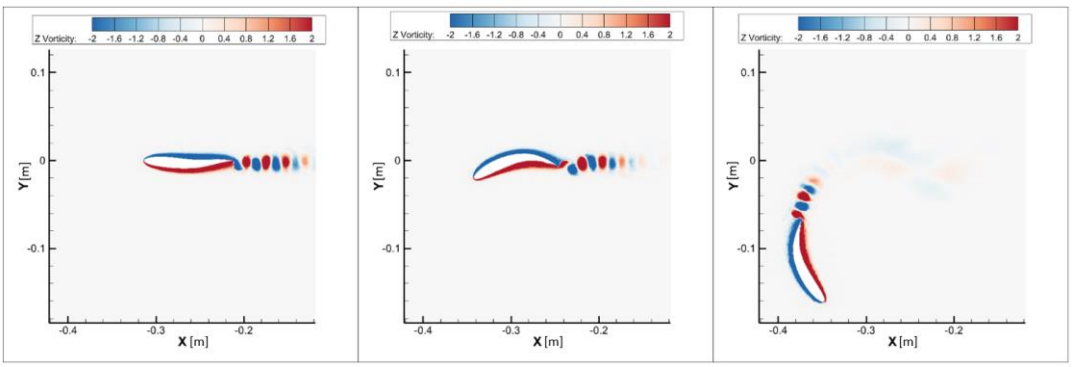

Figure 4.5 Vorticity contour of the constant envelope; left: quasi-steady state at t=25s, middle: transition state at t=26.4s and right: quasi-steady turning state at t=34.4s. Re=2000. (Wright et al., 2023b).

The input power to fulfil the undulation motion reflects the effort of the swimmer to accelerate against the surrounding fluid. As shown in Figure 4.6 during the initial acceleration, the longitudinal force peak coincides with an input power peak at around t=7 seconds. Here, the longitudinal force and power peak also correspond to the acceleration peak. From there onwards, the swimmer continues to accelerate to the targeted velocity but at a decreasing rate. At the quasi-steady turning state at approximately t=27 seconds, the cycle-averaged power converges to a stable value close to zero. The power expenditure during quasi-steady state straight-line swimming and turning are close to each other, which suggests that the extra effort required for turning after it is initiated is insignificant.

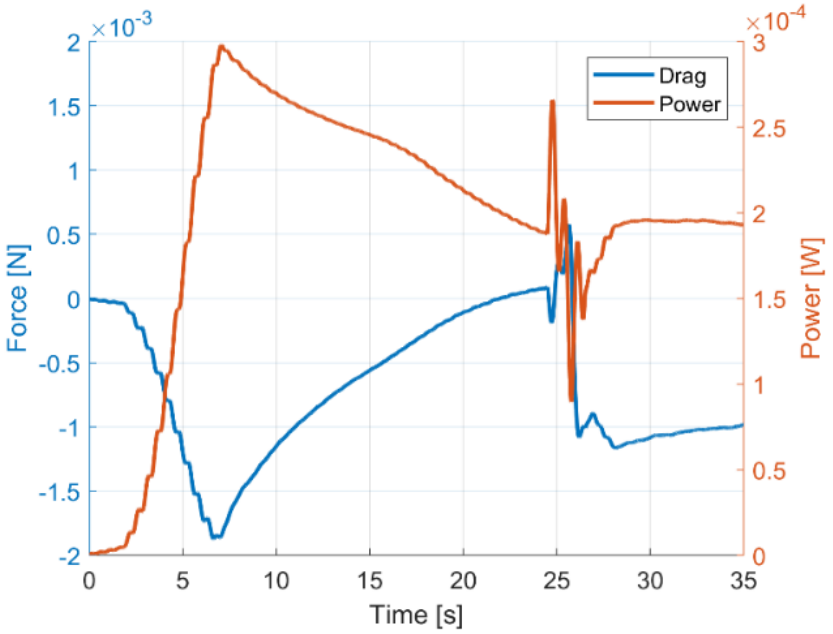

Figure 4.6 Cycle-averaged drag force and power expenditure for a constant envelope. Re=2000. (Wright et al., 2023b).

Observations of the above three states are consistent across different curvature magnitudes and investigated Reynolds numbers (Re = 1000, 1500 and 2000). A linear increase in magnitude of the constant curvature envelope results in a close to linear increase in power expenditure. The resulting turning angle decreases with increased curvature yet flattens out at the end, as shown in Figure 4.7. This results in a decreasing CoM for increased curvature. A similar pattern is observed for all Reynolds numbers where the radius is the dominant variable in the CoM calculation due to its reduction at an increased curvature.

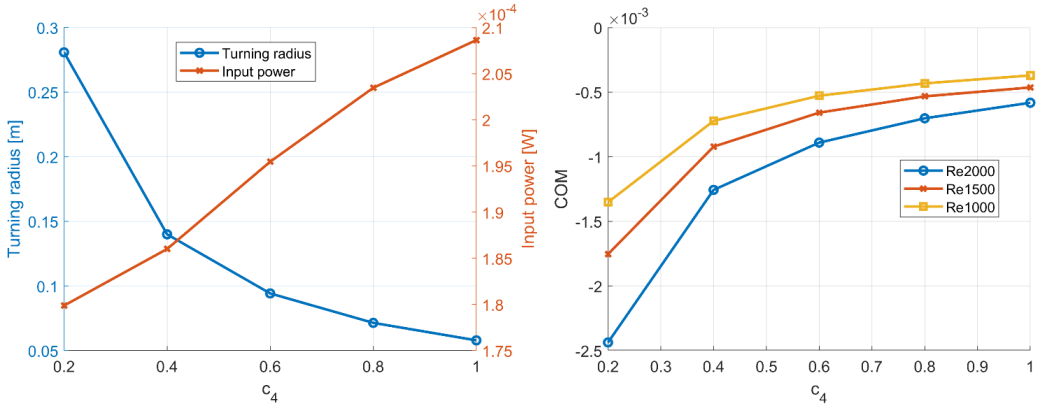

(a) (b)

Figure 4.7 (a) Turning radius and power input for an increasing curvature at Re=2000 (b) Cost of Manoeuvring for increasing curvature. Re=1000, 1500 and 2000. (Wright et al., 2023b).

4.1.3.2 Comparison of curvature envelopes

Fish turn both their head and bend their tail in a turning manoeuvre (Weihs, 1972). In the following, the contribution of head and tail movement towards turning by comparing three curvature envelopes with the same total curvature is investigated. The three selected envelopes are: a constant envelope (equal offset across all joints), a linearly increasing envelope denoted as lin_u (predominantly tail curved) and a linearly decreasing envelope denoted as lin_d (predominantly head curved). The kinematic parameters of these cases are shown in Table 4-2. The Reynolds number in this part of the investigation is fixed at 2000.

Shown in Figure 4.8, the cycle-averaged drag shows two distinguishable phases during the turning transition period. These are highlighted as Phase I and Phase II. Following general observations, negative drag forces correspond to swimming velocity acceleration, and positive drag forces correspond to swimming velocity deceleration in the heading direction. Therefore, Phase I may be associated with the initial body curving against the longitudinal moving flow, leading to an increase in drag forces and subsequently to deceleration. Likewise, Phase II may be associated with the first full sweep with a curved centre line, increasing the thrust and thus acceleration.

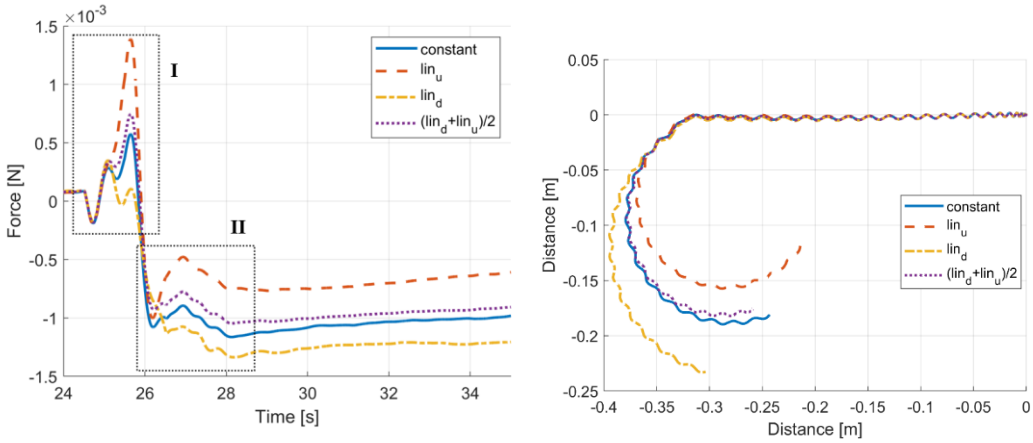

(a) (b)

Figure 4.8 (a) Time histories of the drag force with different curvature envelopes. (b) Trajectories of a constant envelope, linear envelopes and averaged linear envelopes. (Wright et al., 2023b).

When comparing the constant envelope with the average of both linear envelopes, the curves show close agreement (see Figure 4.8). This leads to the conclusion that the constant envelope can be segregated into head and tail contributions. According to Figure 4.8 (b), the predominantly tail turning envelope achieves a sharper turn with a smaller turning radius. This, together with the close match between the constant envelope and averaged linear envelopes, suggests that the head turning has a negative effect on the turning performance.

A comparison of the heading angle and the passing fluid velocity angle may provide an explanation. As shown in Figure 4.9 in the predominantly tail curving envelope the heading angle leads the fluid angle (that is the relative angle of attack of the flow). In contrast, for the predominantly head curving envelope, after an initial peak, the heading angle is behind the fluid angle. For the constant envelope, the two angles are closely aligned, with the heading angle slightly leading the fluid velocity angle.

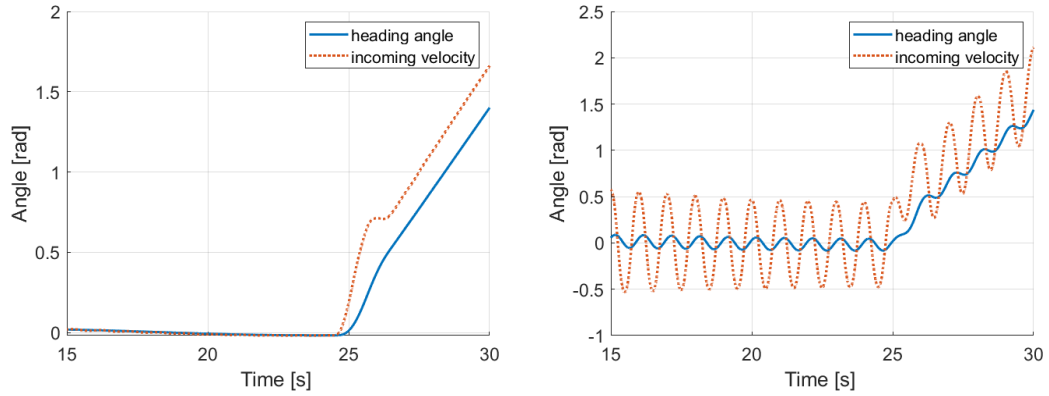

(a)

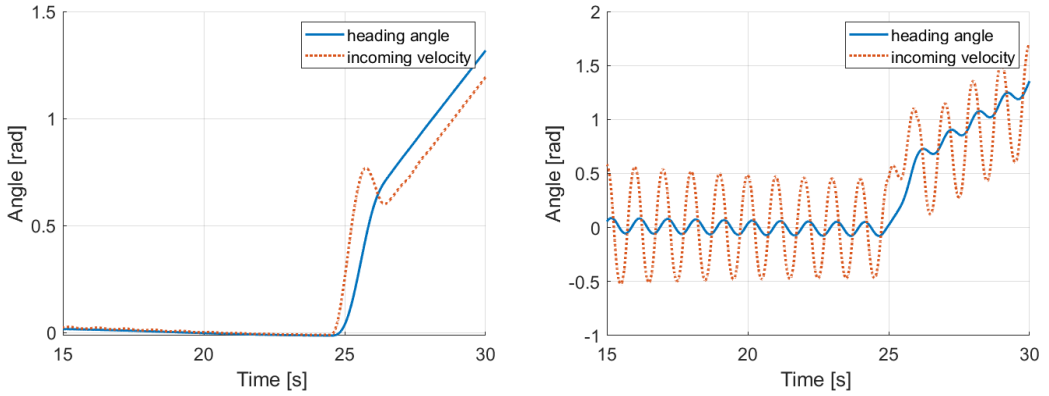

(b)

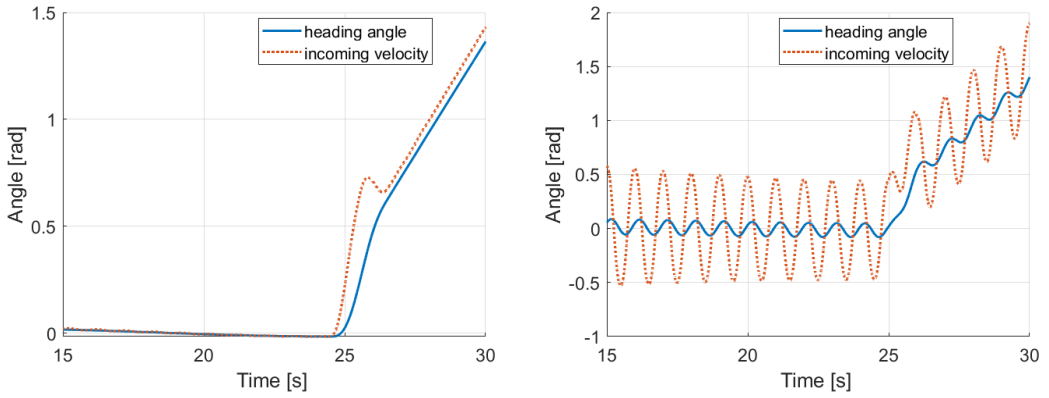

(c)

Figure 4.9 Instantaneous and cycle-averaged heading and incoming flow velocity angles for (a) tail turning (b) head turning (c) constant envelope. (Wright et al., 2023b).

A leading heading angle may positively influence turning performance in that it provides additional moment for the rotation and reduces the counter rotation moment. Figure 4.10 highlights the described mechanism. A strong tail sweep may provide sufficient moment and energy to turn the swimmer in front of the passing fluid stream, providing additional pressure force to create a moment in the turning direction.

Meanwhile, as the tail now sweeps in the opposite direction, the fluid force on the head may provide a dampening effect that reduces the counter turning moment. Evidence of this can be seen in the reduced counter turning moment amplitude between the head and tail curving curves in Figure 4.11. On the other hand, a curved head may negatively influence turning performance in that it does not create sufficient moment to turn the swimmer in front of the fluid stream. Additionally, the reactive force acting on the fish during curving of the head leads to a counter turning moment, and as a result, reduces the positive turning effect of the tail curvature. Further, a curved head may provide less resistance during counter turning undulation.

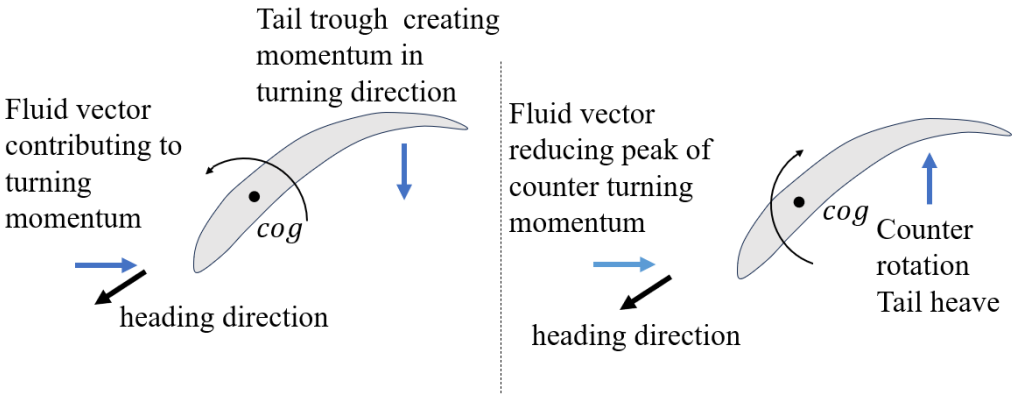

Figure 4.10 Schematic showing heading angle effect on moment during undulation amplitudes. (Wright et al., 2023b).

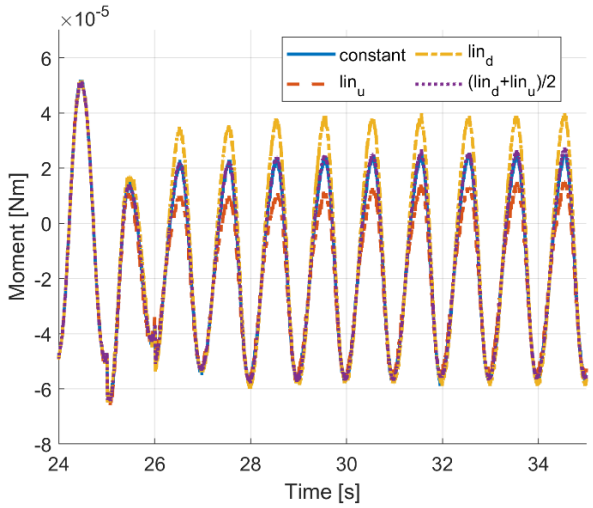

Figure 4.11 Time histories of the moments with a constant envelope, linear envelopes and averaged linear envelopes. (Wright et al., 2023b).

The negative contribution of head turning on the turning performance is also visible in the cycle-averaged power curve in Figure 4.12.

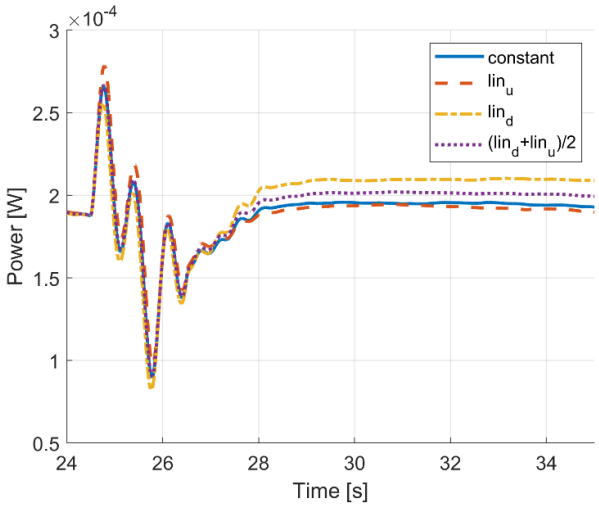

Figure 4.12 Time histories of the cycle-averaged power of a constant envelope, linear envelopes and averaged linear envelopes. (Wright et al., 2023b).

4.1.4 Conclusion on velocity and heading feedback control for combined hydrodynamic and control study of optimal BCF manoeuvring

High manoeuvrability is one of the main desired improvements of a bio-inspired design. Multi-actuated body flexibility enables agile and efficient direction change to adapt and operate in complex environments. After identifying a gap in the knowledge of unsteady manoeuvring and optimal turning of BCF swimmers, a numerical study is conducted with the focus on the unsteady swimming performance of a BCF swimmer during turning. A controllable, self-propelled simulation of a BCF swimmer that performs a turning manoeuvre at an intended forward velocity and different body curvature envelopes is created by adding a linear feedback control algorithm to a CFD multi-body tool. By modelling the simplified fish geometry as a multi-body system, information is gained of joint torque resembling a bio-inspired robotic system so that it is possible to find measures to improve the controllability and turning performance.

Results show the swimmer reaching a quasi-steady turning state similar to the quasi-steady state during rectilinear swimming. The swimmer switches from a rectilinear trajectory to a curved trajectory of stable, periodically repeating state of turning through a transition stage, during which body curvature is added. For a constant envelope, it is shown that the turning radius is related to the magnitude of body

curvature. With increased curvature, the power expenditure increases linearly, while the turning radius decreases but eventually flattens out.

To identify the contributions of head and tail curvatures on the turning performance, predominantly head curved, predominantly tail curved and constantly distributed curvature envelopes are compared. The investigation revealed a symmetry between the head-dominated and tail-dominated envelopes so that the averaged results show close agreement with the constant envelope in terms of force and trajectory. This leads to the conclusion of distinguishable contributions of head and tail curvature on the performance. Further, simulation results show the overall superior turning performance of the predominantly tail curved envelope, highlighting the negative effect of head turning. This leads to finding control parameters that enable smaller turning radii at lower power expenditure. Unlike most of the existing research, the present study considers a more biologically realistic scenario by considering a variable body curvature. Therefore, the findings may be useful for the design of bio-inspired underwater robots with regards to manoeuvrability and stability purposes.

This work proposes a new quantitative measure of turning performance, the Cost of Manoeuvring. The CoM provides a combined assessment of power, turning radius and speed. Simulations show that the CoM is improved in larger body curvature, with a reduced radius as the dominant factor. While the power increases linearly, the radius decreases linearly before it flattens out. Among the three curvature envelopes that are examined, the predominantly tail curving envelope achieves the smallest turning radius and best power performance and, as a consequence, the best CoM.

4.2 Feedback controlled pitching amplitude for assessment of thrust performance of a flexible plate

4.2.1 Problem description

Fish following BCF locomotion propel by accelerating the surrounding fluid in the opposite wave direction. This fluid is accelerating due to the pressure differences along the deforming body in addition to reactive forces at the trailing edge of the swimmer as a component of vortex shedding. The body deformation of a robotic swimmer is

induced by active motor control, which can be optimised to increase efficiency. In search of higher thrust efficiency, observations of natural swimmers suggest including a passive deforming body section at the tail in the form of a flexible caudal fin. The deformation of the fin is influenced by the forced motion at the leading edge together with the shape and rigidity of the fin interacting with the surrounding fluid domain.

The simulation applies the CFD FSI methodology introduced in section 3.3.

The analysis compares a matrix of the frequency and stiffness parameters as shown in Table 4-3, to gain insight into the hydrodynamic performance of different material rigidities as well as how they operate at different frequencies. The testing matrix consists of three materials, each simulated at five frequencies. Both changes in frequency and rigidity of the plate will lead to a different response.

4.2.2 Simulation setup

All cases share the same simulation setup, except for variations to the actuation frequency and plate rigidity. The mesh domain, measuring 0.8 m in height by 2.1 m in width, has the fin positioned horizontally with the leading-edge positioned at vertical centre and 0.5m from the left boundary, as depicted in Figure 4.13 (a). The left and right boundaries are assigned with corresponding inlet and outlet conditions. Both horizontal boundaries are assigned a far-field condition. The generated mesh contains 57424 cells and the minimum grid spacing is $1.67 \times 10^{-3}\, L$. Refinement is set towards the fin boundary to ensure correct calculation and capture of all physical effects, as depicted in Figure 4.13 (b). A mesh independency study is published in (Luo et al., 2020). The time step for each case is $t_s = T/100$.

The simulated geometry cross-section is inspired by the experimental investigation conducted by Paraz et al. (2014). To match the experimental setup, the chosen Reynolds number 6000 is equal for all cases but is assumed to be of laminar flow; the mass ratio is $m^* = 0.04$.

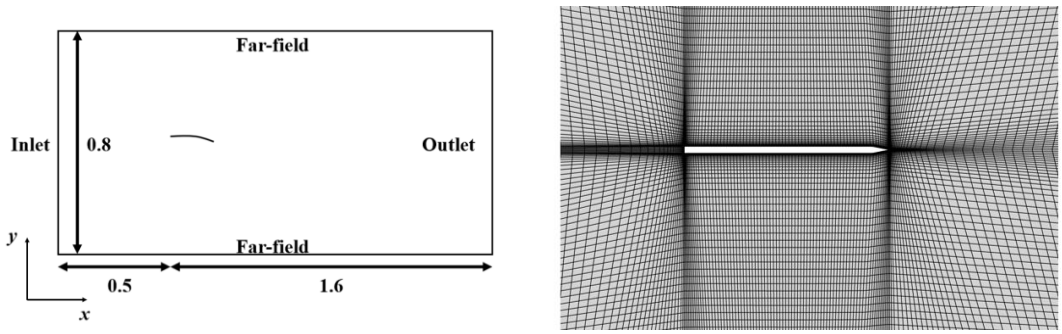

(a) (b)

Figure 4.13 (a) Domain setup and (b) mesh refinement. (Wright et al., 2020b).

For this investigation, the rigidity of the material is of uniform distribution, which reflects the targeted accessible adaptive manufacturing method. Three materials characterised by dimensionless stiffness are considered, $K = 10$, $K = 1.04$ and $K = 0.25$. These correspond to a highly rigid material, a material of medium rigidity and a soft material. These will be called hard, medium and soft in the following.

Table 4-3 Overview of simulated cases varying nondimensional material stiffnesses and frequencies.

	$f^* = 0.75$	$f^* = 1$	$f^* = 1.5$	$f^* = 2$	$f^* = 2.5$
Hard $K = 10$	Case 1	Case 2	Case 3	Case 4	Case 5
Medium $K = 1.04$	Case 6	Case 7	Case 8	Case 9	Case 10
Soft $K = 0.25$	Case 11	Case 12	Case 13	Case 14	Case 15

For all, the Poisson's ratio is 0.35. For each material, the performance is assessed at 5 frequencies. Table 4-3 provides an overview of all simulated cases. When setting up the simulation, it is important to ensure the different cases are compared under comparable conditions. To achieve this, all simulated fins are targeted to reach quasi-steady state, in other words, generate thrust force to balance the drag force at a constant incoming velocity. Due to the characteristics of each case, the thrust generation varies; hence, a desired pitch amplitude to achieve a quasi-steady state must be obtained. This is achieved by implementing feedback control of pitch amplitude to balance the cycle-averaged drag and thrust and, as a consequence, the average force component in the velocity direction converges to zero.

The sampling time is equal to the CFD time step. The tracking error is the difference between the fed back time-averaged thrust coefficient and the setpoint of zero as described in Section 3.3.2.1. The tuned control gains for a properly damped system response are found to be: $K_P = 5$, $K_I = 0$ and $K_D = 0.2$. To examine the tracking performance of the controller, a tuning case summary is presented. Here, the controller gains are tuned manually according to the Ziegler-Nichols method. The PID controller gains have been found within 7 simulations.

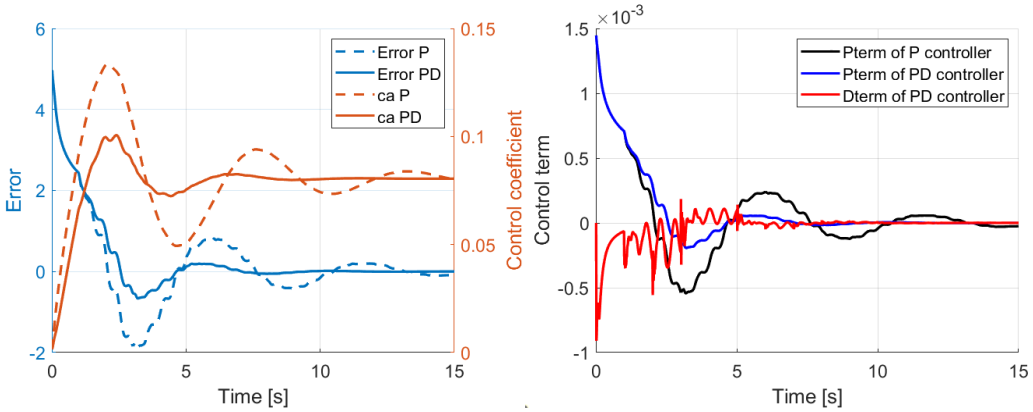

(a) (b)

Figure 4.14 (a) Progression of error and controller output for P and PD controllers and (b) P and PD term progression. (Wright et al., 2020b).

For the initial P controller, the output response c_a is stable yet overshoots with asymptotic convergence after around 15 oscillation periods. By adding a derivative error gain the overshoot is damped and faster convergence is achieved after circa 700 sampling periods. Figure 4.14 (b) shows the dampening effect of the derivative term reducing the overshoot of the P gain and achieving faster overall convergence. No steady-state error is observed; hence, there is no requirement to include an integral control.

4.2.3 Results and discussion

Changes to the rigidity of the fin lead to differences in vertical displacement along the fin when excited at the same frequency. Figure 4.15 (b) shows a trend of lower converged trailing edge displacement for higher actuation frequencies across all rigidities. It can be seen that at the same frequency, the more flexible the fin is, the larger the observed displacement. With increasing rigidity, the observed trailing edge

(TE) deflection amplitude changes little as the frequency is varied. With lower rigidity, the TE amplitude is more sensitive to frequency variation. However, for higher frequencies, the difference in TE amplitude between materials reduces to a minimum as seen in Figure 4.15 (b). An analysis of the converged pitch angle for the medium rigid fin shows a trend towards higher pitch amplitudes for higher frequencies, while results for the soft fin (K=0.25) show that the pitch amplitude reduces after an initial upward incline, see Figure 4.15 (c).

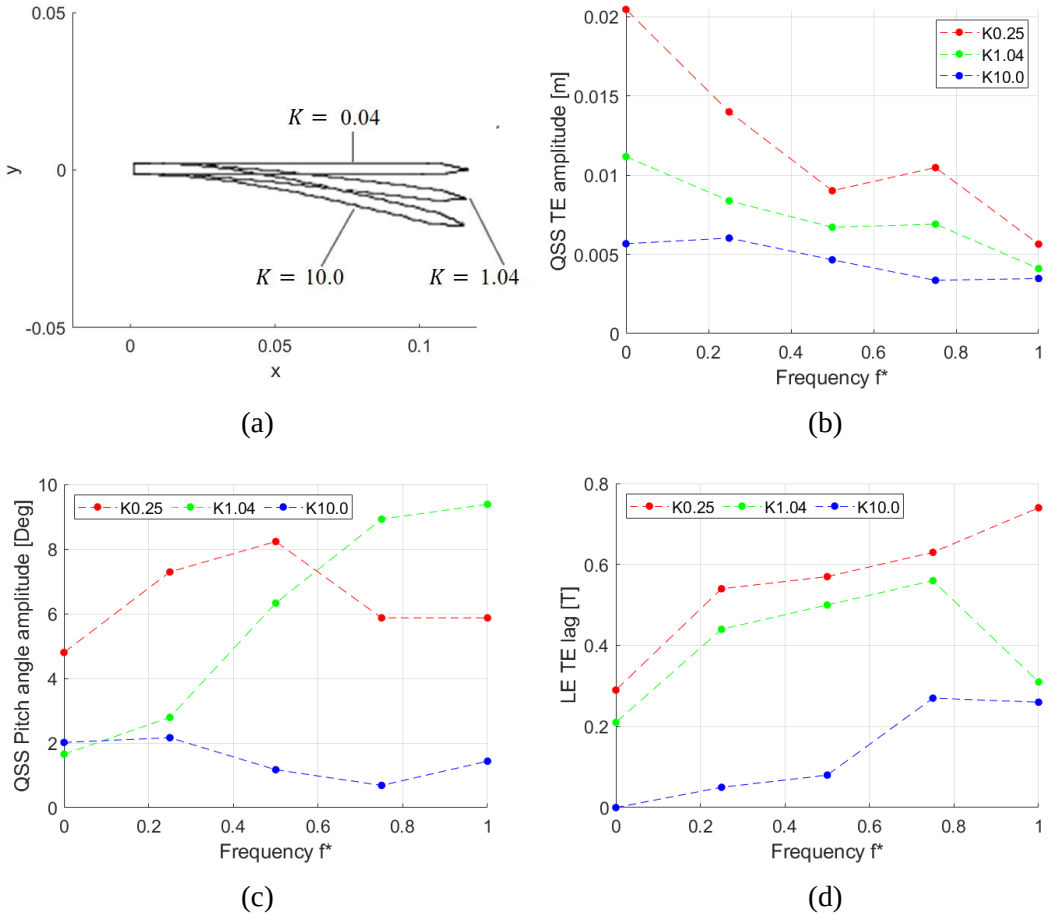

Figure 4.15 (a) Maximum structure displacement at f^*=0.75, (b) TE amplitude, (c) QSS pitch angle amplitude (d) lag of TE behind pitch. (Wright et al., 2020b).

Figure 4.15 (d) suggests that for increased pitch frequencies, the fin shape extends to show larger wave fractions. A more flexible structure leads to a larger phase difference between LE and TE at the same frequency. In Figure 4.15 (c) for changing frequencies the least rigid (K=0.25) fin shows an increase and subsequent decline of converged pitch angle amplitude. In contrast, the medium (K=1.04) and hard (K=10) fins show an increasing and relatively constant quasi-steady state angle amplitude respectively.

The difference in converged pitching amplitudes may point to an energetic benefit of higher actuations frequencies of the least rigid fin.

Figure 4.16 (a) plots the instantaneous thrust coefficient at a quasi-steady state of the rigid material and at varying frequencies. The curves show an increase in thrust peak for increased frequency. The time profiles of the symmetric periodic sign change prove the effectiveness of the PD controller in balancing the unsteady drag and thrust to approach the desired quasi-steady state.

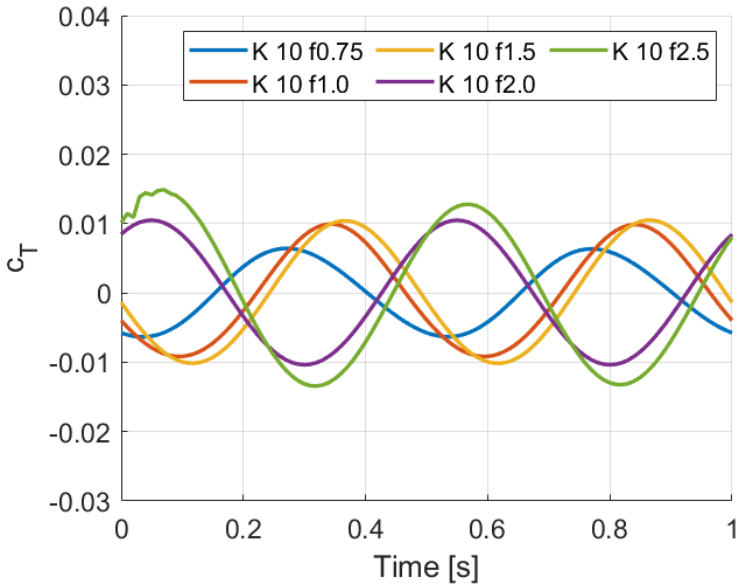

Figure 4.16 (a) Instantaneous thrust force of K=10 for all frequencies at quasi-steady state. (Wright et al., 2020b).

Figure 4.17 shows the Z-vorticity of all 15 cases at quasi-steady state recorded at the same T. The plots are organised so that cases of the same frequency are positioned in the same row. All fins show a trend towards smaller shed vortices for higher frequencies, which agrees with the reduced trailing edge amplitude in Figure 4.15 (b). Furthermore, the phase lag between LE and TE leads to a difference in the plotted vortex, seen, for example, when comparing contours 1), 2) and 3). The plotted contours also confirm the overall larger deflection of fins with lower rigidity. The plots depicted in Figure 4.18 assess two important prototype design criteria: controllability and power expenditure. For all cases, the same tuned control gains are used. Satisfactory convergence is observed for all cases. However, fast convergence is desirable for a swimming prototype which may be achieved by tuning the individual case further.

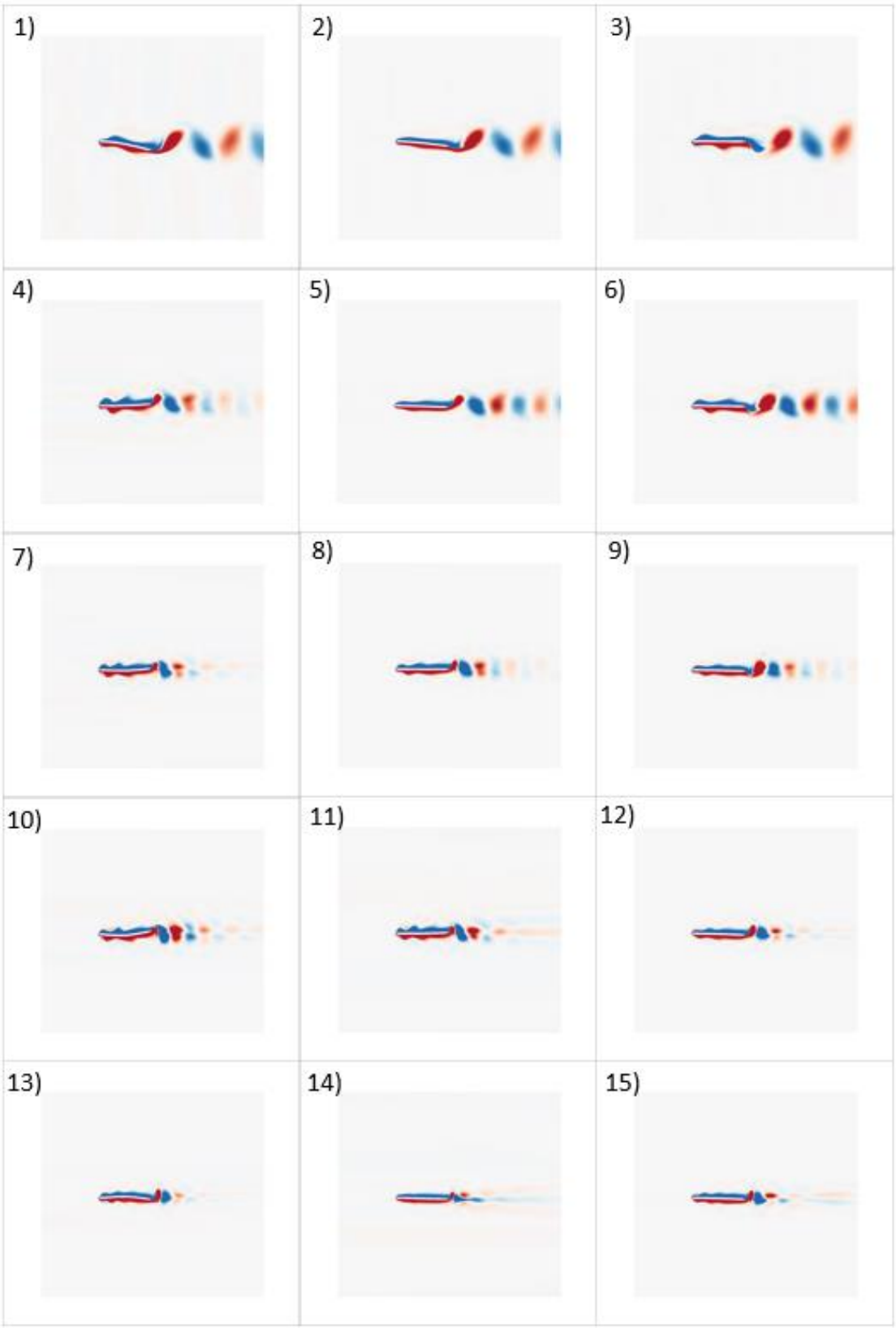

Figure 4.17 Z-vorticity contour at a constant pitch amplitude at instant T for all 15 cases. (Wright et al., 2020b).

Figure 4.18 (a) to (c) show the time progression of the controller output value c_a. Differences in control response (some showing overshoot and slower convergence) are due to the application of equal control gains across all cases to ensure comparability of the results. Improved response may easily be obtained by further tuning the individual setup.

The power coefficient shown in Figure 4.18 (d) generally follows the expectation that for higher frequencies the energy expenditure increases. While the power expenditure is similar for all materials at the first frequency, the medium stiffness (K=1.04) displays energy advantages for frequency cases 2, 3 and 5.

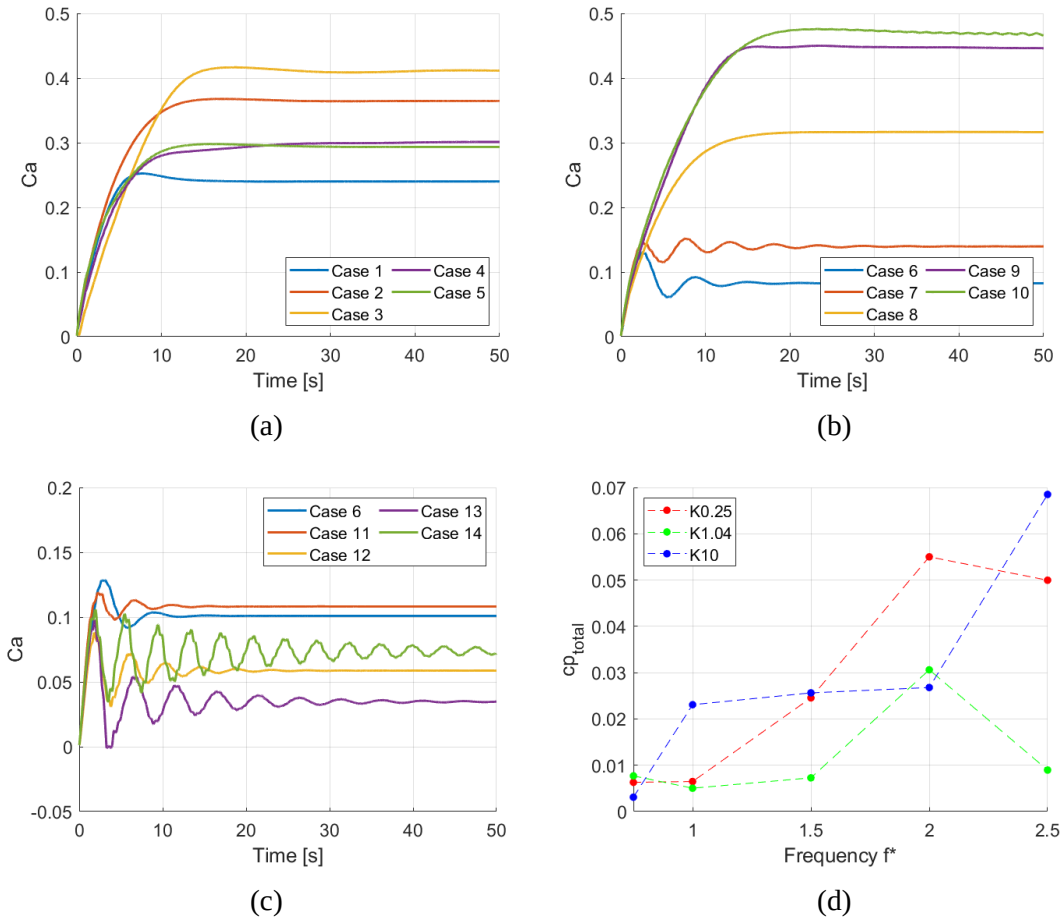

Figure 4.18 (a), (b), (c) progression of controller output variable and (d) power expenditure coefficient. (Wright et al., 2020b).

There is a significant drop in energy expenditure of the medium stiffness (K=1.04) from Case 4 to Case 5, although the pitch amplitude of the medium stiffness (K=1.04) at Case 5 is the highest of all cases (see Figure 4.18(c)). This may suggest improved

efficiency of this combination of medium rigidity ($K = 1.04$) and frequency ($f^* = 1$). Furthermore, the majority of lowest energy expenditures in conjunction with medium stiffness together with the good convergence over all frequencies suggests this is the optimal configuration of the three.

The resulting Strouhal number for all cases, related to the freely moving TE, are close to the assumed optimal range of 0.2 – 0.4 (Rohr and Fish, 2004).

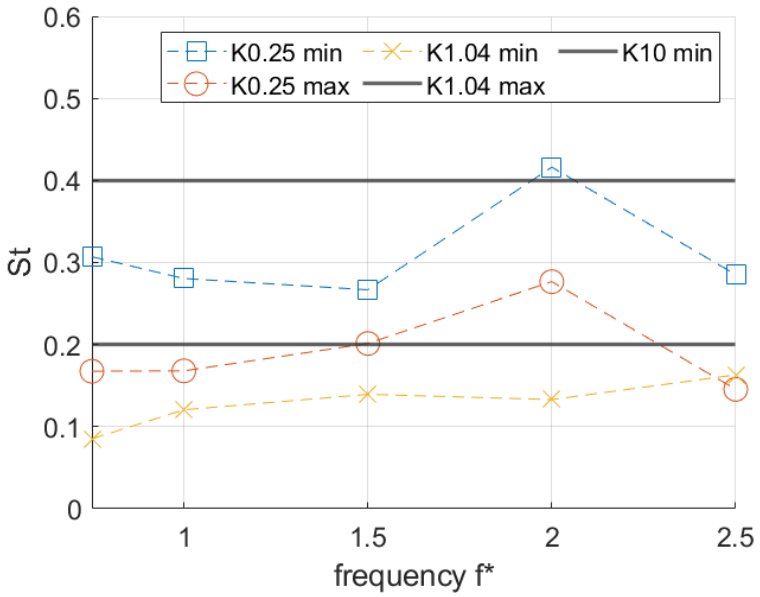

Figure 4.19 Strouhal number for all cases. (Wright et al., 2020b).

4.2.4 Conclusion on feedback-controlled pitching amplitude for assessment of thrust performance of flexible pitching plate

Fish utilise elastic appendages in support of efficient swimming. The mechanism of fluid acceleration and vortex shedding is found in many species to be supported by an elastic caudal fin. The presented numerical study in Section 4.2 aims to support the understanding of thrust generation and the influence of material elasticity actuated at different frequencies. The investigation assesses the thrust performance of an approximated 2D caudal fin geometry actuated in pitch within passing flow. The caudal fin's leading edge follows a prescribed pitching motion at a fixed location while the trailing edge is free to move based on fluid structure interaction. A parametric study

is conducted into the influence of material stiffness and actuation frequency of thrust generation. The simulation consists of a pitching fin within passing flow at Reynolds number 6000 assumed to be laminar flow. The methodology successfully couples CFD–FSI simulations with linear feedback control. A PID controller is set to find the quasi-steady state pitching amplitude for a combination of material stiffness and flexibility. By achieving feedback controlled quasi-steady state swimming it is possible to compare the hydrodynamic performance of fins with different kinematic and material properties. A manually tuned PID controller is proven to be a suitable control strategy with fast convergence towards a quasi-steady state. The numerical study compares three material rigidities, considered as hard, medium and soft respectively.

Results show that, as expected, softer materials exhibit a higher trailing edge deflection, and the trailing edge amplitude is more sensitive to frequency change for elastic materials. While the amplitude of the hard material converges to close to 2 degrees pitching amplitude for all frequencies, the medium rigid material shows a trend towards higher amplitude for higher frequencies, and the least rigid (soft) material peaks at a medium frequency. The observed phase difference between the leading and trailing edges are an indication of the elastic displacement along the fin. While the hard material may be compared to a stiff paddle, the medium and soft materials, excited by the pitching motion, show larger deflection and representation of wave fraction. The medium rigid material at quasi-steady state shows the highest fluctuation of instantaneous body force (drag and thrust peaks) followed by the soft material then the hard material. Higher frequencies lead to larger instantaneous thrust peaks and higher mean thrust and drag. All materials show a trend for higher power expenditure at higher frequencies; however, the medium frequency slope is low at low to medium frequencies and exhibits a drop at the maximum tested frequency. Compared to the soft and hard materials, the medium rigid material exhibits a trend to generally lower energy expenditure and is therefore considered to be performing energetically better. The Strouhal number of all cases remains close to the range of St = 0.2 to 0.4, which is considered in literature to be the optimal range.

The study highlights the complex fluid structure interaction of an elastic fin geometry generating thrust. General trends observed in power expenditures and quasi-steady state amplitudes are interrupted by singular exceptions. This may suggest that the assumption of an evenly distributed and constant fin rigidity is not justified. Future studies may model the fin rigidity more accurately. However, this study provides general data on the thrust performance of elastic plates. Furthermore, it may positively influence design decisions when building caudal fins for bio-inspired underwater robots.

4.3 Combined feedback velocity and position control for analysis of dynamic position holding within incoming flow and in front of a cylindrical body

4.3.1 Problem statement

Fish commonly experience unsteady flow conditions (Liao et al., 2003) stemming from fluid structure interaction around static or dynamic objects leading to upstream low-pressure areas and downstream vortices. Fish are able to adopt to altered flow conditions and have been observed to prefer feeding sites near wing dams, midchannel boulder clusters and natural banks and avoid open areas (Shuler et al., 1994). Also, dolphins are known to swim near ships hulls (Scholander, 1959).

Operation and station holding close to structures is an important component of underwater robotic sensing and manipulation tasks. While conventional thruster propelled vehicles require an extensive amount of energy to maintain a stable position, improved understanding of how fish utilise incoming flow and pressure regions around structures may improve robotic capabilities and reduce energy expenditure.

To investigate the hydrodynamic performance of a self-propelled flexible plate near a cylinder, this work applied a PID controller to dynamically adjust the pitching amplitude of a plate to swim from an initial position to a target position and hold its position at the target location. The setup makes it possible to investigate the dynamic fluid structure interaction between the self-propelled swimmer, incoming flow and cylinder in the swimmer’s wake at different longitudinal distances to the cylinder.

Simulation results support the design of future BAUVs to better interact with their environment for hydrodynamic efficiency and lower power expenditure.

This work represents an extension to the results presented in Section 4.2, in which the swimmer self-propels and moves freely in the horizontal axis to a designated position and holds that position at a cycle-averaged force equilibrium. The horizontal motion of the swimming plate is governed by Newton's second law, given by

$$F_x = m\, u \frac{d}{dt}, \tag{4.9}$$

where F_x is the horizontal force, m is the total mass of the plate and $u\frac{d}{dt}$ is the first derivative of the horizontal velocity of the plate.

Figure 4.20 shows the simulation setup including the original cylinder location, the initial position and the target position of the swimmer. The distance between the initial position and the cylinder is denoted as d_o. The plate chord length is L as is the cylinder $D = L$, the initial position and target position are L apart, so that the initial position is $x_{initial} = p_0$ and the target position is $x_{target} = p_0 - L$. The location of the swimmer is defined by its leading edge.

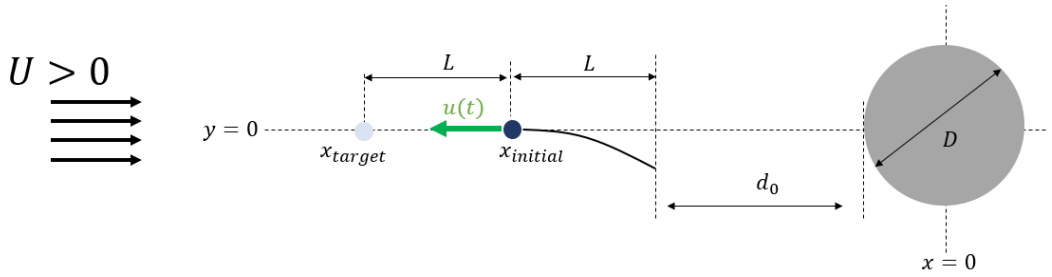

Figure 4.20 Simulation setup. (Luo et al., 2021).

The swimmer is actuated by applying a uniform force to the plate in traverse direction. The leading edge is fixed, while the trailing edge is free to move. The applied force is given by

$$F_{ef}(t) = c_a\, F_{ef0} \sin\left(2\pi\, f_{ef}\, t\right) \tag{4.10}$$

where F_{ef0} is the maximum force amplitude defined by $F_{ef0} = 0.5\rho_f U^2 L\, c_{ef0}$, with c_{ef0} the actuation force coefficient, t is the time and f_{ef} the frequency. Control variable c_a is determined by the PID controller and adjusts the force amplitude between 0 and 1 according to the control error defined in Equation (3.38). Control variable c_a regulates the pitching motion between zero and the maximum amplitude. Starting at zero pitching, the pitching amplitude is functioned to achieve two control targets: firstly, to swim towards a target point and, secondly, to hold position at the target position.

The dimensionless parameters governing this problem are defined as follows: the reduced frequency $f^* = fL/U$; the mass ratio $m^* = \rho_s h/\rho_f L$ with ρ_s and ρ_f the density of the structure and fluid respectively and h is the thickness of the fin; the dimensionless stiffness $K = EI/(\rho_s U^2 L^3)$ where E is Young's modulus and $I = h^3/12$ is the area moment of inertia of the cross section.

Table 4-4 summarises constant values of the setup including the stiffness of the plate K and PID control gains derived through the Ziegler-Nichols tuning method (Ziegler and Nichols, 1942).

Table 4-4 Overview of constant variables.

K	c_{ef0}	m^*	K_P	K_I	K_D	T_h	T_{set}
0.5	2.0	0.5	7 & 15	0	0.05	$20\,T$	$4.2\frac{U}{L}$

4.3.2 Simulation setup

The computational domain is 20L by 55L with the position of the cylinder located in the vertical centre at 10L and 15L from the left boundary, as shown in **Error! R eference source not found.**.

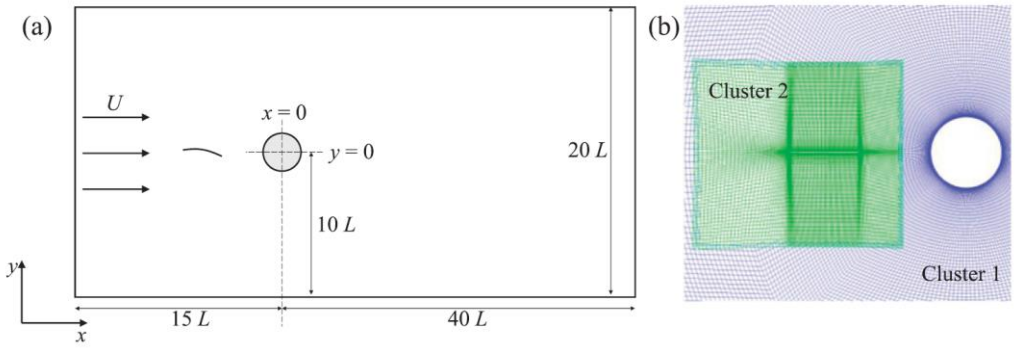

Figure 4.21 (a) schematic of simulation domain and
(b) top view of an overset mesh. (Luo et al., 2021).

The plate is located horizontally to the left of the cylinder at distance d_0 measured at the leading edge of the plate. Small mesh motion is achieved via mesh smoothing, large mesh displacement is accounted for by means of an overset mesh surrounding the plate. There are three meshes in total: the fluid domain mesh, the plate overset mesh and the plate structure mesh. Following a mesh and time step independency study (details provided in (Luo et al., 2021)), a total mesh number of 103,888 and a time step of $\widetilde{\Delta t} = \Delta t \frac{U}{L}, \widetilde{\Delta t} = 0.00333$ are applied. A non-slip boundary condition is imposed on all surfaces of the cylinder and swimmer. The fluid domain boundary conditions are velocity inlet (left boundary) and a non-reflective far field boundary condition (horizontal and right boundary)

4.3.3 Results and discussion

4.3.3.1 Effect of d_0 on static plate in front of the cylinder

Comparable to the results reported in Wu et al (2014)), the presence of a cylinder in the downstream position of a fixed plate leads to drag reduction on the plate. Shown in Figure 4.22, for a constant $Re = 1000$, the drag force reduces when the cylinder is moved towards the plate. The reduced drag translates into reduced required effort to maintain position, making the closer position towards the cylinder energetically favourable.

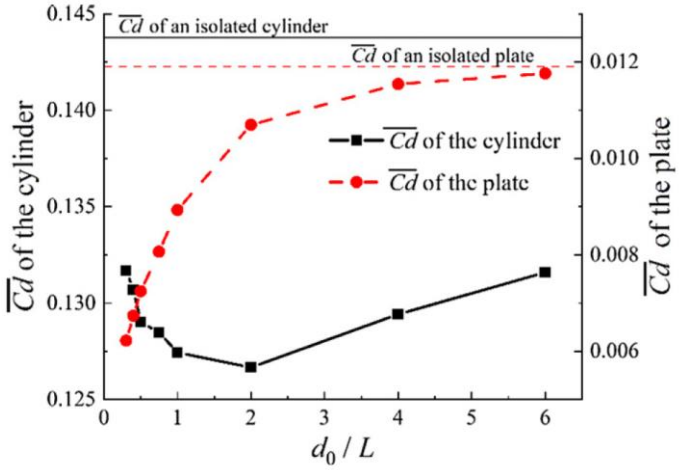

Figure 4.22 Average drag coefficient c_d of plate and cylinder over distance d_0/L. (Luo et al., 2021)

A similar effect is observed for the cylinder; however, the drag reduction peaks at $2\frac{d_0}{L}$

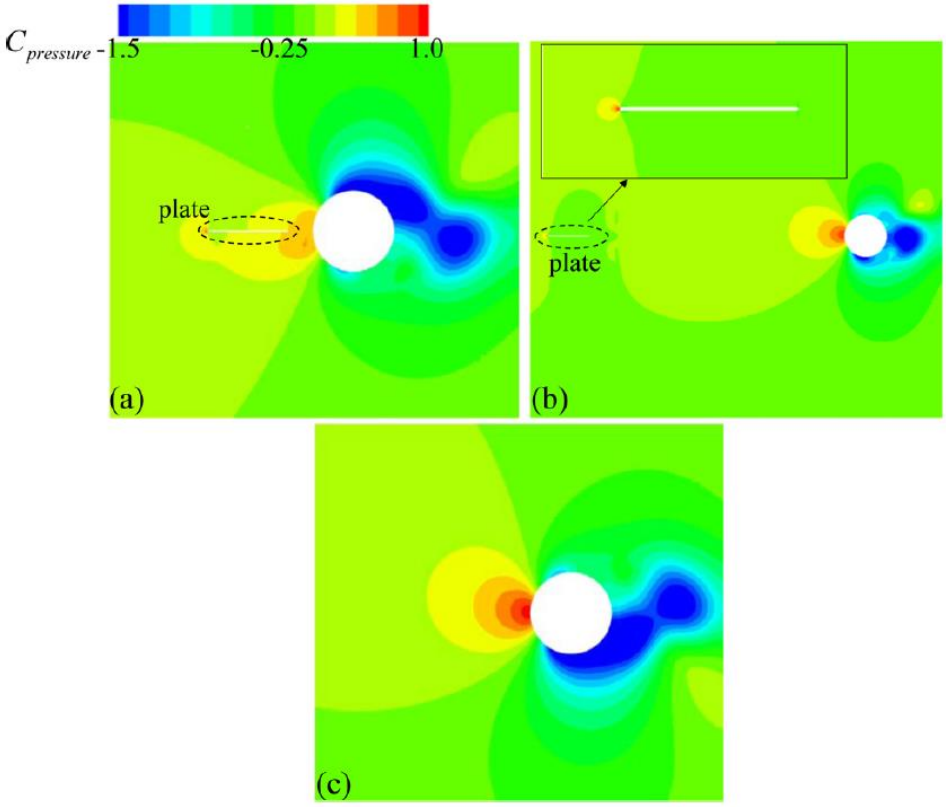

Figure 4.23 pressure coefficient contour at $\frac{tU}{L} = 104$ of (a) $d_0 = 0.3L$ (b) $d_0 = 6L$ and (c) without plate. (Luo et al., 2021).

The contours show that for small d_0, (a), the plate's trailing edge is within the high-pressure zone in front of the cylinder, see Figure 4.23 (a). For a large d_0, the high-

pressure zone is unaffected, see Figure 4.23 (b) and develops in a similar manner to the isolated cylinder in Figure 4.23 (c).

4.3.3.2 Effect of Re on moving plate in front of cylinder

The next step is an analysis of a pitching plate moving towards a target point as described in Figure 4.20. The designed PID controller error logic makes it possible to make a comparison at quasi-steady state equilibrium across different Reynold numbers $Re = [500,1000,1500]$, in other words, free stream fluid velocities.

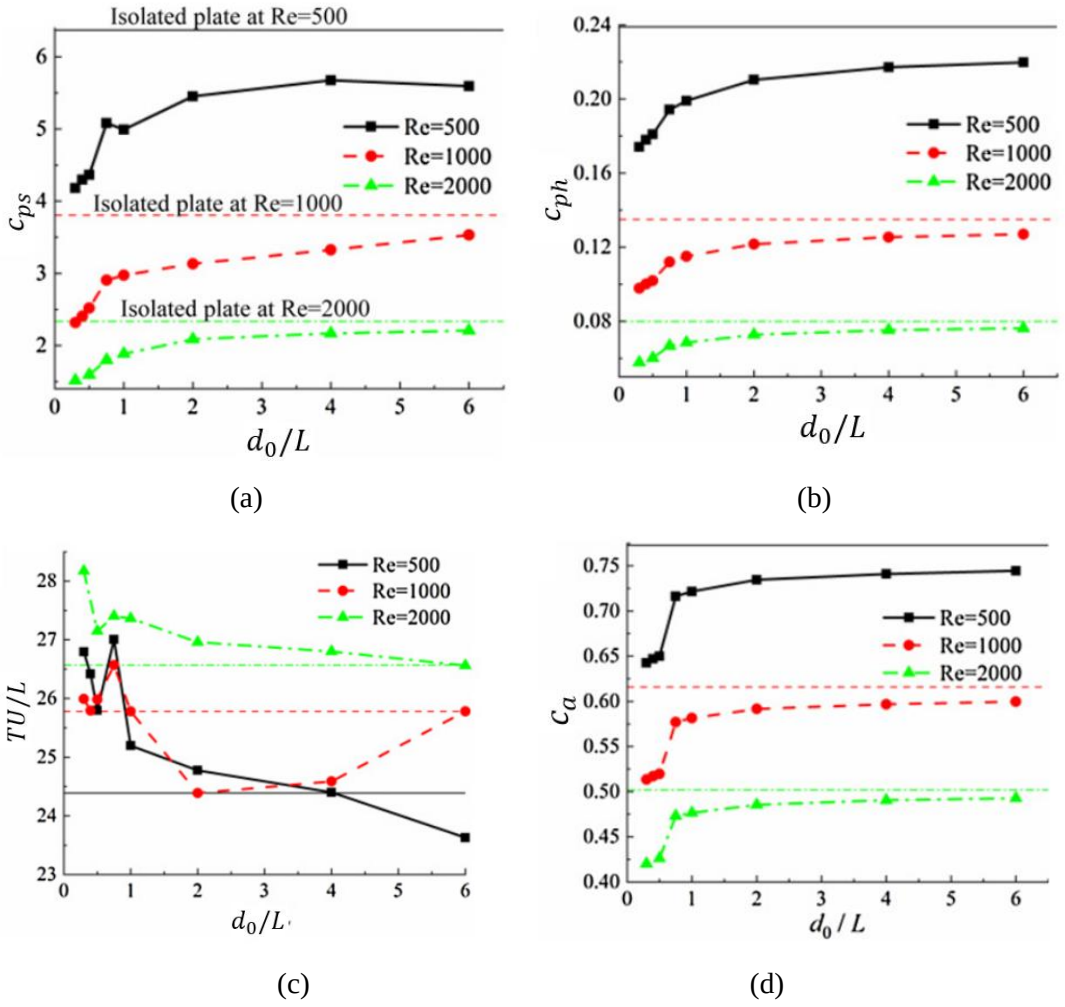

Figure 4.24 Quasi-steady state values at $f^* = 2.5$ over a variable relative distance $\frac{d_0}{L}$ of (a) total power expenditure coefficient C_{Ps} (b) mean power expenditure coefficient C_{Ph} (c) convergence time T_S and (d) converged control variable α_h. (Luo et al., 2021).

Figure 4.24 (a) and (b) show the overall energy expenditure coefficient C_{Ps} and mean energy expenditure coefficient C_{Ph} in a holding position at the target position. For

smaller distances $\frac{d_0}{L}$ the decrease in power expenditure is explained by a reduction in drag similar to that of the static plate. The required power drops significantly for all Re at a distance of d_0 <L. The greatest energy saving compared to the isolated plate is achieved at Re = 1000 and at a distance $d_0 = 0.3L$, which achieves a reduction in the overall energy expenditure coefficient of 38% compared to when there is no cylinder present. Results show the Reynolds number to be a significant factor in the projected energy coefficient. For $d_0 = 0.75\,L$, 183% more energy is needed for Reynolds number $Re = 500$ compared to $Re = 2000$. These results show that higher Reynolds numbers are energetically favourable. Further, the total energy coefficient and mean energy coefficient at the target position follow the same pattern. Both point to the conclusion that the closer the plate swims in front of the cylinder the lower the effort required to hold its position.

Figure 4.24 (c) plots the required time T_S to travel towards the target position and reach a quasi-steady state holding station and Figure 4.24 (d) plots the converged quasi-steady state control variable c_a. Both graphs indicate a more complex fluid structure interaction at small d_0, hence, the longer convergence times and the positive relation between the pitching amplitude and thrust generation. Considering Figure 4.24 (a) and Figure 4.24 (c), lower steady state energy savings do not necessarily mean time savings. For comparison, values for the isolated plate without the presence of the cylinder are included. Comparison of results with and without the presence of a cylinder show that the total power expenditure, mean power expenditure and required pitching amplitude is reduced for all cases. For $Re = 500$ and $Re = 2000$, the majority of cases show an increase in convergence time, not so much for $Re = 1000$. This may be due differences in the speed of which generated vortices move downstream and interact with the cylinder, suggesting an available optimum in the relation between swimmer distance and vortex shedding generation.

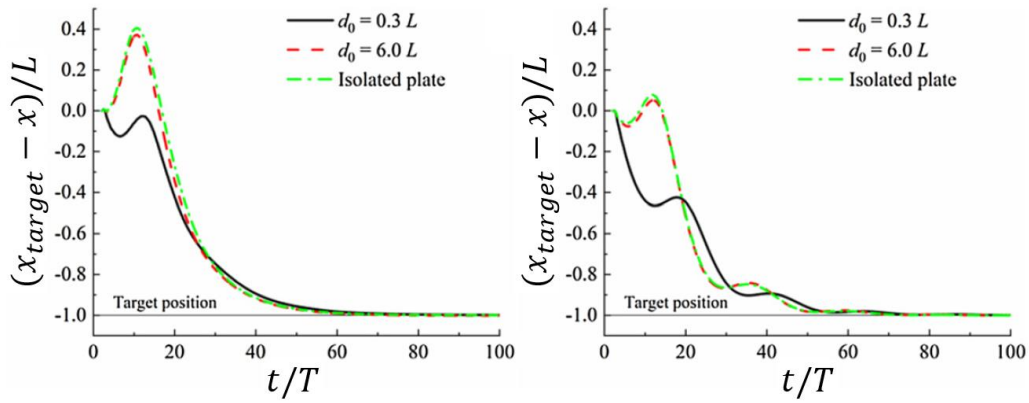

(a) (b)

Figure 4.25 Instantaneous displacement at $f^* = 2.5$ of isolated plate, $d_0 = 0.3\ L$ and $d_0 = 6\ L$ for (a) $Re = 500$ and (b) $Re = 2000$. (Luo et al., 2021).

A comparison of the instantaneous displacement for Re 500 and Re 2000 in Figure 4.25 reveals that for a greater distance between the plate and the cylinder $d_0 = 6\ L$, the displacement is identical with the isolated plate, whereas for a small gap $d_0 = 0.3\ L$ initial downward drift is avoided.

Corresponding nondimensionalised velocity curves in Figure 4.26 show a period of strong acceleration followed by a period of deceleration and subsequent convergence towards a quasi-steady state.

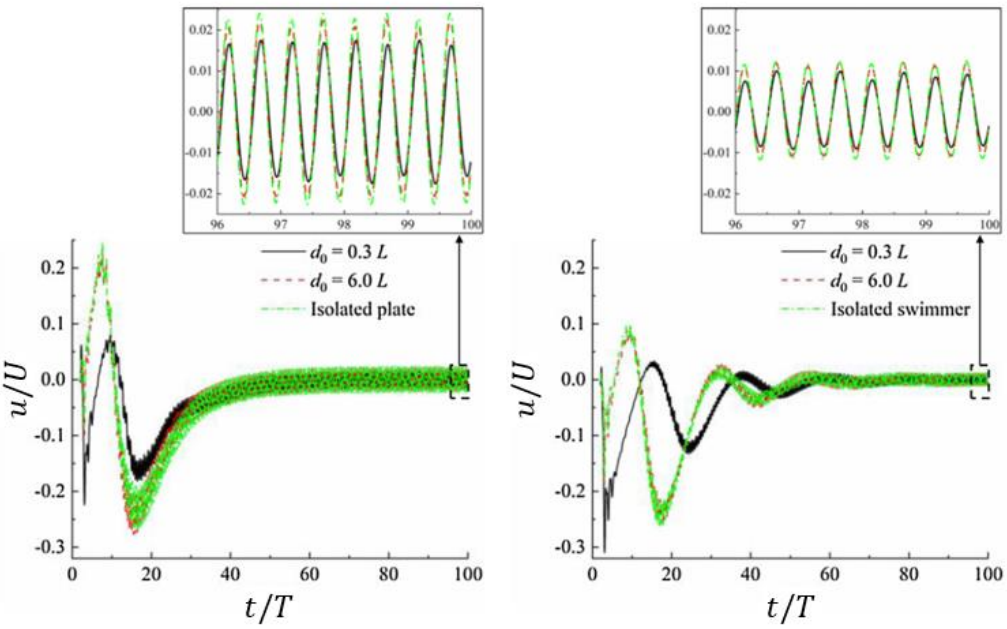

Figure 4.26 Instantaneous velocity at $f^* = 2.5$ of isolated plate, $d_0 = 0.3\ L$ and $d_0 = 6\ L$ for (a) $Re = 500$ and (b) $Re = 2000$. (Luo et al., 2021).

Fluctuation is caused by the adjusting controller response reacting to the strong initial acceleration of the pitching plate. A comparison of the control variable α in Figure 4.27 shows a more damped response for $Re = 500$. The difference in Reynolds numbers will lead to a difference in error magnitude, suggesting that the control parameters are more suitable for $Re = 500$.

Both Reynolds numbers show an equal amount of convergence time, in other words, no time advantage. Figure 4.26 confirms the implemented control logic in that the swimmer reduces its velocity as it approaches the target position and achieves quasi-steady state force equilibrium within the passing flow and resulting close-to-zero mean velocity. It is found that the instantaneous velocity amplitude within the holding position is lower for Re=2000 ($u_b = \pm 0.01U$) compared to Re =500 ($u_b = \pm 0.02U$), as is shown in Figure 4.26.

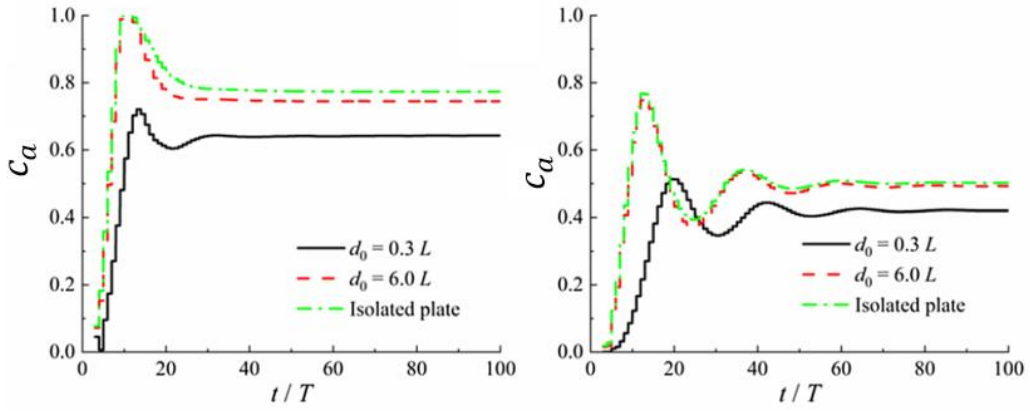

Figure 4.27 Instantaneous control variable α at $f^* = 2.5$ of isolated plate, $d_0 = 0.3\ L$ and $d_0 = 6\ L$ for (a) $Re = 500$ and (b) $Re = 2000$. (Luo et al., 2021).

The generated vortices and reversed Karman vortex street in the wake of the plate is visible in the vorticity contours of Figure 4.28. Clockwise and anticlockwise vortices, which result in a mean forward thrust, are coloured in red and blue respectively. As the figure shows, vortices are at the plate's trailing edge as well as around the cylinder.

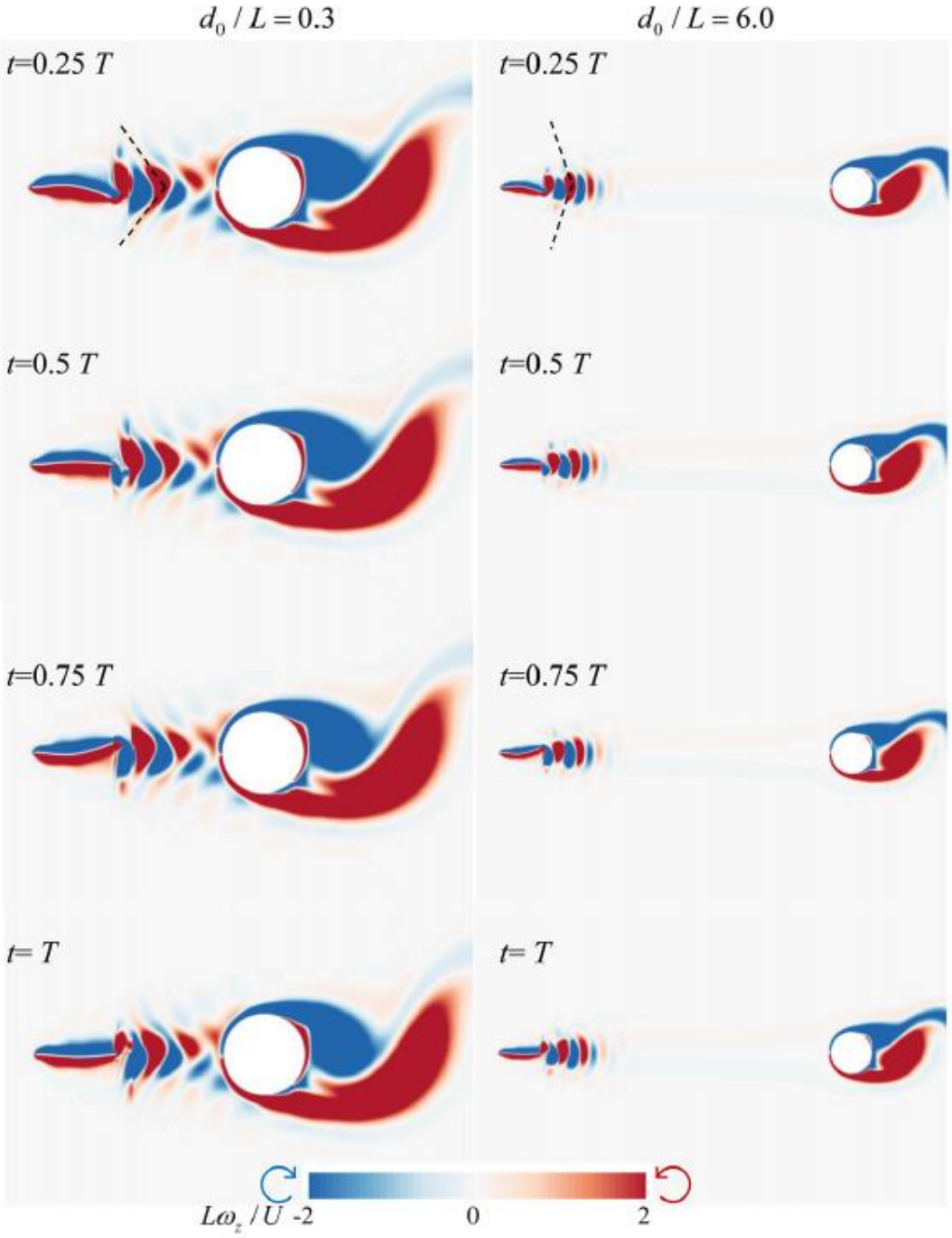

Figure 4.28 Z-vorticity contour at quasi-steady state and $f^* = 2.5$ for $Re = 500$ and $f^* = 2.5$ for (left column) $d_0 = 0.3L$ and (right column) $d_0 = 6L$. (Luo et al., 2021).

The process of vortex shedding is a key component of the thrust mechanism and the vorticity contour in Figure 4.28 shows that the presence of a cylinder in the wake of the plate influences the vortices formation in the wake. For a plate swimming close to the cylinder $d_0 = 0.3\,L$ the vortices are compressed, indicated by the narrower V shape formation. When quickly coming into contact with the high-pressure zone acting

on the cylinder towards the passing flow, the vortices interact with their upstream neighbours. In contrast, for a greater distance $d_0 = 6\,L$ the vortices, as in the case of an isolated plate, can flow downstream undisturbed continuously losing momentum before passing the cylinder.

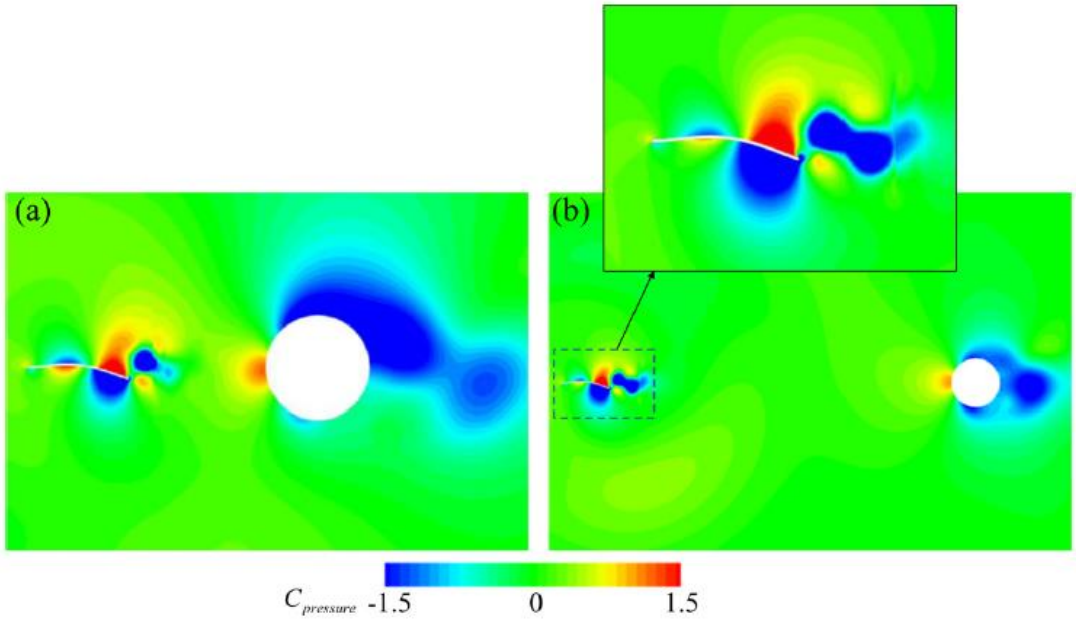

Figure 4.29 Instantaneous pressure contour for $Re = 500$ and $f^* = 2.5$ of (a) $d_0 = 0.3L$ and $d_0 = 6L$ (Luo et al., 2021).

The high-pressure zone acting on the cylinder is visible in Figure 4.29. When swimming close to the front of the cylinder, interaction between the high-pressure zone of the cylinder leads to a reduction in the low-pressure zone of the plate at the trailing edge, resulting in an overall reduction of drag and a related reduction in effort to hold position.

4.3.4 Conclusion on combined velocity and position feedback control for analysis of dynamic position holding within incoming flow in front of a cylinder

Fish perform unsteady locomotion the majority of their time as a reaction to flow conditions and for continuous adaptation to their environment. Fish commonly experience unsteady flow conditions created, for example, by flow around structures or general current dynamics. The ability to adapt to changing conditions enables fish to maintain stability and efficiency.

Understanding the complex fluid structure interaction between fish swimming close to a structure may provide insights into how to develop robotic systems and improve station holding capabilities during, for example, inspection operations.

The conducted numerical investigation aims to support better understanding of the fluid dynamics of a BCF swimmer holding station within passing flow close to a structure. The applied methodology consists of coupling a CFD-FSI solver with feedback control to facilitate dynamic station holding and to make a comparison between different materials at setpoint conditions. In this study, the BCF swimmer is approximated as a 2D elastic plate swimming and holding position within a velocity stream and at variable distances in front of a cylinder. The CFD-FSI simulation environment provides a coupled solution of the fluid and structure equations so that the leading edge is a rigid reference point moving according to Newton's second law while the remaining plate structure moves according to actuation and surface forces. The self-propelled horizontally moving swimmer is subject to instantaneous forces and acceleration. A feedback controller is designed and implemented to lead the swimmer towards and hold at a target location one body length in front of the varied initial position. Holding position within passing flow requires the swimmer to reach a quasi-steady state at which the power expenditure is compared. Observations confirm, a converging controller output leads to periodic stable hydrodynamics over one undulation period. For general comparison throughout the study, a reference case is given with a swimming plate without a cylinder. Results assess the influence of the distance towards the structure and related hydrodynamics effects on the station holding ability and effort.

The presence of a cylinder in the wake of a plate indeed leads to reduced drag acting on the plate and cylinder. CFD simulation results also show for smaller distances between cylinder and plate lead to smaller plate drag. Also, the drag of the cylinder reduces for a plate up to a distance of 2 body lengths and then increases again for smaller distances.

For a self-propelled swimmer, the energy required to swim a distance of one body length and hold position reduces at decreasing distances to the cylinder. The power expenditure drops significantly when the initial position is less than 1 body length from

the cylinder. Overall, higher Reynolds numbers show lower power expenditure leading to the conclusion that a higher Reynolds number is energetically favourable. With reducing distances to the cylinder, the plate requires more time to converge to a quasi-steady state and requires a lower amplitude corresponding to the lower required power. For higher distances between the plate and cylinder, the instantaneous trajectory converges towards the reference case, in other words, the plate without a cylinder. An analysis of the vorticity contours reveal interaction between the low-pressure zone in front of the cylinder and the reversed vortex street of the plate as an explanation for the improved hydrodynamic performance of the swimmer swimming closer to the cylinder.

In summary, the work confirms the energetically positive fluid structure interaction between a self-propelled swimmer and the wake structure. Future studies may extend to varying the elasticity and geometry of the plate and increasing variation of the kinematic parameters.

Chapter 5 Design and development of a bio-inspired underwater vehicle

5.1 Introduction to the design process and requirements

Bio-inspired autonomous underwater vehicles are designed to mimic the high efficiency abilities of underwater creatures. Analogue to best practices, processes and challenges of designing and engineering a physical system, the creation of a bio-inspired robot entails an iterative process of design decisions within a large parameter space. The process is guided by the targeted features of the system and is constrained by the available resources.

The goals of the design process are set out at the beginning as follows: the targeted design shall mimic the general structure and kinematics of a BCF swimmer to achieve a good compromise between a low drag slender design for long distance travel and high manoeuvrability. The cost shall be limited to £2500 and the overall size of the design shall be within 1 meter in length to enable testing in the available water tank.

The vehicle shall operate untethered to swim freely and shall be multi-actuated to enable assessment of performance for different kinematic parameters.

A new vehicle design is developed that includes the novel application of synchronous magnetic joints to allow statically sealed and actuated flexibility between neighbouring body modules. The implemented design creates a modular structure that mimics an eel. The underlying modularity creates a versatile and extendable system that is sufficiently robust while promising anticipated efficiency improvements from a bio-inspired design structure. The design addresses a key weakness of existing modular robotic designs in that it avoids dynamic seals and flexible covers by presenting a novel magnetic coupling solution. The designed magnetic coupling allows for true mechanical modularity and future development of a self-configuring underwater robotic system. Many configurable modular robotic systems for research have been developed (Chennareddy et al., 2017;Liu et al., 2016) but to the best of the author's knowledge, only one of these reconfigurable systems has been designed for underwater operation as part of a bio-inspired swimmer.

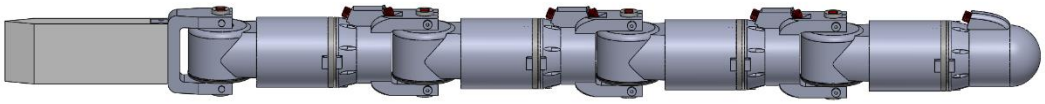

(a)

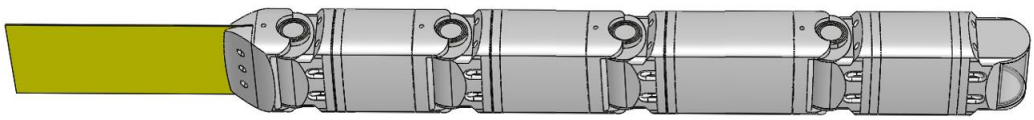

(b)

Figure 5.1 Created robotic designs by the author: (a) First design iteration named "RoboFish" (b) Second design iteration named "Modular Multi-body Autonomous Underwater Vehicle" (MMBAUV)

In the following, key aspects of the design and construction are presented and discussed on the creation of a bio-inspired underwater autonomous vehicle. The first design iteration, shown in Figure 5.1 (a), was created during the EPSRC Supergen ORE funded project: "Autonomous Biomimetic Robot-fish for Offshore Wind Farm Inspection". The author contributed to the project providing the mechanical design including CAD modelling and the magnetic coupling idea and design. The second

design iteration, shown in Figure 5.1 (b), is fully designed and built by the author and is therefore discussed in more detail. Parts of this Section are published in (Wright et al., 2020a;Wright et al., 2023a).

5.2 Development of magnetic coupling

5.2.1 Mechanical design

A synchronous mechanical coupling between two physically separated shafts is achieved by means of a magnetic attraction force. Typically, attracting magnetic forces are generated from permanent magnets or electromagnetic coils. Because the latter relies on a constant energy supply to maintain an induced magnetic field, the design focuses on permanent magnets. Magnetic couples are fixed to a driven side and a load side and are typically arranged in either an axial or coaxial configuration, as shown in Figure 5.2. Synchronous motion is maintained through a restoring torque relative to the displacement angle between the two sides, the so called load angle (Nagrial et al., 2011).

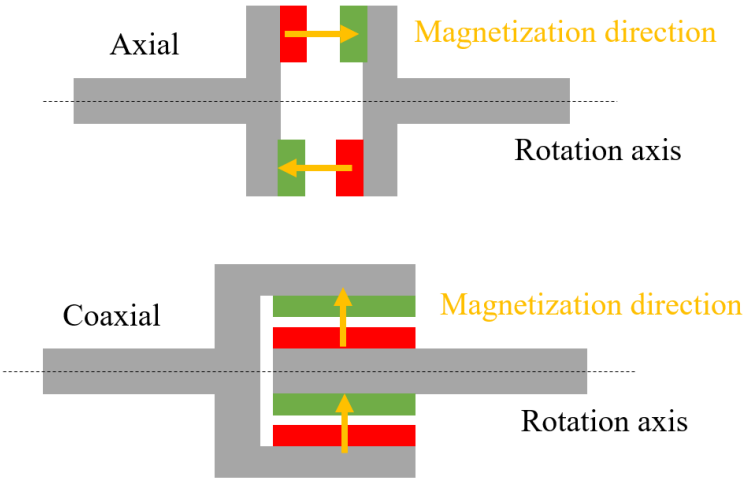

Figure 5.2 Magnet coupling arrangement. (Wright et al., 2023a).

When the load difference between the two sides exceeds the maximum magnetic coupling torque, coupling may be lost and “slip” occurs. Consequently, it is important to design the magnetic couples to provide sufficient coupling strength for the target application.

The design process led to the creation of two iterations of a synchronous coupling for application in a bio-inspired underwater robot. Both designs show a coaxial magnet arrangement for increased torque transfer. The first design consists of twelve permanent magnet couples arranged around an inner driven shaft and surrounding hollow drive shaft. The drive shaft is located enclosed within a module housing and the drive shaft is exposed to water resulting in the magnets being separated by a gap made up of a layer of water, enclosure and air. The driven shaft connects at each end through lever arms to the neighbouring module, as seen in Figure 2.14(a).

The joint design achieves a strong magnetic bond and smooth transfer of torque between the two sides of the coupling but is relatively heavy due to the required structure and number of magnets. The fixed mechanical lever arm is a potential weak point during peak load stress and the arrangement of the inner shaft requires detailed assembly considerations to ensure a mechanically sound design.

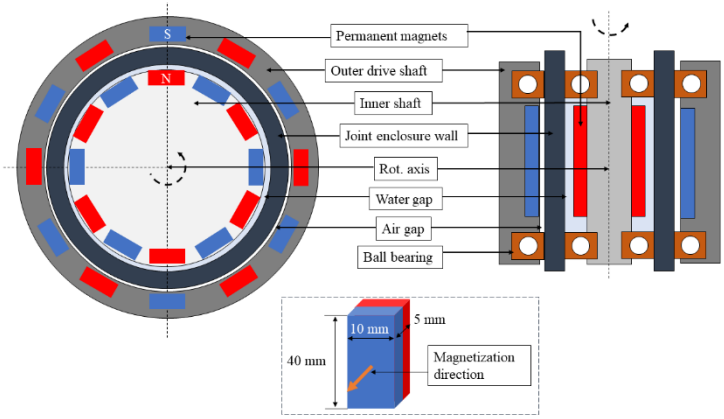

Figure 5.3 Schematic of 360-degree magnetic joint arrangement. (Wright et al., 2020a).

The second design iteration is lighter, can safely disconnect when experiencing forces above design loads, avoids structural weakness of mechanically fixed lever arms and is less complex to assemble.

A key design change is the reduction in the number of magnets and arrangement from a full circumference to an arc shape. The driven shaft magnets are incorporated in the curved surface of the ascending body module forming the joint. The arc shape reduces the magnetic coupling surface and allows the driven side to be guided along the outer wall of the enclosure in which the driver side is placed. Rounded off edges of the driven side module ensure sufficient freedom of rotation and the overall arrangement

results in a relatively smooth surface across the joint, compared to the 360-degree magnet joint arrangement. The updated arrangement achieves significant weight reduction and avoids a fixed mechanical coupling and a potential weak point of lever arms of the original design iteration. Further, this allows for modules to decouple when experiencing extreme external loads. Under normal operating conditions decoupling does not appear due to the characteristics of the viscous, self-supporting nature of water and a push force between the coupled modules when the fish is swimming.

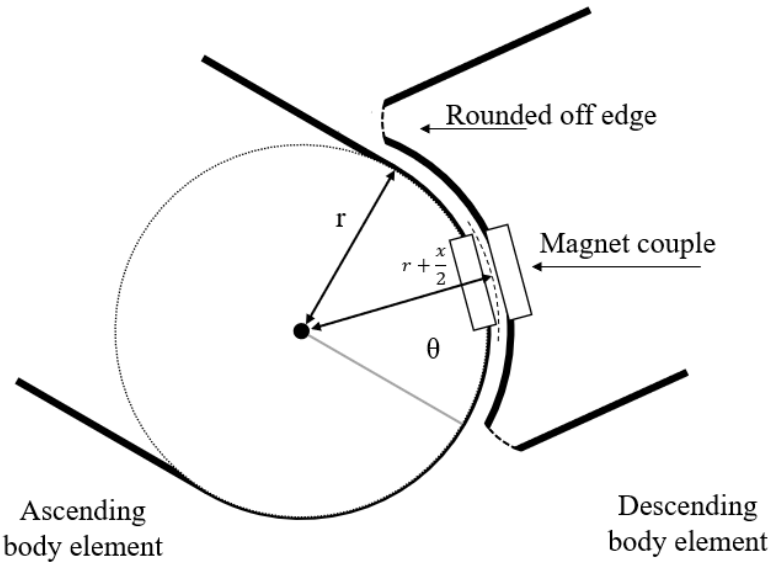

Figure 5.4 2D schematic of neighbouring arrangement of new magnetic joint.
(Wright et al., 2023a)

In addition to torque transmission, the proposed design makes use of the attractive force in the magnetisation direction to align and hold neighbouring body modules, with the descending module resting atop the neighbouring module's ball bearing.

5.2.2 Calculation of coupling force

For the calculation of the magnetic coupling strength, a joint is assumed to consist of *n* pairs of magnet couples in an alternating arrangement. The alternating arrangement makes use of the repelling force of neighbouring magnets of the same polarity. To reduce the cost of the initial prototype, only widely available cuboid shaped neodymium magnets are considered. The final coupling provides one Degree of

Freedom (DoF) between neighbouring body modules to enable the shaping of a travelling wave in the common plane of rotation of the joints.

Figure 5.5 shows the force vector, for a normal distance Δx and perpendicular distance Δy for a single magnetic couple that ensures connection in normal and rotational directions. The force vector direction of the cuboid magnets is noted in the variable index and the dimensions of the magnets are denotated by *W*, *L* and *T* for width, length, and thickness respectively. While a sufficiently strong normal holding force F_x between magnets is easily achievable, it is critical to design the maximum sheer force F_y to reduce the load angle and avoid slip.

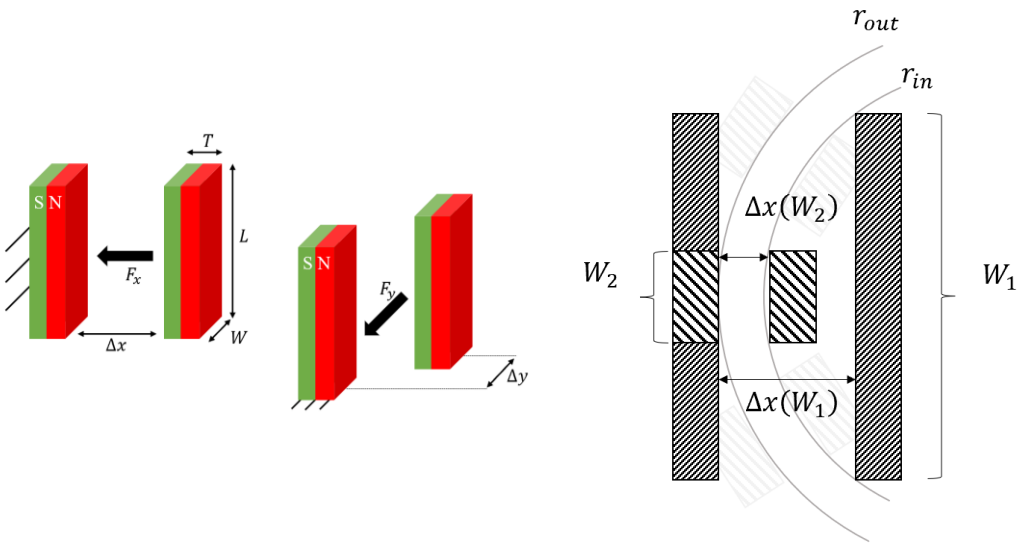

(a) (b)

Figure 5.5 (a) Restoring force F_x and F_y at Δx and Δy displacement of magnets (b) magnet normal distance Δx(W) for different cuboid magnet width W.(Wright et al., 2023a).

To support the design process, an approximation model is used that is sufficiently accurate and fast to support an iterative design process. The maximum transferable torque, τ_{max}, is approximated by a function of the number of magnet couples n, the maximum sheer force $F_{y,max}$, the radius $r + \frac{\Delta x}{2}$ between the joint centre and the half distance $\frac{\Delta x}{2}$ between the two magnets

$$\tau_{max} = \left(F_{y,max}\left(r + \frac{\Delta x}{2}\right)\right)n. \tag{5.1}$$

The magnetic forces F_x and $F_{y,max}$ are calculated using equations published by Schomburg et al. (Schomburg et al., 2020). Accordingly, F_x can be approximated as follows

$$F_x = \frac{d_e^2}{[\Delta x + d_e]^2}\, F_0, \tag{5.2}$$

where F_0 is the force F_x at magnet distance zero (Δx=0), and the variable d_e is the distance between magnets at which the normal force F_x is one quatre of the normal force at zero magnet distance, hence, $F_x(d_e) = \frac{1}{4}F_0$. To identify d_e, values for $F_{x=0}$ and $\frac{1}{4}F_{x=0}$ are computed by means of a magnetostatic FEM simulation using EMS (EMSworks, 2022) for Autodesk Inventor (Munford and Normand, 2016). The maximum shear force in the X-Y plane is approximated by

$$F_{y,max} = \frac{1}{1.11 - 0.244exp\left(-2\left[\frac{L_1}{L_2} - 1\right]\right)} \frac{F_0}{L_2} \frac{d_e^2}{x + d_e}. \tag{5.3}$$

Here, $\frac{L_1}{L_2}$ is the length ratio between magnet couples and remains equal to 1. As shown in Equations (5.2) and (5.3), the coupling strength is directly related to the magnet strength, magnet dimension, and the normal distance between magnet couples. Figure 5.5 (b) shows, for varying magnet distance, the normal distance between magnet couples converges towards the wall thickness and the air gap between the two connected modules. For a given radius *r*, the magnet width and depth are found by balancing the magnet dimensions, the maximum possible magnet couples, and the smallest possible normal distance between magnet couples. Restricting factors include the limited space available around the inner and outer shafts. The height of the magnets is determined based on factors including overall module height, related to the module aspect ratio and buoyancy volume as well as the centre of gravity.

The final derived design consists of *n* = 4 magnetic couples arranged at a radius of $r = 32mm$ and a magnet couple distance of $\Delta x = 6\,mm$. All magnets are cuboid NdFeB magnets measuring 40x10x5 mm (LxWxH). As shown in Figure 5.6 (a), the design's attracting normal force between each magnet couple is $F_x = 19.2325N$ and the

maximum shear force is $F_y = 22.8746N$. According to Equation (5.3), this results in a maximum transferable torque of τ_{max} = 2.4533 Nm. In comparison, the magnetostatic simulation results calculated a maximum torque of $\tau_{max} = -2.6315Nm$ at 14 degrees load angle. Figure 5.6 (b) shows results of the magnetostatic simulations for different load angles and the resulting restoring torque.

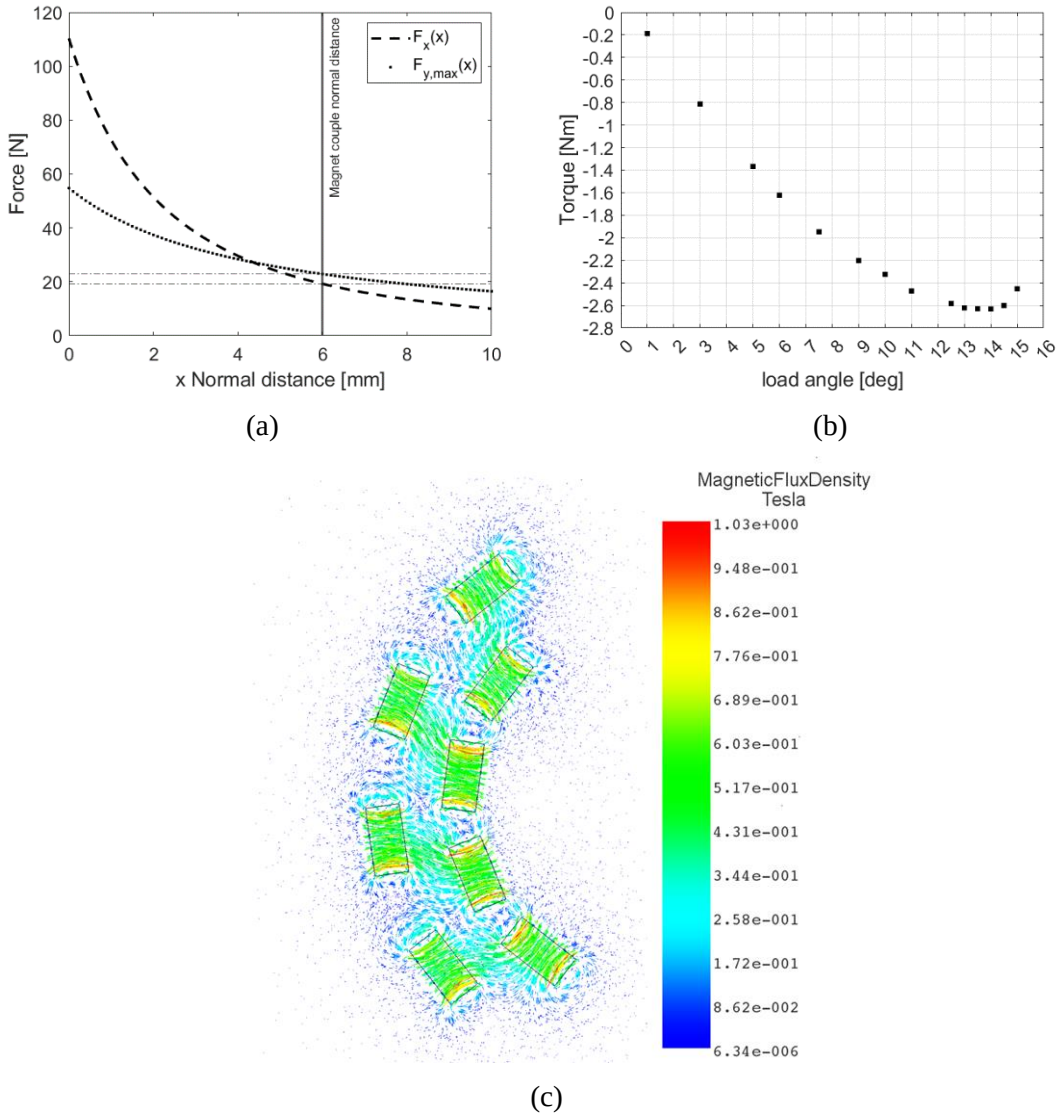

(a) (b)

(c)

Figure 5.6 (a) force curves according to Equations (5.2) and (5.3), (b) FEM results of maximum load torque for different load angles (c) section view of magnetic field intensity plot at 14 degrees load angle. (Wright et al., 2023a).

The section view of the magnetic field, shown in Figure 5.6 (c), shows the connecting field lines between magnet couples and the minimum magnetic field intensity between magnets of the same polarity. During operation, the opposite magnet poles will attract

and the equal magnet poles will repel, resulting in a restoring torque for the driven side to follow the drive side.

5.3 Electronic circuit design, communications and control

Each module houses an identical set of electronics to enable actuation of the drive shaft and enable wireless communications between each module and a controlling laptop. Each circuit is built around an Arduino NANO 33 BLE and is powered by two 18650 batteries connected in series via a 2S Battery Management System (BMS) resulting in 3000mAh capacity and a supply voltage between approximately 7V - 8.4V. The joint is actuated by a Hitec HS-646WP servo motor. Each joint is driven via an HTD M5 timing belt connected to a servo pulley with a gear ratio of 12:32. The design allows for a maximum rotation angle of ± 35 degrees between two modules given by the mechanical constraint of intersecting neighbouring modules and the gear ratio between pulley, shaft and servo motor. The servo power is measured by the Adafruit INA260 breakout board which is powered via the Arduino board's 3.3v pin and communicates via a I2C bus. An additional Zener diode, a capacitor, and two Schottky diodes are added to protect the Arduino's Vin pin from over-voltage and reverse current transients caused by rapid servo movements. A 12-volt TDK WRM483265-10F5-12V-G wireless charging coil is installed at the bottom of each module. A switch makes it possible to turn off the module while wireless charging continues. Figure 5.7 shows the full module circuit design.

Wireless communications to maintain remote control of the robot is required to facilitate untethered swimming. With the trials of the prototype being held exclusively in a lab environment, Bluetooth Low Energy (BLE) has shown to provide effective and reliable connectivity when the robot is swimming close to the surface.

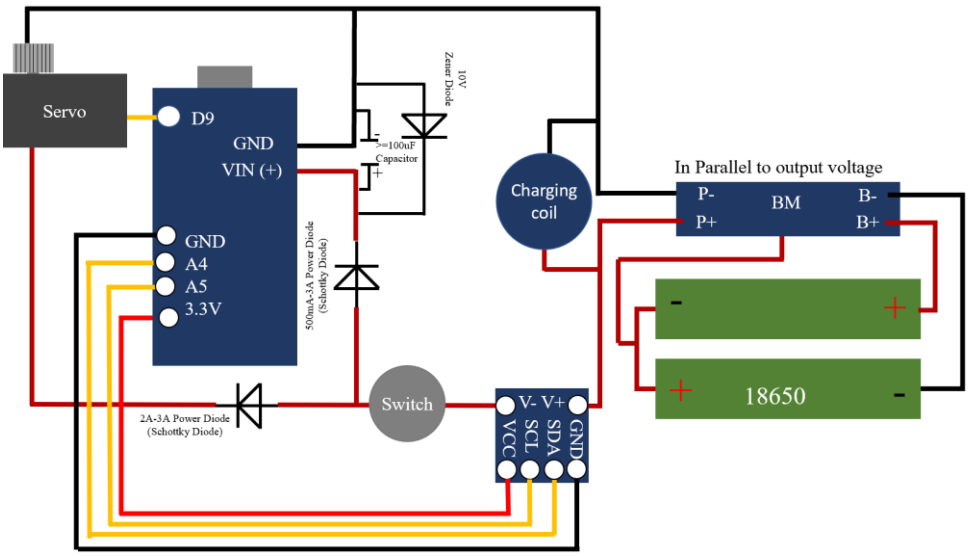

Figure 5.7 Module circuit schematic. (Wright et al., 2023a).

Communications are established between each module (slave) and a laptop (central master). Two-way data transfer, at a BAUD rate of 115200, is established between the central device (laptop) and each individual module (Arduino board). As a result, the modules do not communicate directly with each other but the data of each module is received, processed and returned at the central device. Each module is identified by a Universal Unique Identifier (UUID). Following standard BLE format, transferred data is organised in *Services* and *Characteristics*, which can be selectively made available for each data link at the central device.

BLE communications are setup via a MATLAB function within Simulink. Robot kinematic parameters can be changed online and live data, such as servo power, is recorded.

The robot structure can form a traveling wave via oscillation motion of its joints at a phase difference according to their body position. Each joint follows a sinusoidal oscillation according to its position along the swimmer and Equation (3.30).

The maximum frequency is calculated by $f_{max} < \frac{\omega}{A(L)2\pi}$with $\omega = \frac{60}{0.2}\left[\frac{deg}{sec}\right]$ being the no load servo velocity. The max torque is calculated to be 9.6 ~ 11.6 kg/cm provided by the Hitec HS 646 WP Analog Servo.

5.4 CAD design, prototyping and assembly

Additive manufacturing, also known as 3D printing, offers fast and low-cost prototyping of complex geometries. The two well established methods of Fuse Deposition Modelling (FDM) and Digital Light Processing - Stereolithography (DLP-SLA) are used.

A first prototype was created using Fuse Deposition Modelling (FDM). The print material Acrylonitrile Styrene Acrylate (ASA) filament is used due to its high strength, impact and chemical resistance compared to alternatives such as Polylactic acid (PLA). Key printing parameters that influence the quality and accuracy of the print include extrusion temperature and speed, depositing nozzle size and print bed temperature. Final print results may also be influenced by external factors such as ambient temperature and forced convection from air fluctuation, for example, draught from an open window or air conditioning.

Challenges in waterproofing the created components layered structure and poor dimensional tolerances led to changing to SLA 3D printing technique for the second prototype.

The second prototype is created using a Digital Light Processing - Stereolithography (DLP-SLA) printer: ANYCUBIC Photon Mono (ANYCUBIC, 2022). SLA printing is a well-established method but not as common as FDM printing. It is slightly higher in cost and requires handling of a liquid resin, adding to the production steps, such as washing and curing the final printed part. The print processes consist of a built plate that is lowered into a liquid print resin located in a basin with a transparent bottom, so called FEP, located above a UV light. The Anycubic photon Mono printer achieves a print resolution of up to 50 micros determined by the screen resolution. Print failure and part deformation during the printing process can result from printing enclosed cavities that lead to a pressure difference, the so-called “suction cup effect”, extensive overhang or an insufficient support structure resulting in unsupported new layers.

The finished parts are coated with a UV blocking spray to extend the longevity of the parts and stop the materials from further solidifying when exposed to UV light, for

example, during transport. No degradation of part quality or structural integrity was observed over several months of tests. Figure 5.8 shows the SLA printer during the print process and the completed 3D printed structure parts of the head and body modules.

(a) (b) (c)

Figure 5.8 (a) SLA 3D printer and structure parts of (b) a head and (c) a body module.

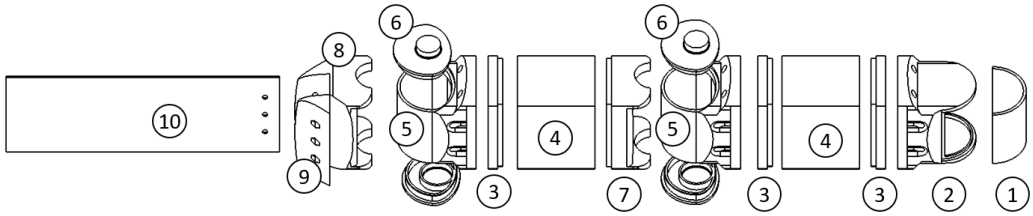

Figure 5.9 (1) front window (2) head frame, (3) electronic housing flange, (4) electronic housing, (5) joint housing, (6) joint housing cap, (7) magnet housing, (8) tail main frame, (9) tail fastening bar, (10) tail plate. (Wright et al., 2023a).

Figure 5.9 shows CAD models for the three main body sections (head, body and tail fin). All presented parts are 3D printed except for the tail fin plate. Electronic components are installed and accessed via the flange connection between the joint enclosure and the electronics compartment. The interface is watertight sealed via 8xM3 screws and a surface seal made of expanded DA320 closed cell sponge material.

5.5 Buoyancy and balance adjustment

To achieve optimal swimming, it is important to balance and ballast the robot to ensure it has right amount of buoyancy and swims stably in an upright position as well as to reduce static and dynamic instabilities. Modules are balanced and ballasted individually to allow for flexible configuration to extend or reduce the number of robot

body modules. Individual module buoyancy adjustment and ballasting is also important to reduce any undesired roll motion when the central line curves during manoeuvring. All module structures are axisymmetric along X in the X-Y and XZ plane (see Figure 5.10). Static components are placed to ensure a centre of gravity point below the centre of buoyancy to enhance static stability in an upright position. The buoyancy force and centre of mass of each module are Y asymmetric in YX plane, due to the module shape having a lower volume and greater mass towards the joint side. Added weight is needed to make it possible to align the centre of mass and centre of buoyancy for each module.

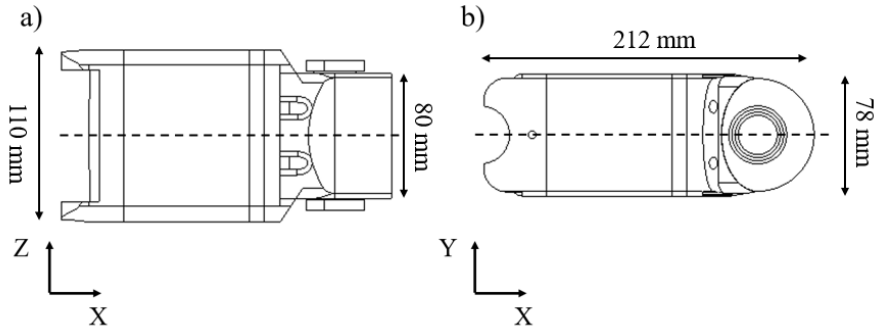

Figure 5.10 a) Z- axis symmetry b) X-axis symmetry. (Wright et al., 2023a).

The overall dimensioning of the body volume during the design process, taking Archimedes principle into consideration, resulted in only low amounts of ballast being required. Final balancing and ballasting are achieved together by adding weights at the bottom of each module. As a result, the robot is submerged along the free surface of water and a stable horizontal floating position of the assembled robot is achieved.

5.6 Key challenges experienced during design and building process

Fundamental yet most challenging to the design process was the watertightness of the 3D printed enclosures. Early in the design process the choice was made to move from FDM to SLA 3D printing as it provided a waterproof structure. Because of the magnetic coupling, only static interfaces to access the module housed electronics for assembly and maintenance need to be designed. During the design process and supported by the ability to fast prototype using 3D printing, radial and face seal arrangement were investigated. Radial seals provide the benefit of an increasing

sealing force the higher the external pressure, however, they require high tolerances and are difficult to achieve using the applied additive manufacturing techniques.

The final design includes a face seal suitable to be produced using the chosen 3D printing techniques and the sealing pressure can be adjusted via 8 screws. Most important to the designed water seal is a soft sealing material. Most common nitrile O-ring materials are rather hard and did not achieve reliable water tightness. The final face seal is made up of a soft closed foam material.

A further challenge was using Bluetooth Low Energy in an underwater application. A simple test consisting of a bucket of water and a waterproof Tupperware food container to submerge an Arduino microcontroller provided sufficient evidence for acceptable performance at low water depths.

For the robot to swim just below the water surface, each module was ballasted individually. Initially, the ballast weight was to be placed inside the module, however, limited space, however, limited space, rapid movements during undulation and the need to open the static seal each time an adjustment is made lead to the decision to attach the ballasting weight to the outside at the bottom of each module. This setup increases the drag, so that future systems are planned to have a more sophisticated and actuated method of blasting.

5.7 Conclusion Chapter 5 Design and development of bio-inspired autonomous underwater vehicle

Creating and testing bio-inspired underwater vehicle prototypes represents a key part of the effort to understand and apply bio-inspired locomotion. Testing of prototypes and experimental research provide proof of feasibility and validation data for CFD simulations. Amongst the vast number of ingenious designs, modular bio-inspired eel or snakelike robots represent a versatile platform able to exceed the performances of conventional designs.

A common challenge faced by bio-inspired mechanical designs is the integration of body flexibility. In the case of modular snake-eel like robots, the majority of designs rely on O-rings and flexible covers to waterproof the actuated connection between

modules. Both solutions provide insufficient ingress protection at large water depths and rough open sea conditions. This is mainly due to degradation from wear and tear, required engineering tolerances and insufficient protection against increasing water pressure at greater depths. Further, both solutions limit modularity due to challenges when needing to access, replace and repair modules. A new and fully modular design is presented based on the novel application of a synchronous magnetic coupling. The prototype achieves statically sealed watertightness and true mechanical modularity by avoiding a fixed mechanical coupling between neighbouring modules. The magnetic torque transfer without fixed mechanical connections offers a reduced weight structure and protective decoupling under extreme load. The final presented design avoids using a fixed mechanical connection, which facilitates disconnection under high load, and increases the survivability of the robot in harsh environments. Analytical and numerical simulations are conducted to design and optimise the strength of the magnetic coupling. The strong but breakable connection offers a pathway to future development of underwater robots as can be observed in space robotics, namely the use of self-configurable modular robotic technologies (Letier et al., 2019). Future development towards self-configuration and adaptation to the environment will be enabled by adding an actuated decoupling mechanism to the current permanent magnet connection.

Two different types of additive manufacturing are used and discussed, namely Fuse Deposition Modelling (FDM) and Stereo Lithography STL). The final, second iteration prototype is created using SLA and the parts are optimised for this printing technique. Each module houses an identical set of electronics. Wireless open loop control is achieved via a Bluetooth Low Energy (BLE) connection between each module and a laptop as the central node. Bluetooth was selected as a low-cost solution, however, this restricts the swimmer to swimming close to the water surface. The Bluetooth connection is further used to send and record power data of each module on the laptop. The structure consisting of a head module, repeating body modules and a tail fin may have a variable number of body modules. The head module is identical to a body module apart from a forward-facing clear screen to allow, for example, a camera to point in a forward direction. The tail fin module uses the same joint connection as the other modules and the fin plate can easily be replaced to, for

example, test different materials. The tail fin itself does not provide significant buoyancy. While body modules are balanced individually, the tail and head modules are balanced in combination so that the overall robot lays flat just below the water surface.

The final created design represents the best combination of available and created parts as determined by the author. Through the iterative process numerous combinations and changes have been made, such as changing the shape and function of the 3D printed parts, such as changing the assembly order or water-sealing surface. The design process was concluded after a balance between all general requirements where found. Such general requirements include dimensioning for optimal water tightness, access to and assembly of the modules, sufficient buoyancy, low-drag shape optimisation as well as maintaining the ability to 3D print the part with the available printer.

Selection of components, such as equipment for electronic, communications and control, was determined based on required functionality and guided by price, dimension and compatibility considerations.

Chapter 6 Hydrodynamic lab testing of modular magnetic bio-inspired underwater vehicle

In the following, results are presented that test and confirm the ability of the robot to generate thrust and swim freely. A custom-built reversed bollard test is constructed to measure the force at the leading edge resulting from body undulation with different amplitude envelopes and magnitudes, frequencies and tail plate stiffnesses.

A state-of-the-art optical motion tracking system from Qualisys AB is used to measure the swimming trajectory of the robot. Applying this technique, a study is conducted to investigate the maximum swimming speed for varying kinematic parameters. Parts of this Section are published in (Wright et al., 2023a).

6.1 Facility, robot configuration and lab setup

All lab tests are conducted at the Kelvin Hydrodynamics Laboratory at the University of Strathclyde. The laboratory has two water tanks, a towing tank and a wave tank.

The towing tank is 76x4.6x3 m (LxWxD). The wave tank is 9x3.15x1 m (LxWxD). All tests are conducted in still water conditions and the robot ballasted to remain submerged just below the water surface to maintain BLE communication.

(a)

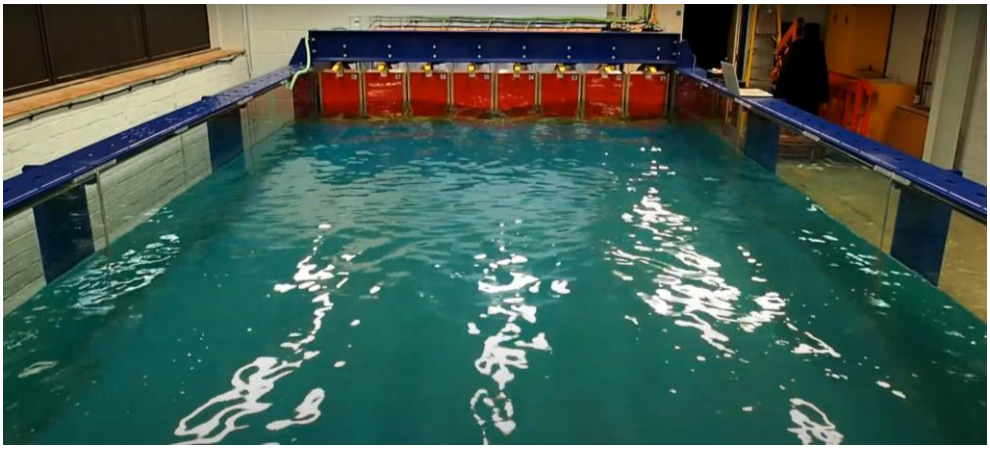

(b)

Figure 6.1 Kelvin Hydrodynamic (a) towing tank (b) wave tank.

The robot configuration used in the tests consists of a head module, two body modules and a tail module with a total length of 907x70 x110 mm (LxWxH). The tested robot configuration is shown in Figure 6.2. The joint positions along the robot body, starting from the leading edge of the head module are $s_1 = 248$ mm, $s_2 = 444$ mm and $s_3 = 642$ mm.

The robot followed kinematics described by Equation 3.30 where the kinematic parameters, including $A(s)$, $C(s)$, $\varphi(s)$, f, c_a and c_s, are controlled through user input in MATLAB. Communication between the software and the robot is achieved using Bluetooth between a laptop and an Arduino Nano microcontroller installed in each body module.

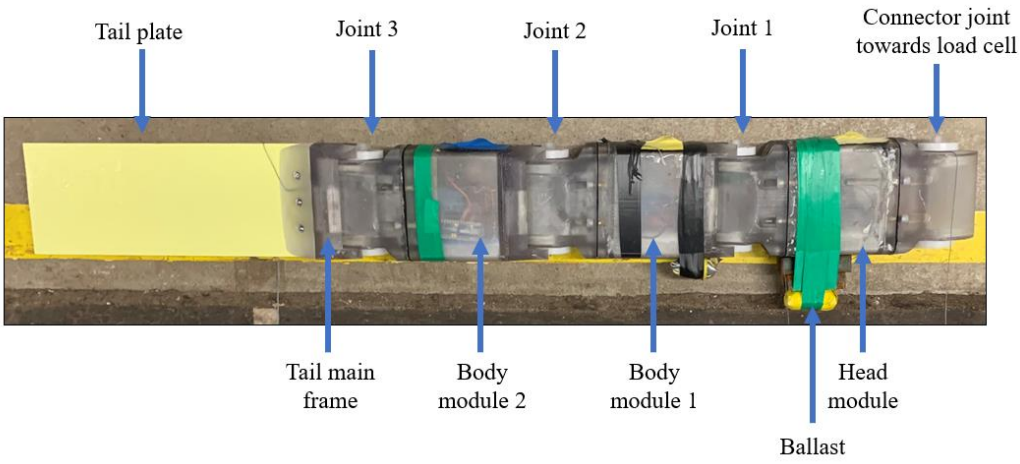

Figure 6.2 Robot configuration during lab tests. (Wright et al., 2023a).

6.2 Experimental thrust measurements

Thrust generation through body undulation is a fundamental design feature of the presented robot. As discussed in Section 2.2, currently available hydrodynamic efficiency coefficients, such as the Froude efficiency, are not suitable to assess the swimming performance of fish, as the useful energy of fish propulsion is not clearly definable. To measure the robot generated thrust, a test methodology resembling the bollard pull test is conducted. A comparable test setup was applied in Struebig et al. (2020).

To take account of the undulation propulsion dynamics and periodic thrust generation, the swimmer is configured to exert a force by pushing against a load cell rather than exerting force by pulling on a line away from a fixed position. This modification aims to optimise the application of the methodology for a more effective and accurate assessment of the undulation propulsion dynamics.

6.2.1 Setup and calibration

The force measurement apparatus consists of an aluminium bar lowered lengthwise into the water with the robot connected to it at the lower end. The aluminium bar is fitted with 4 strain gauges positioned to, from the perspective of the robot, measure the force applied in both normal and lateral directions. In fact, the attached strain gauges measure the beams bending moment, but the readings are calibrated to measure

force. The robot is connected through a 3D printed adapter fixing the robot head to the aluminium bar. The connection allows one rotational degree of freedom to account for the wave motion of the robot to start at the leading edge. Figure 6.3 shows the setup and the three main components 1) strain gauge bar 2) adapter facing towards the strain gauge bar 3) robot.

The setup is calibrated to determine the conversion factor between the measured change in voltage of the strain gauges and the magnitude of applied forces. Here, the setup is loaded with defined weights and the measured voltage is recorded. Figure 6.4 (a) shows the linear relationship between the added weights and the corresponding measured voltage. The slope, in other words, the conversion factor is found to be 0.0882 volts per newton. In the second step, to validate the conversion factor, it is used to directly measure the applied load. Figure 6.4 (b) shows the error between the added and applied measured load in %.

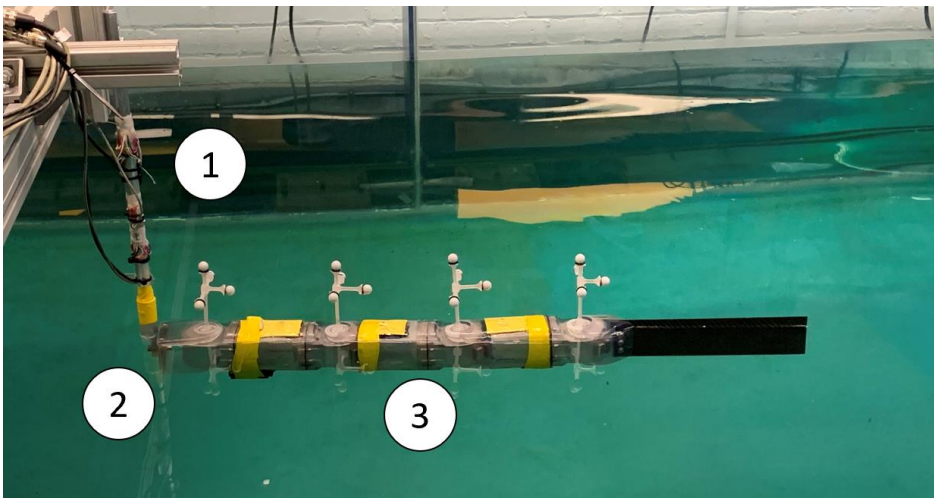

Figure 6.3 Robot thrust test (1) strain gauge bar (2) adapter (3) robot. (Wright et al., 2023a).

The measured thrust data is post-processed via a lowpass filter to cut out frequencies above 2.5 times the actuation frequency. Figure 6.5 shows an example set of results with highlighted sampling points and a low-pass filtered signal. For equal measurements between cases and to ensure perpendicular alignment of the robot towards the strain gauge bar, forward force sample data is taken at the point where the side force sample data over one oscillation cycle $T = 1/f$ is closest to zero $\frac{1}{T}\sum F_y \approx 0$. At this point instantaneous force curves are compared, and the net thrust is recorded.

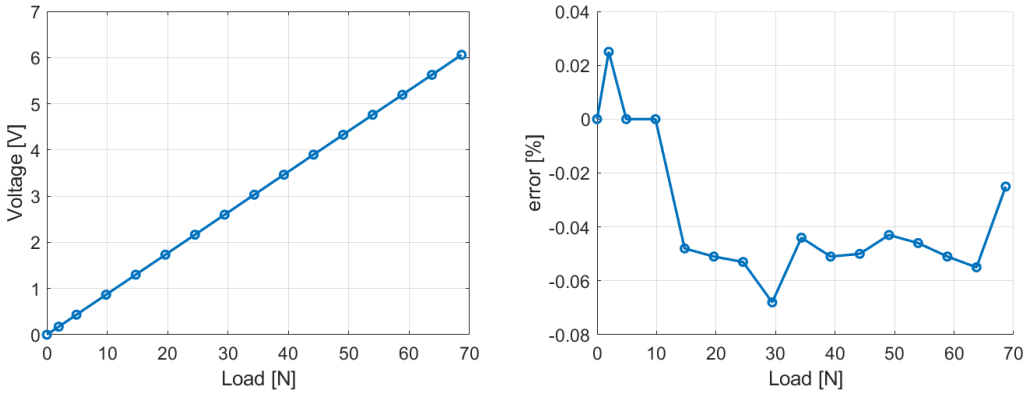

(a) (b)

Figure 6.4 (a) Calibration voltage measurements for added load and (b) error per cent between added and measured load using found conversation factor.

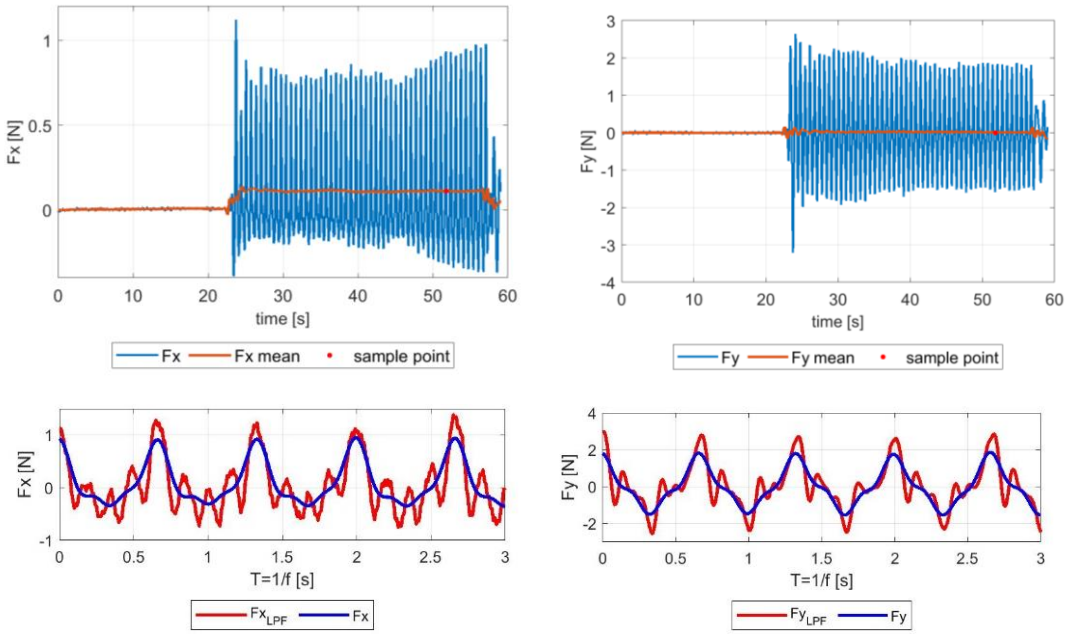

(a) (b)

Figure 6.5 Sample results showing type of captured results and application of lo-fi filter: (a) thrust force and instantaneous force with a low-pass filter, (b) side force and instantaneous force with a low-pass filter. (Wright et al., 2023a)

6.2.2 Investigated parameters

Recorded data is compared for different frequencies, amplitudes and fin materials. Results are obtained using a constant amplitude envelope, $A(s) = c_a$. The wavelength is maintained at $\lambda = 2\pi$. To assess the thrust performance and support future design decisions on the flexibility of the tail fin, three different caudal fin materials (single sided carbon fibre, Foamex and High Impact Polystyrene (HIPS)) are investigated at

two amplitude and two frequency values. A test matrix of all parameters is shown in Table 6-1.

Table 6-1 Reversed bollard test case parameter

	Material	f [Hz]	c_a [-]
Case 1	Carbon fibre	1	10
Case 2	Carbon fibre	1	15
Case 3	Carbon fibre	1.5	10
Case 4	Carbon fibre	1.5	15
Case 5	Foamex	1	10
Case 6	Foamex	1	15
Case 7	Foamex	1.5	10
Case 8	Foamex	1.5	15
Case 9	HIPS	1	10
Case 10	HIPS	1	15
Case 11	HIPS	1.5	10
Case 12	HIPS	1.5	15

All three tail plates are 1 mm thick and are of the dimensions shown in Figure 6.6. The tail material properties are in agreement with the general material properties available in the MatWeb database (MatWeb, 2023). The robot is controlled using open loop real-time serial communications through MATLAB Simulink (MathWorks Inc., 2023).

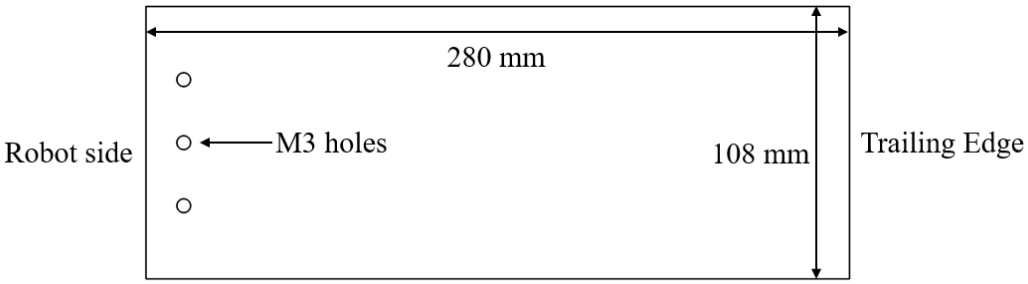

Figure 6.6 Exchangeable tail plate dimensions. (Wright et al., 2023a).

6.2.3 Results and discussion

6.2.3.1 The influence of actuation frequency

Figure 6.7 (a) shows an overview of the measured net thrust comparing cases of constant amplitude and material and frequency variation. For all cases, an increase in wave frequency results in an increase in net thrust. While the increase is marginal for case pairs 6-8, the difference between case pairs 2-4 increases twentyfold. As expected, an increase in wave frequency led to an increase in instantaneous force

frequency in all cases. The instantaneous forces of case pairs 9-11, Figure 6.7 (b), show that the side force remains stable in magnitude for increasing frequency while the net thrust force increases.

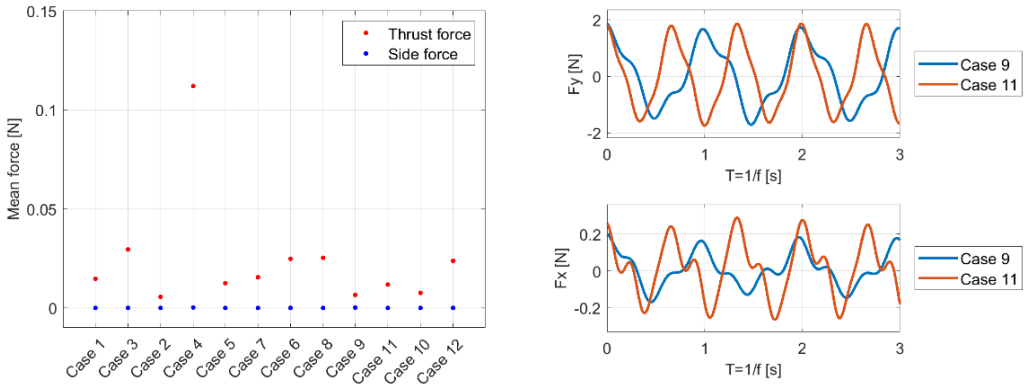

(a) (b)

Figure 6.7 (a) comparison of case pairs for increased frequency
(b) instantaneous force comparison of case pairs 9-11. (Wright et al., 2023a).

6.2.3.2 The influence of actuation amplitude

Figure 6.8 (a) provides an overview of a comparison of the measured net thrust and case pairs in relation to changes in undulation amplitude. An increase in amplitude results in an increase in net thrust, in all but one case. Further, an increase in amplitude led in all cases to an increase in the observed side force which can be seen in the comparison of the instantaneous forces of case pairs 3-4 in Figure 6.8 (b). While the general force curves show a resemblance to one another, the amplitude of side and thrust forces increase in line with the increase of actuation amplitude.

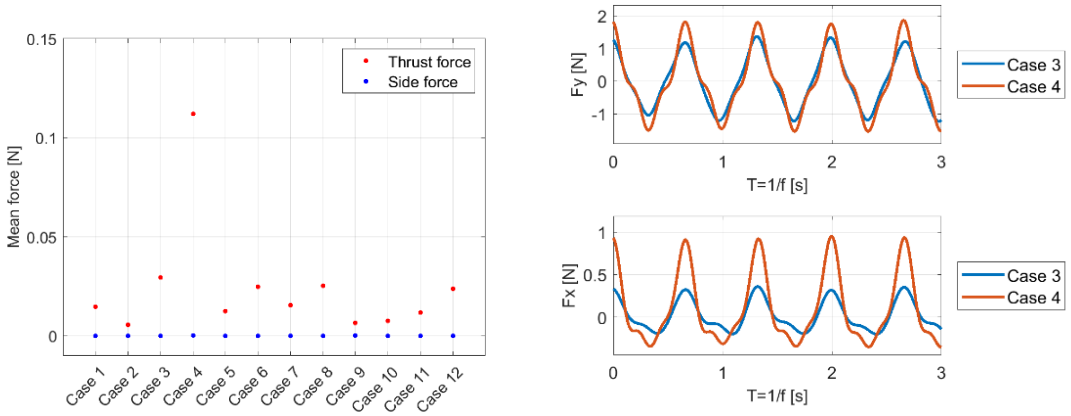

(a) (b)

Figure 6.8 (a) comparison of case pairs for increasing amplitude
(b) instantaneous force comparison of case pairs 3-4. (Wright et al., 2023a).

Strikingly, Case 4 achieves the highest mean forward force. Mean force calculations are consistent with the instantaneous curve, see Figure 6.8 (b). Potential reason for the significant increase in mean thrust may be due to optimal hydrodynamics or resonance frequency effects for the selected kinematic parameters.

6.2.3.3 Variation of caudal fin stiffness

The difference in material stiffness leads to a different elastic displacement due to the fluid surface pressure. Figure 6.9 shows the deformation over one oscillation cycle $T = 1/f$ of the Foamex material in case 4. Clearly visible is the formation of vortices.

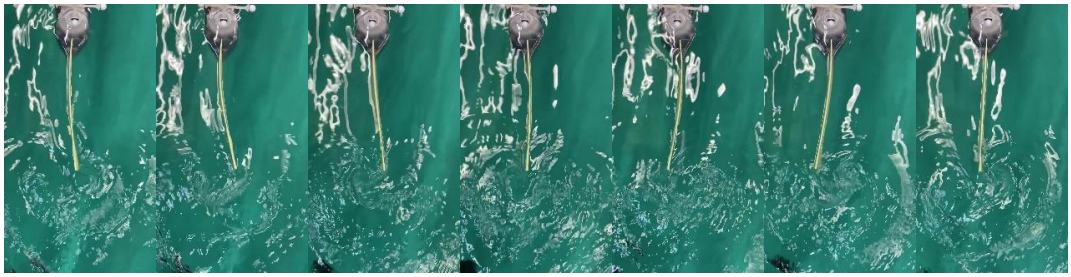

Figure 6.9 Elastic displacement of Foamex tail plate. (Wright et al., 2023a).

A comparison of the three caudal fin materials shows differences in the force magnitude as well as differences in elastic displacement wave shape. A comparison of the mean thrust in Figure 6.10 does not reveal a clear advantage for any of the three materials for the tested geometries. However, a trend towards improved thrust performance with increased stiffness is visible which may be explained by unfavourable elastic displacement of the less rigid materials.

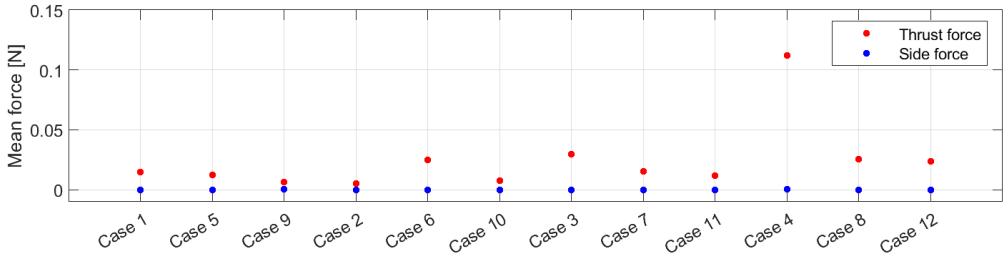

Figure 6.10 Overview of net thrust between case pairs of different materials at a constant amplitude and frequency. (Wright et al., 2023a).

Figure 6.11 to Figure 6.14 present the instantaneous force curves of all cases. The figures are arranged to compare the performance of the three materials at varying frequency and amplitude.

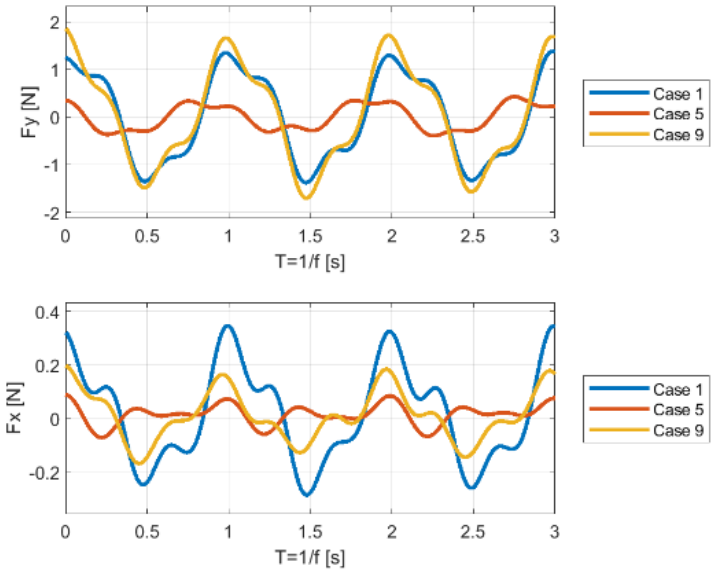

Figure 6.11 $c_a = 10, f = 1$. (Wright et al., 2023a).

In terms of optimal curve progression, ideally the sinusoidal undulation motion translates into smooth sinusoidal force curves, where the cycle mean side force is zero and the cycle mean normal force is positive. Force curves of Figure 6.11 and Figure 6.12 differ in actuation amplitude and are equal in actuation frequency. The resulting side force curves are significantly smoother for the higher amplitude. Potential reasons may include resonance effects, and improved fluid structure interaction at the selected parameters.

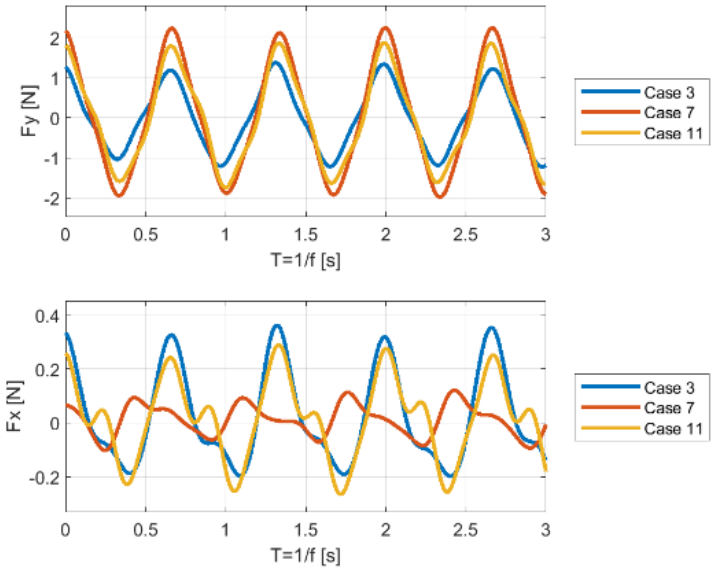

Figure 6.12 $c_a = 15, f = 1$. (Wright et al., 2023a).

However, the normal force for both amplitudes shows strong fluctuation suggesting non-smooth acceleration. Out of all amplitude and frequency parameter combinations Figure 6.14 records the smoothest curves in lateral and normal force directions.

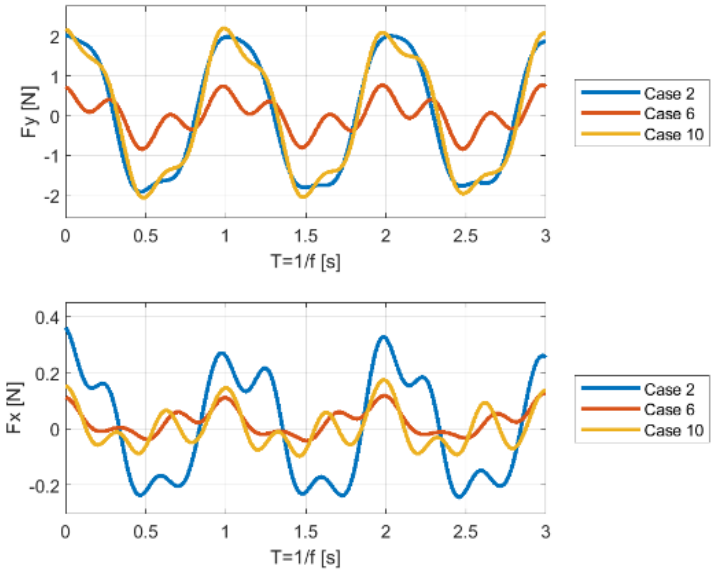

Figure 6.13 $c_a = 10, f = 1.5$. (Wright et al., 2023a).

Non-smooth force recording, in for example Figure 6.13, show no resemblance with the input actuation parameters, further suggesting complex fluid structure interaction and non-smooth elastic deformation of the tail fin. In contrast, smooth recordings, in for example Figure 6.14, show good agreement of the force peaks according to the actuation frequency.

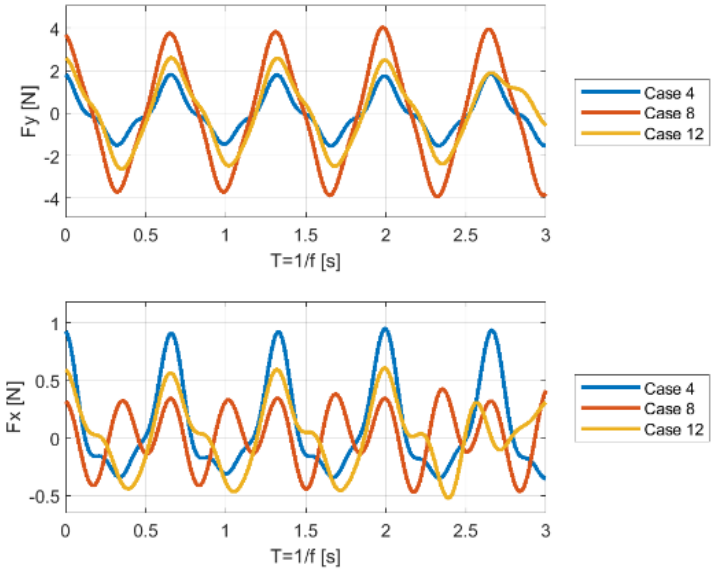

Figure 6.14 $c_a = 15, f = 1.5$. (Wright et al., 2023a).

Ideally, the elastic caudal fin extends the main body's undulation shape and allows for smooth vortex shedding. Results show that the actuation amplitude frequency and stiffness have a strong influence on the swimming stability as well as thrust generation.

6.2.1 Conclusion on experimental thrust measurements

Extensive lab testing was conducted to test and assess the basic functions and performances of the robot protype. All tests are conducted in a lab environment at the Kelvin Hydrodynamics Laboratory (KHL) at the University of Strathclyde over a number of days, however, each of the presented data sets are recorded in a single day to reduce inconsistencies between data points. The KHL has two water tanks, a large towing tank measuring 76x4.6x3 m (LxWxD) and a smaller size wave tank measuring 9x3.15x1 m (LxWxD); both are used to test the prototype robot.

The tested robot configuration consists of a head and tail module and 2 body modules, resulting in a total swimmer length of 907 mm with the joints located at 248 mm, 444 mm and 652 mm along the body.

Thrust generation is a fundamental function of the created prototype. The efficiency at which the electric energy stored within the batteries is converted to kinematic energy is highly variable and influenced by the tail fin material and kinematic parameters. Therefore, a test apparatus is created to perform experimental measurements of the created forward force for a variation of tail fin materials and body kinematics.

The experimental tests analyse three different tail plate materials, representing a hard, medium and soft material, the undulation wave frequencies are $f = 1\ Hz$ and $f = 1.5\ Hz$, and the undulation wave amplitudes are $c_a = 10$ and $c_a = 15$. The resulting total number of investigated cases is 12.

The created apparatus resembles a reversed bollard test. The custom-made test setup consists of an aluminium bar fitted with load cells in a particular arrangement to measure the forward and side forces, from the perspective of the robot. The robot is positioned in the water to push against the bar. Here, the robot head is fixed to the bar via a 3D printed adapter allowing for a single rotational degree of freedom. The setup is calibrated to convert the strain gauge voltage to a force value. Calibration results

confirm the accuracy and tolerance of the setup. Post processing of the acquired data ensures that the forward force measurements are taken when the cycle mean side force is equal to zero. This ensures a perpendicular position of the robot towards the strain gauge bar. Recorded data is processed through a low-pass filter, to cut out all frequencies above 2.5 times the actuation frequencies.

Results confirm findings of previous studies in literature that the frequency is a suitable control variable to adjust the forward swimming speed. For a constant tail fin material and wave amplitude, an increasing frequency leads to increasing thrust generation. This was found to be also true when the amplitude is varied in all but one case. In other words, for a constant frequency and tail material, an increasing amplitude leads to increasing thrust generation. Results of tests of different tail fin materials indicate a varying level of complexity of the fluid structure interaction. In some cases, the measured wave form represents low fluctuation between crest and trough, while others show high fluctuation which is not removed by the low-pass filter. A general trend towards improved thrust generation for higher tail fin stiffness is observed.

6.3 Experimental free-swimming measurements

Unrestricted swimming tests make it possible to observe the stability of the highly dynamic system and provide first insights into the overall swimming performance including manoeuvrability and swimming speed. All free-swimming tests are presented for the setup described in Section 5.1 with a Foamex caudal fin. The presented results validate the ability of the robot to swim and manoeuvre, in other words, controlled change of swimming direction.

6.3.1 Setup and calibration

Qualisys is a vision-based system that senses the motion of reflective markers mounted on top of the robot. The setup consists of at least two cameras to sense 3DoF linear motion sensing and three cameras to sense 6DoF motion sensing including rotation. Figure 6.15 shows a schematic of a three-camera setup above the water tank and the cameras common field of view area on the water surface. The accuracy of the detection is 0.01 mm, and the sample rate is set to 300 Hz.

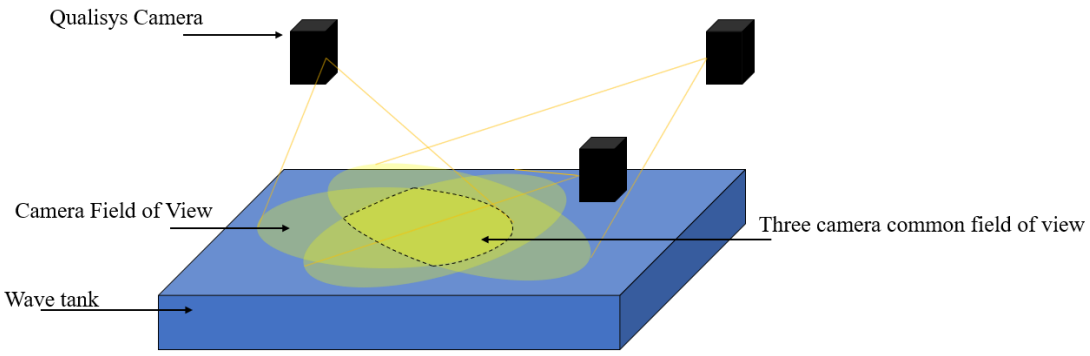

Figure 6.15 Schematic of motion capturing setup around water tank.

Four 3D printed “tree” structures, each with four reflective markers, are mounted on the top of the swimmer. Two different size reflective ball diameters are used; 1 cm diameter shown in Figure 6.16 and 3 cm diameter shown in Figure 6.19. The bigger reflective ball diameter improved detection over larger distances and area. Prior to testing, the Qualisys system is calibrated using a calibration probe of known size and defined marker spacing.

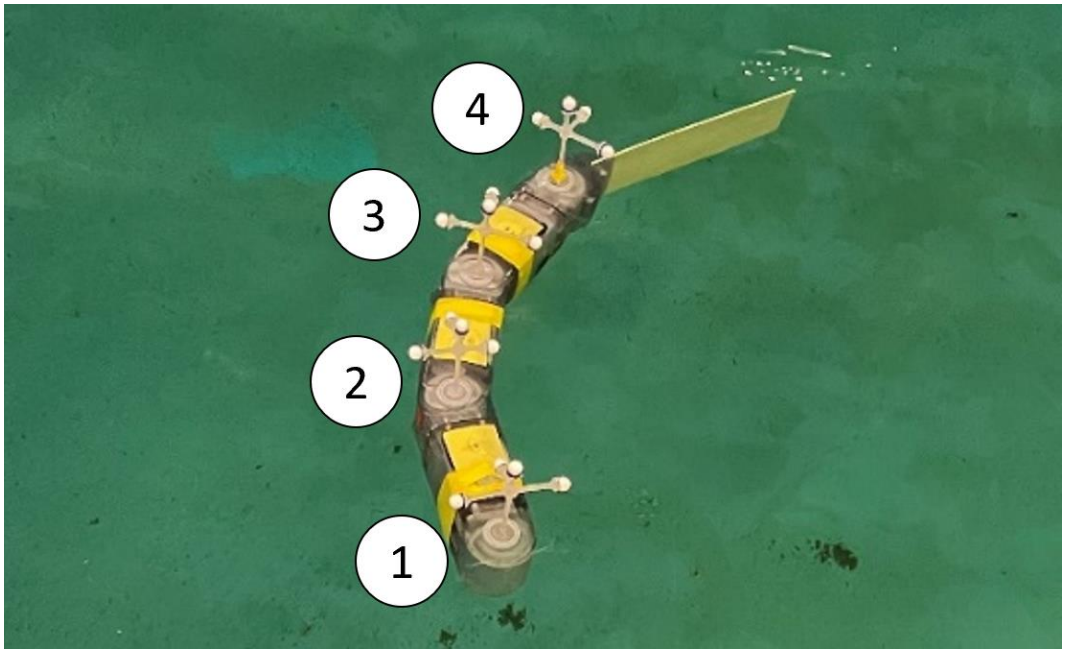

Figure 6.16 Curved MMBAUV in water with four reflective markers. (Wright et al., 2023a).

6.3.2 Investigated parameters

The presented free-swimming manoeuvring and turning tests provide a first result of the minimum turning radius. A parametric study is conducted to measure the velocity

for the straight swimming robot with an attached Foamex tail plate. Equal servo input amplitudes are varied between 30 to 70 degrees in steps of 10 degrees, translating to joint amplitudes of 11.25, 15, 18.75, 22.5 and 26.25 degrees, and actuation frequencies of 0.4 Hz, 0.6 Hz and 0.8 Hz. Higher frequencies are representable by the protypes hardware; however, observations have shown high roll instabilities when undulating at higher frequencies, which leads to difficulties in motion capturing and wireless data transmission. Table 5-2 provides an overview of all tested cases.

Table 6-2 Overview of free-swimming velocity parameters

	$c_a = 30$	$c_a = 40$	$c_a = 50$	$c_a = 60$	$c_a = 70$
$f = 0.4\,Hz$	Setup 1	Setup 2	Setup 3	Setup 4	Setup 5
$f = 0.6\,Hz$	Setup 6	Setup 7	Setup 8	Setup 9	Setup 10
$f = 0.8\,Hz$	Setup 11	Setup 12	Setup 13	Setup 14	Setup 15

6.3.3 Results and discussion

6.3.3.1 Turning

BCF swimmers manoeuvre by curving their central line, as numerically investigated in Section 4.1. Basic lab tests have confirmed the ability of the robot to curve and generate thrust. Presented manoeuvring lab test results took place before the numerical investigation and, therefore, do not follow up on the findings of Section 4.1. Experimental validation is planned for the future.

Importantly, body curvature moves the centre of mass of the robot. Curving leads to a slight tilt angle towards the inner curved side. Individual balancing and ballasting of each module, in comparison to balancing and ballasting the whole robot configuration, reduces the extent the robot leans to one side to maintain a stable position in the plane.

To reduce the influence of waves reflecting back off of the walls, the robot is positioned at the centre of the common camera area and the water is given time to calm before setting the robot in motion. Stable swimming performances for curved swimming trajectories throughout the whole capture area is achieved. Figure 6.17 shows the trajectory of the four attached reflective markers. The data is recorded with

a constant amplitude envelope at $c_a = 10$, equal joint offset of $c_s = 70$ and a frequency of $f = 1\ Hz$.

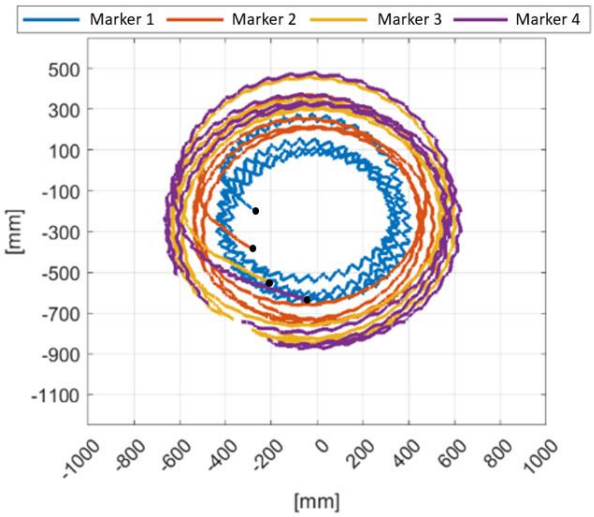

Figure 6.17 Cambered robot body circle trajectory. Starting position highlighted by black dots (Wright et al., 2023a).

Starting from a resting position, Figure 6.17**Error! Reference source not found.** shows the robot reaches a stable circular trajectory. The head module follows the smallest radius of circa 300 mm and tail fin joint follows a larger radius of circa 1400mm. Recorded data of roll pitch and yaw is shown in Figure 6.18 and corresponds to the data in Figure 6.17. The dynamic roll and pitch amplitudes are recorded to be circa 2.5 and 2 degrees respectively. Static pitch and roll amplitude are recorded at around 8 and 10 degrees respectively. The time for one full circle is approximately 35 seconds resulting in an angular velocity of 10 degrees per second.

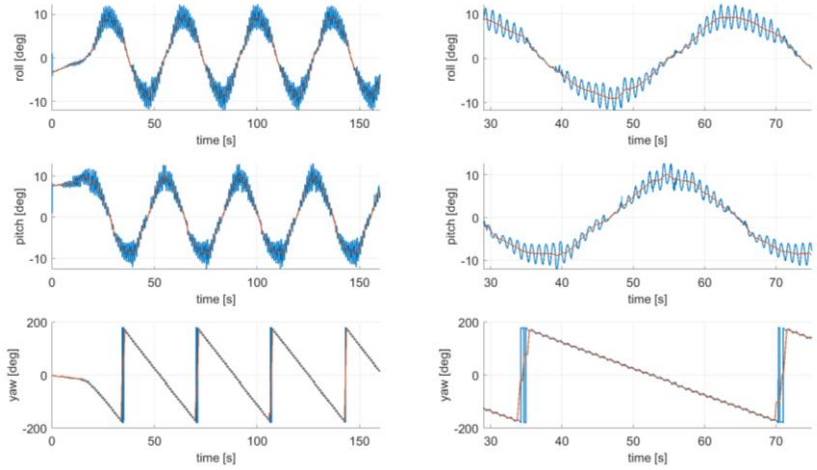

Figure 6.18 Roll, pitch and yaw trajectories of multiple circles (left column) and focus on a single circle (right column). (Wright et al., 2023a).

Figure 6.18 highlights the stable manoeuvring performance by showing the high level of repeatability for each turning circle. Next to the expected repeating yaw angle, which moves between minus and plus 180 degrees, the pitch and roll also show a repeating pattern. Roll and pitch both oscillate between ca. plus and minus 10 degrees. Both signals show a stable phase difference of around 22.5 degrees or one eighth π.

6.3.3.2 Straight swimming velocity tests

As discussed in Section 2.2, determining the efficiency of a self-propelling swimmer remains challenging. The self-propelled swimming velocity is an indicator of the technical ability of the system to transform electric energy into kinetic energy. In the following, a series of measurements are presented to investigate the quasi-steady swimming speed of the robot for different kinematic parameters. Conducted in a towing tank in still water, the robot is positioned at the centre of the tank parallel to the tank walls. Figure 6.19 shows the robot in its initial position. Setting a constant amplitude envelope resulted in reduced roll instability, compared to, for example, a linear amplitude envelope due to the undulation axis symmetry and counter balancing.

Figure 6.19 Photo of robot velocity measurement setup.

Figure 6.20 plots the recorded maximum quasi-steady state mean velocity of each amplitude and frequency combination. Results confirm the trend of the force measurements in Section 6.2 that an increase in amplitude and frequency lead to an increase in swimming velocity. Striking is the near linear relationship between

frequency and velocity. The maximum and minimum measured velocities are 0.5 m/s and 0.03 m/s corresponding to 0.57 and 0.03 body lengths per second.

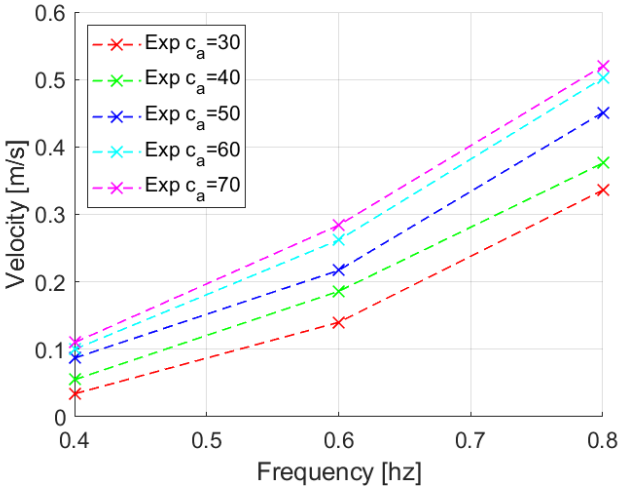

Figure 6.20 Overview of experimentally measured cycle-averaged maximum swimming velocities.

Joint yaw actuation also resulted in recorded periodic pitch and roll motion. Figure 6.21 shows an overlay of the recorded yaw and roll occurring at frequency 0.6 Hz and joint input amplitudes of 30 and 40 degrees. After a transition period, yaw and roll progress with constant amplitude and frequency. Results show the roll frequency $f_{roll} = \frac{1}{T_{roll}} \approx 0.6\ Hz$ is equal to the yaw actuation frequency and an increasing yaw amplitude leads to an increasing roll amplitude. A minor offset of the recorded roll motion may be explained by small imperfections of the ballasting as well as inaccuracies of the zero position of the joints due to the timing belt gear spacing.

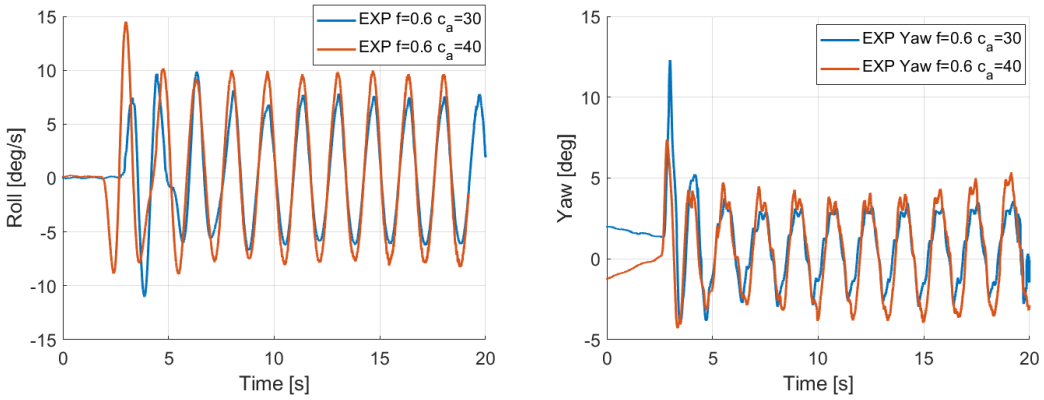

(a) (b)

Figure 6.21 Comparison of experimental data of 0.6 Hz and $c_a = 30$ and $c_a = 40$ (a) instantaneous yaw and (b) instantaneous roll.

As shown in Figure 6.22, both setups show a similar progress of forward average velocity. Following similar initial acceleration, both show a drop after two full body undulations, after approximately five seconds, followed by a subsequent velocity increase. The measured maximum velocity, sampled at 19 seconds, is 140 mm/s and 186 mm/s.

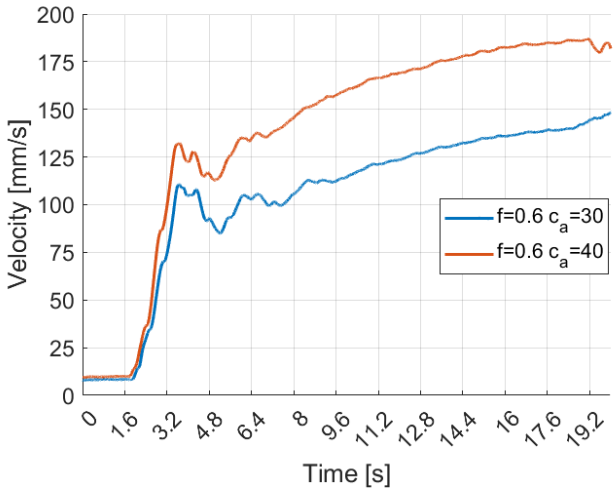

Figure 6.22 Average forward velocity of two experimental measurements.

6.3.4 Conclusion on experimental free-swimming measurements

A great deal of effort has been put into creating an untethered prototype to achieve unrestricted swimming motion. Free-swimming motion is recorded through a motion capturing system from Qualisys AB. The setup sees a number of cameras, focused on a common area, able to detect reflective markers attached to the robot. Through calibration and detection of the reflective markers at a defined distance it is possible to reconstruct the 6DoF and 3D position and motion of the robot. It is possible to derive the displacement velocity and acceleration data based on the discrete trajectory data.

Fast motion and wide recording angles provide challenges to taking measurements and at times led to failure of detection and subsequent loss of data. However, it is possible to interpolate data points to fill minor gaps in data. Results of a turning manoeuvre are presented for a fixed amplitude, offset and frequency. The body curvature of the robot leads a changing heading direction, vectoring of mean thrust, a resulting moment and a stable turning trajectory. The achieved minimum turning radius of the head is 300

mm, equal to one third of the body length. Recordings of pitch and roll reflect the periodicity of the undulation motion.

The free-swimming forward speed is measured for a range of undulation amplitudes and frequencies. The tests aim to provide insight into the ability of the system to convert electrical energy into kinetic energy as an indicator of the efficiency. The experimental parametric study is conducted for a range of undulation amplitudes and frequencies at a constant amplitude envelope and wavelength of 2π. All tests are conducted using the Foamex tail plate. The free-swimming tests confirm that the frequency and amplitude are suitable control variables to regulate the swimming speed of the robot. Increases in frequency lead to a near linear increase in swimming speed for all tested amplitudes.

6DoF motion tracking confirmed the robot undulating at input frequency. Recordings show that the robot periodically moves in roll equal to the undulation frequency and that an increase in undulation amplitude leads to an increase in roll amplitude.

A comparison of the mean forward speed for two amplitudes at equal frequency shows a steep acceleration and subsequent deceleration followed by a slow climb towards final velocity. The stark acceleration aligns with the first full body undulation sweep.

Overall, the free-swimming tests highlight the functionality of the created system and potential for efficient, agile and manoeuvrable swimming.

6.4 Comparison of experimental and numerical model

Numerical models enable virtual testing of physical systems. Models may be limited by simplifying assumptions to reduce computational expense, a lack of available data and understanding of physical phenomena or unknown system dynamics. Developing accurate numerical models remains a key challenge and is increasingly difficult for complex systems. The bio-inspired robot prototype represents such a complex system.

In the following, a comparison is attempted between the numerical model described in Section 3.2.3 and experimental free-swimming results presented in Section 6.3.3.2.

6.4.1 Setup

A CFD multi-body simulation, applying the model described in Section 3.2.3, is setup to resemble the experimental setup in 6.3.3.2. The setup uses an identical solver setup as presented in Section 5.3. Figure 6.23 shows the created robot geometry as a 2D cross section within an 18x4.6 m (LxW) mesh domain. The unstructured mesh is setup with an increased mesh density zone around the robot and its forward path. The size of the mesh at the swimmer boundary is $\Delta_{xy} = \frac{1}{333}$ m and increases to $\Delta_{xy} = \frac{1}{33}$ m in the far field, resulting in 32011 total mesh nodes. The time step is set to $\Delta t_s = 0.001$ seconds.

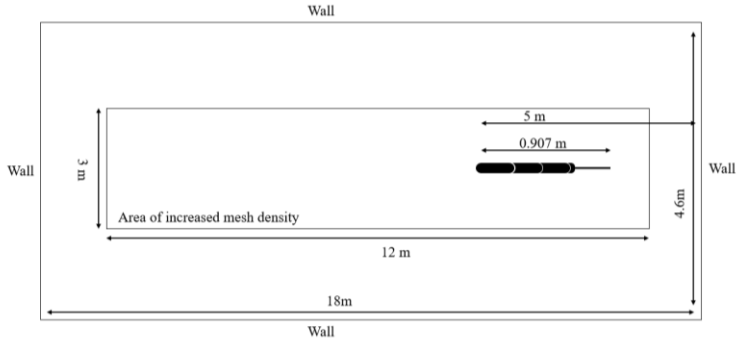

(a)

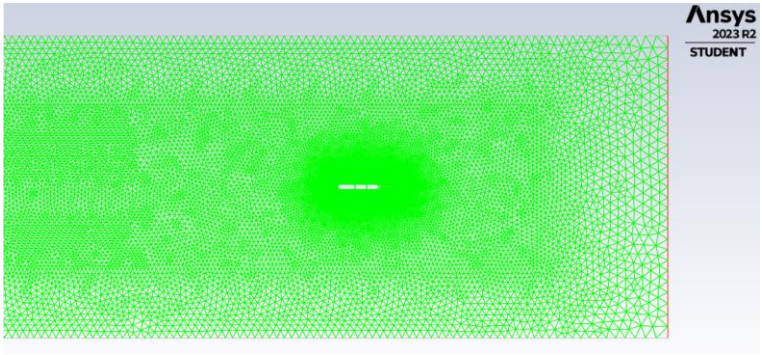

(b)

Figure 6.23 (a) Schematic of CFD domain setup (b) meshed domain.

6.4.2 Comparison results and discussion

Figure 6.24 plots the error of the quasi-steady state cycle-averaged velocity between CFD and experimental data as a percentage change and absolute error. An overall match can be considered poor for the frequencies 0.4 Hz and 0.8 Hz but be seen as improved for the frequency 0.6 Hz. A linear trend is visible with the best prediction

around the medium frequency of 0.6 Hz. Noticeably similar is the error for different actuation frequencies, which may suggest a common source of error. The largest negative absolute error remains below 0.1 m/s and the largest positive absolute error is just below 0.15 m/s.

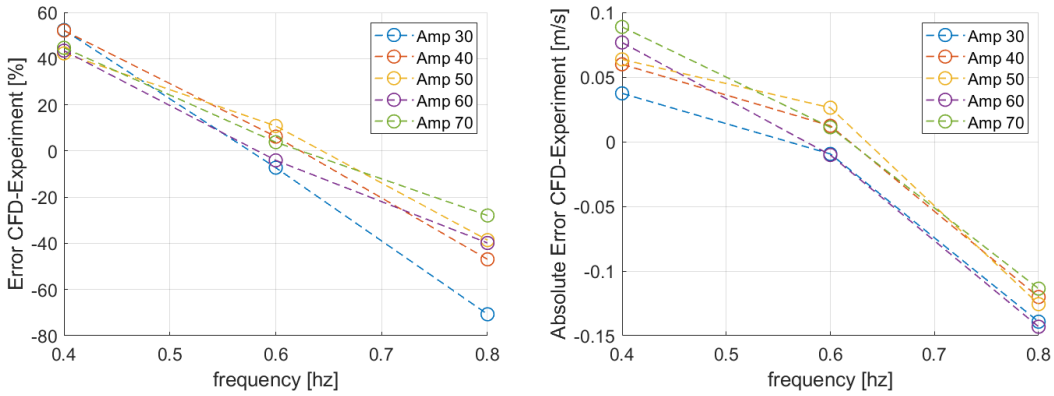

(a) (b)

Figure 6.24 Quasi-steady state velocity error between CFD and experimental data (a) in percent and (b) absolute error in meters per second.

Figure 6.25 (a) shows a comparison of experimental and numerical data of the lateral velocity for setup 6 of Table 6-2, $f = 0.6\ Hz$ and $c_a = 30$. Both curves show a high degree of agreement where the actuation frequency is noticeably visible in the periodicity of both signals. Figure 6.25 (b) shows a comparison of the forward velocity of the same setup where the experimental results reach an overall higher velocity. The forward velocity curves do not match as well as the lateral velocity curves in absolute values and in progression.

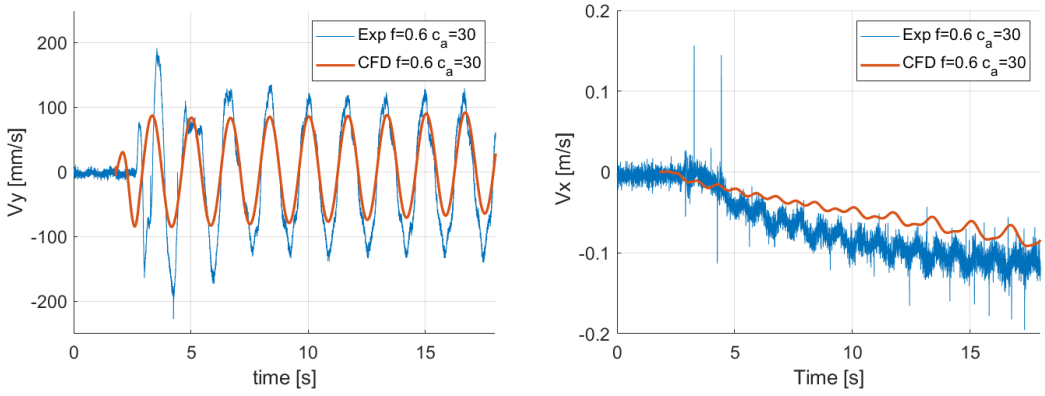

(a) (b)

Figure 6.25 Comparison of experimental and numerical instantaneous velocity for frequency f = 0.6 Hz and c_a =30 in (a) lateral and (b) normal direction.

The conducted CFD simulations are two dimensional to reduce computational time and resources. In contrast, the real robot is allowed unrestricted motion in three dimensions. Energy conservation leads to the CFD model assumption that all input energy remains within a 2D plane and neglects, for example, roll motion depicted in Figure 6.21(a). Roll may appear due to a non-neutral position of the centre of mass. During experiments, a low centre of mass is desirable as it will create a restoring torque to keep the robot upright and reduce roll.

Typically for a numerical simulation, the CFD model uses a simplified geometry and a non-slip wall boundary condition. However, the robot is subject to surface roughness and imperfections. Further, for practical reasons added ballast is placed at the bottom of the head enclosure, visible in Figure 6.2, to balance the low buoyancy of the fin module. This results in increased drag. The elasticity of the caudal fin is a further significant factor not taken into consideration.

The CFD simulation does not consider elastic bending experienced by the experimental caudal fin. The general importance of the tail fin was established in a work by Kelasidi (2018). The numerical tests in Section 3.2 and experimental tests in Section 5.2.2.3 have shown that the elasticity of the caudal fin also affects thrust performance.

The CFD model assumes a fully submerged robot at neutral buoyancy, where the density of the robot is equal to the density of the water. In contrast, the experimental robot is required to swim close to the surface of the water to maintain wireless Bluetooth communication, which is implemented to realise a low cost, untethered prototype.

Problems of non-fully submerged objects are categorised as free-surface problems in which both the air and water domains need to be considered. Effects not present in fully submerged objects, such as resistance caused by waves, may occur.

The multi-body algorithm assumes fully compliant joint motion true to the input signal. The synchronous motion of the magnetic joint is proportional to the load angle and the related restoring torque. This results in a phase shift between the drive and the

driven shaft, which may cause the joint to not accurately represent the input signal. Inertia forces, appearing during the rapid rotational direction changes of the periodic oscillation motion may further contribute to a phase difference between load sides, depending on the actuation frequency and amplitude. Nevertheless, Figure 6.25 (a) shows that the frequency of the yaw motion remains true to the input frequency, but the amplitude may differ from the input amplitude. This needs to be confirmed in future experiments where focus needs to be placed on distinguishing between the global yaw motion of the robot and the joint yaw motion.

The robotic prototype represents a complex mechatronic system consisting of various mechanical and electronic components subject to individual efficiencies and potential lag. While the CFD simulation does consider the multi-body nature of the robot, it does not include any consideration of the mechatronic systems, including dynamics relating to the actuators, timing belt or power system.

Every experiment is subject to measurement uncertainty including, but not limited to, model manufacturing accuracy, sensor accuracy and random uncertainties. While it is possible to clearly define initial conditions in the CFD simulation, experimental conditions, although carefully controlled, may vary to a small degree. For example, during the conducted experiments, it proved extremely difficult to position the robot at a stable position at absolute zero velocity.

6.4.3 Conclusion on comparison of experimental and CFD simulation

Experiments and CFD simulations are both important tools in understanding bio-inspired locomotion and developing efficient robotic systems. CFD simulations aim to achieve a high degree of accuracy and to be able to correctly predict the dynamics of the robot prototype and fluid structure interaction between the robot prototype and surrounding water.

A comparison is made between the applied CFD multi-body simulation and results of the hydrodynamic lab experiments. To make the comparison, the experimental measurements of Section 6.3.3.2 are repeated within the CFD multi-body simulation described in Section 3.2.3.

The discussion acknowledges the fundamental differences of the two approaches, such as the 2D simulation model versus the 3D experimental model, fully compliant joints versus joints with more complex magnetic coupling dynamics and a lack of consideration of electric motor and mechanical efficiencies within the CFD multi-body simulation. Further significant factors not accounted for in the CFD simulation are the elastic bending of the tail fin plate and the robots swimming location close to the surface, which is considered a free surface problem. A comparison of the whole data set of the parametric study shows an error between CFD and experimental data with linear progression.

The CFD simulation overpredicts the swimming velocity at the lower tested frequency and underpredicts the swimming velocity at the higher tested frequency. The lowest error between both approaches is achieved at medium frequencies for all combinations of amplitude and frequency. This suggests a common error.

A comparison between simulation and experiment of instantaneous velocities shows a poor agreement of the forward velocity, but a high degree of agreement for the lateral velocity. The results may suggest good performance of the magnetic joints by not showing significant delay between the two coupled modules. Recorded differences in forward swimming velocities may be explained by the difference in the rigidity of the caudal fin.

Overall, the largest observed simulation error predicted swimming velocity is +55% for low frequencies and negative 60% for high frequencies. At medium frequency, the velocity prediction error ranged between +/-10%. Current results are unsatisfactory and require improvement. The comparison may not factor the CFD simulation as being generally inaccurate because previous validation and testing has proven its accuracy. Rather, it highlights the challenges of modelling the complexity of physical systems. CFD modelling, prototyping and experimental testing share the common goal of advancing knowledge of autonomous propulsion yet put emphasis on different aspects. Overall, both methodologies complement each other and are important tools in furthering the understanding of fish locomotion and the creation of bio-inspired underwater vehicles. Future research shall assess the impact of the differences between both models, of which some may be neglectable.

Chapter 7 Thesis Conclusion and Future Work

Fish inspire scientists and engineers alike to study fish swimming and transfer knowledge into bio-inspired underwater robots with the aim to create superior vehicles in terms of efficiency, manoeuvrability, resilience and ability to adapt to complex environments. After more than a century of research into fish and fish locomotion, bio-inspired robots still fall short of their natural inspiration and a comprehensive understanding of fish locomotion remains to be contained behind the complex interplay of fluid structure interaction, fish physiology and behaviour.

In this study, numerical and experimental investigations are conducted to enhance the understanding of bio-inspired propulsion and manoeuvring. For both methodologies, contributions to knowledge are made. Ultimately, this work draws its strength from the wide range of applied methodologies reflecting the interdisciplinary nature of the research subject of bio-inspired autonomous underwater vehicles.

This thesis achieves all its initially set goals as set out in Section 1.5. In detail, chapter three describes and establishes CFD simulations coupled with a linear control algorithm. The ability to control a swimmer model within a CFD simulation enables simulating unsteady locomotion beyond traditional CFD simulations of flow over static geometries or fully prescribed kinematics. For a self-propelled swimmer, the swimming states may no longer be predetermined but adjusted by a closed feedback control loop. Chapter three continues to establish three control strategies by defining the feedback control error functions which are then applied in three numerical investigations in chapter four.

The three investigations in Chapter four focus on the optimal manoeuvring kinematics of BCF swimmers as well as an assessment of the thrust performance of an approximate elastic tail fin of different rigidities and an investigation into the station holding performance of a free-swimming elastic plate at different Reynolds numbers and distances to a cylinder in the wake.

Designing and building a bio-inspired underwater vehicle provides challenges distinctly different to numerical modelling and analysis. Chapter five describes the

design and construction of a new modular, bio-inspired underwater vehicle, which achieves static water tightness and true mechanical modularity through the novel application of synchronous magnetic couplings. The final presented design is a small size, fully 3D printed prototype of circa 1 meter length including a replaceable elastic tail fin.

Chapter six describes extensive hydrodynamic laboratory tests to test and assess the swimming performance of the created prototype. Buoyancy and ballasting tests are conducted, starting from the construction stage of the robot. Experimental measurements are taken for thrust and free-swimming trajectories. Thrust measurements are taken through a custom-made reversed bollard test stand for different actuation parameters and tail plate materials. The trajectories of the free-swimming robot for different kinematic parameters are recorded using a motion capturing system.

Overall, the created methodologies and platforms, numerical and experimental studies provide a great opportunity to be continued and extended in future research. The CFD simulations coupled with control may be extended, for instance, to a wider set of parameters and control strategies. The created bio-inspired robot platform provides high potential to be extended and refined, for example, to create and build a modular self-assembling robot or a robotic arm. A patent was submitted for the robot design which underlines its novelty and commercial potential.

Both general research questions are fundamental enough to maintain sufficient space for future research and may never be answered in their entirety. This work has attempted to contribute to answering the general research questions through investigations guided by the specific research questions also outlined in Section 1.5.

Section 4.1 investigated the optimal body curvature of a manoeuvring Body Caudal Fin swimmer. The investigation compared three curvature envelopes (linear increasing, linear decreasing and constant curvature) at three Reynolds numbers (2000, 1500, 1000). The numerical simulation results show an advantage of low head and high tail curvature for lowest power lowest radius turns. The curvature bias towards the tail increases the turning moment, reduces the counter turning moment over one

undulation cycle and maintains a head position in front of the passing fluid to create an additional positive turning moment creating surface pressure.

Future investigations may increase the parameter space and further look at quadratic or exponential curvature envelopes as investigated in amplitude envelope studies. Further, future studies may expand the investigation into turbulent flow at higher Reynolds numbers. Future work may investigate and compare experimental fish data against CFD data for a comprehensive study on animal behaviour.

Section 4.2 compared caudal fins with three different material stiffnesses and actuated with different pitching frequencies. Results indicate that softer materials show greater trailing edge deflection and their amplitude is more sensitive to frequency changes compared to harder materials. Hard materials maintain a steady amplitude across frequencies, while medium rigid materials increase in amplitude with higher frequencies, peaking at medium frequencies for the softest materials. The phase difference between leading and trailing edges reflects elastic displacement, with medium and soft materials showing larger deflections and wave-like behaviour. Medium rigid materials have the highest fluctuation in instantaneous body force, with higher frequencies resulting in greater thrust peaks and overall power expenditure; however, they generally consume less energy than soft and hard materials, performing better energetically. Future studies may be extended to a wider range of material properties and actuation parameters. Extending the study may also make it possible to draw a more general conclusion on the hydrodynamic performance.

Section 4.3 contributed results to answer the question on how a swimmer interacts with a bulk body located downstream during dynamic position holding. Results highlighted that the presence of a cylinder behind a bio-inspired swimmer reduces the drag on both the swimmer and the cylinder. The drag acting on the cylinder decreases until the plate is within 2 body lengths, then increases with closer distances. For a self-propelled swimmer, energy required to swim and hold position decreases as the distance to the cylinder decreases, with significant power drops when within 1 body length. Higher Reynolds numbers result in lower power expenditure, making them more energetically favourable, while closer distances to the cylinder slow convergence to a quasi-steady state and reduce the required amplitude for lower power. The interaction between the

low-pressure zone of the cylinder and the reversed vortex street of the plate explains the improved hydrodynamic performance. Future studies may expand the investigation to include materials of different properties and kinematic actuation parameters. Further, the bulk body may be represented by different geometries including fundamental geometric structures and geometries of real-world structures. Additionally, future studies may investigate the interaction of a swimmer and a bulk body at different relative positions, such as swimming in the wake or to the side of a bulk body. The current investigation is limited to flow assumed to be laminar, therefore, future studies may be extended into turbulent flow.

The experimental part of the study, starting in Chapter 5, consists of the design, construction and testing of a bio-inspired underwater prototype. Early in the design process the focus is put on a modular body caudal fin swimmer represented by discrete modules connected in series. The prototype is designed with a focus on optimal swimming performance, modularity and suitability for lab testing. Features to enable optimal swimming performance include a low drag slender design including low drag head module and continuous side surface to enable smooth fluid acceleration. Modularity is considered in the mechanical, electrical and software design. The magnetic joint design represents a key novelty that enables true mechanical modularity through magnetic torque transfer and without a fixed mechanical coupling between modules. Basic electronic modularity is achieved through common module design to create independent modules and redundancies throughout the robot. Guided by the electronic design, the robot is controlled and collects sensor data through Bluetooth communication between each module and a central PC.

Future designs may investigate different shapes and the addition of pectoral fins to further decrease drag and increase roll stability respectively. Also, the magnetic joint design may further mature, miniaturise and optimise to strengthen torque transmission and the inclusion of an active decoupling mechanism. A common electronic module structure may be maintained, however, each module may be specialised to house a certain internal or external operational function, such as sensors, data processing, and power storage. Modularity overall provides a strong path for future development to enable low cost, easy to deploy, recover and repair underwater vehicles. The

construction may be improved through application of different 3D printing methods and traditional material processing techniques. The robot may be enabled to dive through joint rotation, the addition of a joint degree of freedom or via hydrofoils acting as pectoral fins for down force lift. For a further matured design, lab testing may continue for hydrodynamic optimisation and may be enhanced with lab testing focussed on control and operation optimisation.

Chapter 6 describes extensive lab testing of the prototype, to assess its basic operating ability and swimming performance. Results show that the prototype fulfils all its functional objectives combined with excellent swimming performance.

The first investigation focusses on the thrust generation of the robot. An experimental parametric study is conducted comparing the thrust generation of different tailfins with different material stiffnesses. Results align with previous studies in literature that show an increasing frequency increases the generated thrust. Similarly, increasing amplitude at a constant frequency and tail material also boosts thrust. Tests with different tail fin materials revealed varied fluid structure interactions, with higher stiffness generally leading to improved thrust generation. Future studies may expand the tested material stiffness and kinematic parameters. In nature, flexible appendages are found in numerous different shapes and can be variable in stiffness. Future studies may consider the tail fin material, stiffness variation distribution and mechanisms in more detail. The applied methodology represents a sufficiently accurate and robust measurement methodology; however, it may be extended by measurement of the joint load angle to test the mechanical design of the prototype.

Free swimming tests assess the dynamic thrust and stability performance of the robot. After balancing, the robot has shown to swim stably and has the ability to manoeuvre stably throughout the lab testing tank. By continuing undulation around a curved central line, the robot is able to manoeuvre stably horizontally. Future investigations may extend the investigation across different kinematic parameters and may focus on the dynamic stability and its contribution to the swimming performance. The current prototype is remotely controlled; implementing sensors and autonomous control algorithms will be the next step in the development.

Acknowledging the challenges of measuring the efficiency of the prototype, a parametric study is conducted on the maximum swimming speed for varying amplitude magnitudes and frequencies with a constant amplitude envelope. Measurements show the robots ability to swim at fast speeds of up to 0.5 m/s which corresponds to around 0.5 body lengths per second. In accordance with the thrust measurements, an increase in frequency or amplitude results in increased velocities. Tests focused on a constant amplitude envelope mainly due its more stable swimming performance. Future investigations may expand the tested kinematic parameters and investigate different amplitude envelopes in terms of performance and swimming stability. Further, future investigations may include thrust enhancing or drag reducing measures, such as varying the caudal fin geometry and/or material and different module shapes respectively.

The final part of the thesis compares numerical and experimental results of a setup that corresponds to the free-swimming speed measurement described in section 6.3.3.2. Compared are the steady state velocity and instantaneous velocity of both methodologies. Overall, good agreement of the velocity magnitude is achieved, however, a comparison in terms of relative velocity may be considered poor. The comparison provides a discussion of the general differences of the methodologies and potential sources of mismatch. Future work may further align both methodologies by enhancing the numerical simulations to take details of the mechanical and electrical subsystem into account or put further emphasis on digital representation during the design and build process of the prototype. Future comparisons may be attempted, in particular in relation to the manoeuvring results in Section 4.1.

In conclusion, the author hopes the presented results prove useful to the scientific and engineering communities. The applied numerical and experimental methodologies have allowed for new investigations to support data generation and analysis of unsteady fish swimming. Further, created simulation methodologies and the robot prototype provide an excellent basis for future research work.

References

ACKERMAN, E. 2018. *MIT's Soft Robotic Fish Explores Reefs in Fiji* [Online]. IEEE Spectrum. Available: https://spectrum.ieee.org/mit-soft-robotic-fish-explores-reefs-in-fiji [Accessed 20/08/ 2024].

AKHTAR, I. & MITTAL, R. A biologically inspired computational study of flow past tandem flapping foils. 35th AIAA Fluid Dynamics Conference and Exhibit, 2005. 4760.

ANASTASIADIS, A., PAEZ, L., MELO, K., TYTELL, E. D., IJSPEERT, A. J. & MULLENERS, K. 2023. Identification of the trade-off between speed and efficiency in undulatory swimming using a bio-inspired robot. *Scientific Reports,* 13**,** 15032.

ANDERSON, J. M. & CHHABRA, N. K. 2002. Maneuvering and stability performance of a robotic tuna. *Integrative and comparative biology,* 42**,** 118-126.

ANSYS FLUENT 2021. Ansys Fluent Theory Guide *Theory Guide***,** 67.

ANYCUBIC. 2022. *ANYCUBIC Photon Mono* [Online]. Available: https://www.anycubic.com/products/photon-mono-resin-3d-printer [Accessed 02 2022].

ARASTEHFAR, S., CHEW, C.-M., JALALIAN, A., GUNAWAN, G. & YEO, K. S. 2019. A relationship between sweep angle of flapping pectoral fins and thrust generation. *Journal of Mechanisms and Robotics,* 11**,** 011014.

BARRETT, D. S. 1996. *Propulsive efficiency of a flexible hull underwater vehicle.* Massachusetts Institute of Technology.

BAYAT, B., CRESPI, A. & IJSPEERT, A. Envirobot: A bio-inspired environmental monitoring platform. 2016 Ieee/Oes Autonomous Underwater Vehicles (Auv), 2016. Ieee, 381-386.

BENNETT, S. 1993. Development of the PID controller. *IEEE Control Systems Magazine,* 13**,** 58-62.

BHALLA, A. P. S., BALE, R., GRIFFITH, B. E. & PATANKAR, N. A. 2013. A unified mathematical framework and an adaptive numerical method for fluid–structure interaction with rigid, deforming, and elastic bodies. *Journal of Computational Physics,* 250**,** 446-476.

BLAKE, R. 1977. On ostraciiform locomotion. *Journal of the Marine Biological Association of the United Kingdom,* 57**,** 1047-1055.

BLAKE, R. 2004. Fish functional design and swimming performance. *Journal of fish biology,* 65**,** 1193-1222.

BLAKE, R. & CHAN, K. 2006. Models of the turning and fast‐start swimming dynamics of aquatic vertebrates. *Journal of fish biology,* 69**,** 1824-1836.

BOYER, F., POREZ, M. & KHALIL, W. 2006. Macro-continuous computed torque algorithm for a three-dimensional eel-like robot. *IEEE transactions on robotics,* 22**,** 763-775.

BREDER, C. M. 1926. The locomotion of fishes. *Zoologica,* 4**,** 159-297.

BRITANNICA 2023. Tuna. *Britannica.* Britannica.

BRITANNICA 2023 Manta Ray. 2023: Britannica.

BRITANNICA 2024. Common Clown Fish. *In:* RAFFERTY JOHN P (ed.).

BUNGARTZ, H.-J., LINDNER, F., GATZHAMMER, B., MEHL, M., SCHEUFELE, K., SHUKAEV, A. & UEKERMANN, B. 2016. preCICE–a fully parallel library for multi-physics surface coupling. *Computers & Fluids,* 141**,** 250-258.

CARLING, J., WILLIAMS, T. L. & BOWTELL, G. 1998. Self-propelled anguilliform swimming: simultaneous solution of the two-dimensional Navier–Stokes equations and Newton's laws of motion. *Journal of experimental biology,* 201**,** 3143-3166.

CHA, Y., CHAE, W., KIM, H., WALCOTT, H., PETERSON, S. D. & PORFIRI, M. 2016. Energy harvesting from a piezoelectric biomimetic fish tail. *Renewable Energy,* 86**,** 449-458.

CHEN, B. & JIANG, H. 2019. Swimming performance of a tensegrity robotic fish. *Soft robotics,* 6**,** 520-531.

CHEN, Z. 2017. A review on robotic fish enabled by ionic polymer–metal composite artificial muscles. *Robotics and biomimetics,* 4**,** 24.

CHENNAREDDY, S., AGRAWAL, A. & KARUPPIAH, A. 2017. Modular self-reconfigurable robotic systems: a survey on hardware architectures. *Journal of Robotics,* 2017.

CHEW, C.-M., LIM, Q.-Y. & YEO, K. Development of propulsion mechanism for Robot Manta Ray. 2015 IEEE International Conference on Robotics and Biomimetics (ROBIO), 2015. IEEE, 1918-1923.

COMBES, S. A. & DANIEL, T. 2003. Flexural stiffness in insect wings I. Scaling and the influence of wing venation. *Journal of experimental biology,* 206**,** 2979-2987.

CORAL, W., ROSSI, C., CURET, O. M. & CASTRO, D. 2018. Design and assessment of a flexible fish robot actuated by shape memory alloys. *Bioinspiration & biomimetics,* 13**,** 056009.

CRESPI, A., BADERTSCHER, A., GUIGNARD, A. & IJSPEERT, A. J. 2005. AmphiBot I: an amphibious snake-like robot. *Robotics and Autonomous Systems,* 50**,** 163-175.

CRESPI, A. & IJSPEERT, A. J. AmphiBot II: An amphibious snake robot that crawls and swims using a central pattern generator. Proceedings of the 9th international conference on climbing and walking robots (CLAWAR 2006), 2006. 19-27.

CRESPI, A. & IJSPEERT, A. J. 2008. Online optimization of swimming and crawling in an amphibious snake robot. *IEEE Transactions on robotics,* 24**,** 75-87.

CRESPI, A., LACHAT, D., PASQUIER, A. & IJSPEERT, A. J. 2008. Controlling swimming and crawling in a fish robot using a central pattern generator. *Autonomous Robots,* 25**,** 3-13.

DE MOURA, C. A. & KUBRUSLY, C. S. 2013. The courant–friedrichs–lewy (cfl) condition. *AMC,* 10.

DENG, J., SHAO, X.-M. & YU, Z.-S. 2007. Hydrodynamic studies on two traveling wavy foils in tandem arrangement. *Physics of fluids,* 19**,** 113104.

DEWEY, P. & SMITS, A. 2023. Hydrodynamics of Manta Ray Pectoral Fin Propulsion. *Princeton, NJ, USA.*

DHONDT, G. 2017. Calculix crunchix user's manual version 2.12. *Munich, Germany, accessed Sept,* 21**,** 2017.

DI SANTO, V., GOERIG, E., WAINWRIGHT, D. K., AKANYETI, O., LIAO, J. C., CASTRO-SANTOS, T. & LAUDER, G. V. 2021. Convergence of undulatory swimming kinematics across a diversity of fishes. *Proceedings of the National Academy of Sciences,* 118.

DRUCKER, E. & LAUDER, G. 2001. Wake dynamics and fluid forces of turning maneuvers in sunfish. *Journal of Experimental Biology,* 204**,** 431-442.

DURAISAMY, K., IACCARINO, G. & XIAO, H. 2019. Turbulence modeling in the age of data. *Annual review of fluid mechanics,* 51**,** 357-377.

EELUME AS. 2023. *Reshaping underwater operations* [Online]. Available: https://eelume.com/ [Accessed 2023].

ELOY, C. 2013. On the best design for undulatory swimming. *Journal of Fluid Mechanics,* 717**,** 48-89.

EMSWORKS 2022. https://www.emworks.com/.

EPPS, B. P. & TECHET, A. H. 2007. Impulse generated during unsteady maneuvering of swimming fish. *Experiments in Fluids,* 43**,** 691-700.

EVOLOGICS GMBH 2023. BOSS project.

FARNELL, D. J., DAVID, T. & BARTON, D. 2004. Numerical simulations of a filament in a flowing soap film. *International Journal for Numerical Methods in Fluids,* 44**,** 313-330.

FERZIGER, J. H., PERIĆ, M. & STREET, R. L. 2019. *Computational methods for fluid dynamics*, springer.

FISH, F. E. 2002. Balancing requirements for stability and maneuverability in cetaceans. *Integrative and Comparative Biology,* 42**,** 85-93.

FISH, F. E., KOLPAS, A., CROSSETT, A., DUDAS, M. A., MOORED, K. W. & BART-SMITH, H. 2018. Kinematics of swimming of the manta ray: three-dimensional analysis of open-water maneuverability. *Journal of Experimental Biology,* 221**,** jeb166041.

GAO, A. & TRIANTAFYLLOU, M. S. 2018. Independent caudal fin actuation enables high energy extraction and control in two-dimensional fish-like group swimming. *Journal of Fluid Mechanics,* 850**,** 304-335.

GERSTNER, C. L. 1999. Maneuverability of four species of coral-reef fish that differ in body and pectoral-fin morphology. *Canadian Journal of Zoology,* 77**,** 1102-1110.

GLUSHKO, I., OLENEW, E., KOMAR, M., KNIESE, L., SOKOLOVSKYI, R., KEBKAL, O., BANNASCH, R. & KEBKAL, K. Software control architecture for the BOSS Manta Ray AUV actuation system. 2018 IEEE/OES Autonomous Underwater Vehicle Workshop (AUV), 2018. IEEE, 1-5.

GÓMEZ, J. G. 2008. Modular robotics and locomotion: application to limbless robots. *Pdd. Universidad Autonoma de Madrid. Madrid,* 42.

GOODING, R. M., NEIL, W. H. & DIZON, A. E. 1981. SKIPJACK TUNA, KATSUWONUS PELAMIS. *Fishery Bulletin,* 79**,** 31.

GRAY, J. 1933. Directional control of fish movement. *Proceedings of the Royal Society of London. Series B, Containing Papers of a Biological Character,* 113**,** 115-125.

GUIZZO, E. 2013. *HiBot Demos New Amphibious Snake Robot* [Online]. Available: https://spectrum.ieee.org/hibot-demos-new-amphibious-snake-robot [Accessed 20/08/ 2024].

HAN, J. 2009. From PID to active disturbance rejection control. *IEEE transactions on Industrial Electronics,* 56**,** 900-906.

HESS, A., TAN, X. & GAO, T. 2020. CFD-based multi-objective controller optimization for soft robotic fish with muscle-like actuation. *Bioinspiration & biomimetics,* 15**,** 035004.

HESS, F. Bending moments and muscle power in swimming fish. Proc. 8th Australasian Fluid Mechanics Conference, 1983. 12A.

HOAR, W. & RANDALL, D. 1978. Fish physiology. Locomotion, vol VII. *Academic Press, New York*.

HU, H., LIU, J., DUKES, I. & FRANCIS, G. Design of 3D swim patterns for autonomous robotic fish. 2006 IEEE/RSJ International Conference on Intelligent Robots and Systems, 2006. IEEE, 2406-2411.

HU, J. 2016. *Numerical study on hydrodynamic performance of bio-mimetic locomotion.* http://purl.org/coar/resource_type/c_db06.

HU, J., XIAO, Q. & LI, R. 2021. Numerical simulation of a multi-body system mimicking coupled active and passive movements of fish swimming. *Journal of Marine Science and Engineering,* 9**,** 334.

HUANG, W.-X. & TIAN, F.-B. 2019. Recent trends and progress in the immersed boundary method. *Proceedings of the Institution of Mechanical Engineers, Part C: Journal of Mechanical Engineering Science,* 233**,** 7617-7636.

IJSPEERT, A. J. 2008. Central pattern generators for locomotion control in animals and robots: a review. *Neural networks,* 21**,** 642-653.

IJSPEERT, A. J. 2014. Biorobotics: Using robots to emulate and investigate agile locomotion. *science,* 346**,** 196-203.

IJSPEERT, A. J., CRESPI, A., RYCZKO, D. & CABELGUEN, J.-M. 2007. From swimming to walking with a salamander robot driven by a spinal cord model. *science,* 315**,** 1416-1420.

JINDRICH, D. L. & FULL, R. J. 1999. Many-legged maneuverability: dynamics of turning in hexapods. *Journal of experimental biology,* 202**,** 1603-1623.

JONES, G. P., PLANES, S. & THORROLD, S. R. 2005. Coral reef fish larvae settle close to home. *Current biology,* 15**,** 1314-1318.

KAJTAR, J. B. & MONAGHAN, J. J. 2010. On the dynamics of swimming linked bodies. *European Journal of Mechanics-B/Fluids,* 29**,** 377-386.

KATZSCHMANN, R. K., DELPRETO, J., MACCURDY, R. & RUS, D. 2018. Exploration of underwater life with an acoustically controlled soft robotic fish. *Science Robotics,* 3**,** eaar3449.

KATZSCHMANN, R. K., MARCHESE, A. D. & RUS, D. Hydraulic autonomous soft robotic fish for 3D swimming. Experimental Robotics: The 14th International Symposium on Experimental Robotics, 2015. Springer, 405-420.

KELASIDI, E., KOHL, A. M., PETTERSEN, K. Y., HOFFMANN, B. & GRAVDAHL, J. T. 2018. Experimental investigation of locomotion efficiency and path-following for underwater snake robots with and without a caudal fin. *Annual Reviews in Control,* 46**,** 281-294.

KELASIDI, E., LILJEBÄCK, P., PETTERSEN, K. Y. & GRAVDAHL, J. T. 2015. Experimental investigation of efficient locomotion of underwater snake robots for lateral undulation and eel-like motion patterns. *Robotics and Biomimetics,* 2**,** 1-27.

KELASIDI, E., PETTERSEN, K. Y., GRAVDAHL, J. T. & LILJEBÄCK, P. Modeling of underwater snake robots. 2014 IEEE International Conference on Robotics and Automation (ICRA), 2014. IEEE, 4540-4547.

KERN, S. & KOUMOUTSAKOS, P. 2006. Simulations of optimized anguilliform swimming. *Journal of Experimental Biology,* 209**,** 4841-4857.

KHALIL, W., GALLOT, G. & BOYER, F. 2007. Dynamic modeling and simulation of a 3-D serial eel-like robot. *IEEE Transactions on Systems, Man, and Cybernetics, Part C (Applications and Reviews),* 37**,** 1259-1268.

KOOCHESFAHANI, M. M. 1989. Vortical patterns in the wake of an oscillating airfoil. *AIAA journal,* 27**,** 1200-1205.

KORSMEYER, K. E., STEFFENSEN, J. F. & HERSKIN, J. 2002. Energetics of median and paired fin swimming, body and caudal fin swimming, and gait transition in parrotfish (Scarus schlegeli) and triggerfish (Rhinecanthus aculeatus). *Journal of experimental biology,* 205**,** 1253-1263.

LACHAT, D., CRESPI, A. & IJSPEERT, A. J. BoxyBot: a swimming and crawling fish robot controlled by a central pattern generator. The First IEEE/RAS-EMBS International Conference on Biomedical Robotics and Biomechatronics, 2006. BioRob 2006., 2006. IEEE, 643-648.

LEE, D. & YANNAKAKIS, M. 1996. Principles and methods of testing finite state machines-a survey. *Proceedings of the IEEE,* 84**,** 1090-1123.

LETIER, P., YAN, X. T., DEREMETZ, M., BIANCO, A., GRUNWALD, G., ROA, M., KRENN, R., ARANCÓN, M. M., DISSAUX, P. & CASARRUBIOS, J. S. G. MOSAR: Modular spacecraft assembly and reconfiguration demonstrator. 15th Symposium on Advanced Space Technologies in Robotics and Automation, 2019.

LI, L., LIU, A., WANG, W., RAVI, S., FU, R., YU, J. & XIE, G. 2019. Bottom-level motion control for robotic fish to swim in groups: modeling and experiments. *Bioinspiration & biomimetics,* 14**,** 046001.

LI, L., RAVI, S., XIE, G. & COUZIN, I. D. 2021. Using a robotic platform to study the influence of relative tailbeat phase on the energetic costs of side-by-side swimming in fish. *Proceedings of the Royal Society A,* 477**,** 20200810.

LI, R., XIAO, Q., LIU, Y., HU, J., LI, L., LI, G., LIU, H., HU, K. & WEN, L. 2018. A multi-body dynamics based numerical modelling tool for solving aquatic biomimetic problems. *Bioinspiration & biomimetics,* 13**,** 056001.

LI, Y., XU, Y., WU, Z., MA, L., GUO, M., LI, Z. & LI, Y. 2022. A comprehensive review on fish-inspired robots. *International Journal of Advanced Robotic Systems,* 19**,** 17298806221103707.

LIAO, J. C. 2022. Fish swimming efficiency. *Current Biology,* 32**,** R666-R671.

LIAO, J. C., BEAL, D. N., LAUDER, G. V. & TRIANTAFYLLOU, M. S. 2003. The Kármán gait: novel body kinematics of rainbow trout swimming in a vortex street. *Journal of experimental biology,* 206**,** 1059-1073.

LIGHTHILL, M. 1960. Note on the swimming of slender fish. *Journal of fluid Mechanics,* 9**,** 305-317.

LIGHTHILL, M. J. 1971. Large-amplitude elongated-body theory of fish locomotion. *Proceedings of the Royal Society of London. Series B. Biological Sciences,* 179**,** 125-138.

LILJEBÄCK, P. & MILLS, R. Eelume: A flexible and subsea resident IMR vehicle. Oceans 2017-Aberdeen, 2017. IEEE, 1-4.

LILJEBÄCK, P., PETTERSEN, K. Y., STAVDAHL, Ø. & GRAVDAHL, J. T. 2013. *Snake robots: modelling, mechatronics, and control*, Springer.

LILJEBÄCK, P., STAVDAHL, Ø., PETTERSEN, K. Y. & GRAVDAHL, J. T. Mamba-A waterproof snake robot with tactile sensing. 2014 IEEE/RSJ International Conference on Intelligent Robots and Systems, 2014. IEEE, 294-301.

LIN, Z., HESS, A., YU, Z., CAI, S. & GAO, T. 2019. A fluid–structure interaction study of soft robotic swimmer using a fictitious domain/active-strain method. *Journal of Computational Physics,* 376**,** 1138-1155.

LIU, J., ZHANG, X. & HAO, G. 2016. Survey on research and development of reconfigurable modular robots. *Advances in Mechanical Engineering,* 8**,** 1687814016659597.

LOW, K. Current and future trends of biologically inspired underwater vehicles. 2011 Defense Science Research Conference and Expo (DSR), 2011. IEEE, 1-8.

LU, B., WANG, J., ZOU, Q., FAN, J. & ZHOU, C. 2023. Towards Power Cost Analysis and Optimization of a Multi-Flexible Robotic Fish. *Available at SSRN 4405120*.

LUO, Y. 2021. A numerical study of fin and jet propulsions involving fluid-structure interactions.

LUO, Y., WRIGHT, M., XIAO, Q., YUE, H. & PAN, G. 2021. Fluid–structure interaction analysis on motion control of a self-propelled flexible plate near a rigid body utilizing PD control. *Bioinspiration & Biomimetics,* 16**,** 066002.

LUO, Y., XIAO, Q. & SHI, G. 2020. A Fluid–Structure Interaction Study on a Bionic Fish Fin With Non-Uniform Stiffness Distribution. *Journal of Offshore Mechanics and Arctic Engineering,* 142.

MA, S., ZHAO, Q., DING, M., ZHANG, M., ZHAO, L., HUANG, C., ZHANG, J., LIANG, X., YUAN, J., WANG, X. & HE, G. 2023. A Review of Robotic Fish Based on Smart Materials. *Biomimetics,* 8**,** 227.

MAERTENS, A., TRIANTAFYLLOU, M. S. & YUE, D. K. 2015. Efficiency of fish propulsion. *Bioinspiration & biomimetics,* 10**,** 046013.

MAERTENS, A. P., GAO, A. & TRIANTAFYLLOU, M. S. 2017. Optimal undulatory swimming for a single fish-like body and for a pair of interacting swimmers. *Journal of Fluid Mechanics,* 813**,** 301-345.

MAERTENS, A. P. & WEYMOUTH, G. D. 2015. Accurate Cartesian-grid simulations of near-body flows at intermediate Reynolds numbers. *Computer Methods in Applied Mechanics and Engineering,* 283**,** 106-129.

MATHWORKS INC. 2023. MATLAB 2023b.

MATWEB. 2023. *Material Property Data* [Online]. Available: https://www.matweb.com/ [Accessed].

MINTCHEV, S., STEFANINI, C., GIRIN, A., MARRAZZA, S., OROFINO, S., LEBASTARD, V., MANFREDI, L., DARIO, P. & BOYER, F. An underwater reconfigurable robot with bioinspired electric sense. 2012 IEEE international conference on robotics and automation, 2012. IEEE, 1149-1154.

MITTAL, R. & IACCARINO, G. 2005. Immersed boundary methods. *Annu. Rev. Fluid Mech.,* 37**,** 239-261.

MJAAVATTEN, A. 2021. Curvature of a 1D curve in a 2D or 3D space. *MATLAB Central File Exchange Retrieved July,* 10**,** 2023.

MORISON, J., JOHNSON, J. W. & SCHAAF, S. A. 1950. The force exerted by surface waves on piles. *Journal of Petroleum Technology,* 2**,** 149-154.

MOUNTCASTLE, A. M. & COMBES, S. A. 2013. Wing flexibility enhances load-lifting capacity in bumblebees. *Proceedings of the Royal Society B: Biological Sciences,* 280**,** 20130531.

MUNFORD, P. & NORMAND, P. 2016. *Mastering Autodesk Inventor 2016 and Autodesk Inventor LT 2016: Autodesk Official Press,* John Wiley & Sons.

NAGRIAL, M. H., RIZK, J. & HELLANY, A. 2011. Design of synchronous torque couplers. *World Academy of Science, Engineering and Technology,* 79**,** 426-431.

NATASHAH HITTI. 2023. *MantaDroid offers "graceful" alternative to existing underwater robots* [Online]. Dezeen. Available:

https://www.dezeen.com/2017/12/07/mantadroid-manta-ray-robot-autonomous-underwater-vehicles-design-technology/ [Accessed 2023].

PARAZ, F., ELOY, C. & SCHOUVEILER, L. 2014. Experimental study of the response of a flexible plate to a harmonic forcing in a flow. *Comptes Rendus Mécanique,* 342**,** 532-538.

PARRA RUBIO, A., FAN, D., JENETT, B., DEL ÁGUILA FERRANDIS, J., TOURLOMOUSIS, F., ABDEL-RAHMAN, A., PREISS, D., ZEMÁNEK, J., TRIANTAFYLLOU, M. & GERSHENFELD, N. 2023. Modular Morphing Lattices for Large-Scale Underwater Continuum Robotic Structures. *Soft Robotics,* 10**,** 724-736.

PAVLOV, V., ROSENTAL, B., HANSEN, N. F., BEERS, J. M., PARISH, G., ROWBOTHAM, I. & BLOCK, B. A. 2017. Hydraulic control of tuna fins: A role for the lymphatic system in vertebrate locomotion. *Science,* 357**,** 310-314.

PESKIN, C. S. 1972. Flow patterns around heart valves: a numerical method. *Journal of computational physics,* 10**,** 252-271.

PILIANTENERGY. 2023. *Velox - Piliant Energy* [Online]. Available: https://www.pliantenergy.com/robotics [Accessed 07/11 2023].

POREZ, M., BOYER, F. & IJSPEERT, A. J. 2014. Improved Lighthill fish swimming model for bio-inspired robots: Modeling, computational aspects and experimental comparisons. *The International Journal of Robotics Research,* 33**,** 1322-1341.

QUALISYS. *Improving efficiency and maneuverability of underwater vehicles* [Online]. Qualisys Available: https://www.qualisys.com/stories/robotics-underwater-research-at-ntnu/ [Accessed 20/08/ 2024].

RAISSI, M., PERDIKARIS, P. & KARNIADAKIS, G. E. 2019. Physics-informed neural networks: A deep learning framework for solving forward and inverse problems involving nonlinear partial differential equations. *Journal of Computational physics,* 378**,** 686-707.

RAJENDRAN, S. K. & ZHANG, F. 2022. Design, Modeling, and Visual Learning-Based Control of Soft Robotic Fish Driven by Super-Coiled Polymers. *Frontiers in Robotics and AI,* 8**,** 431.

RANADE, R., HILL, C. & PATHAK, J. 2021. DiscretizationNet: A machine-learning based solver for Navier–Stokes equations using finite volume discretization. *Computer Methods in Applied Mechanics and Engineering,* 378**,** 113722.

RANDENI, S., SACARNY, M., BENJAMIN, M. & TRIANTAFYLLOU, M. 2022. Morpheus: An A-sized AUV with morphing fins and algorithms for agile maneuvering. *arXiv preprint arXiv:2212.11692*.

READ, D. A., HOVER, F. & TRIANTAFYLLOU, M. 2003. Forces on oscillating foils for propulsion and maneuvering. *Journal of Fluids and Structures,* 17**,** 163-183.

REZAPOUR, E., PETTERSEN, K. Y., LILJEBÄCK, P., GRAVDAHL, J. T. & KELASIDI, E. 2014. Path following control of planar snake robots using virtual holonomic constraints: theory and experiments. *Robotics and biomimetics,* 1**,** 1-15.

ROHR, J. J. & FISH, F. E. 2004. Strouhal numbers and optimization of swimming by odontocete cetaceans. *Journal of Experimental Biology,* 207**,** 1633-1642.

SALAZAR, R., FUENTES, V. & ABDELKEFI, A. 2018. Classification of biological and bioinspired aquatic systems: A review. *Ocean Engineering,* 148**,** 75-114.

SCARADOZZI, D., PALMIERI, G., COSTA, D. & PINELLI, A. 2017. BCF swimming locomotion for autonomous underwater robots: a review and a novel solution to improve control and efficiency. *Ocean Engineering,* 130**,** 437-453.

SCHOLANDER, P. 1959. Wave-riding dolphins: How do they do it? At present only the dolphin knows the answer to this free-for-all in hydrodynamics. *Science,* 129**,** 1085-1087.

SCHOMBURG, W. K., REINERTZ, O., SACKMANN, J. & SCHMITZ, K. 2020. Equations for the approximate calculation of forces between cuboid magnets. *Journal of Magnetism and Magnetic Materials,* 506**,** 166694.

SFAKIOTAKIS, M., LANE, D. M. & DAVIES, J. B. C. 1999. Review of fish swimming modes for aquatic locomotion. *IEEE Journal of oceanic engineering,* 24**,** 237-252.

SHELL, H. R. 2012. Cinehistory and experiments on film. *Journal of Visual Culture,* 11**,** 288-306.

SHINTAKE, J., CACUCCIOLO, V., SHEA, H. & FLOREANO, D. 2018. Soft biomimetic fish robot made of dielectric elastomer actuators. *Soft robotics,* 5**,** 466-474.

SHULER, S. W., NEHRING, R. B. & FAUSCH, K. D. 1994. Diel habitat selection by brown trout in the Rio Grande River, Colorado, after placement of boulder structures. *North American Journal of Fisheries Management,* 14**,** 99-111.

SONG, Z., MARBURG, A. & MANALANG, D. 2020. Resident subsea robotic systems: A review. *Marine Technology Society Journal,* 54**,** 21-31.

SPAGNOLIE, S. E., MORET, L., SHELLEY, M. J. & ZHANG, J. 2010. Surprising behaviors in flapping locomotion with passive pitching. *Physics of Fluids,* 22.

STEFANINI, C., OROFINO, S., MANFREDI, L., MINTCHEV, S., MARRAZZA, S., ASSAF, T., CAPANTINI, L., SINIBALDI, E., GRILLNER, S. & WALLEN, P. A compliant bioinspired swimming robot with neuro-inspired control and autonomous behavior. 2012 IEEE International Conference on Robotics and Automation, 2012. IEEE, 5094-5098.

STRUEBIG, K., BAYAT, B., ECKERT, P., LOOIJESTIJN, A., LUETH, T. C. & IJSPEERT, A. J. 2020. Design and development of the efficient anguilliform swimming robot—MAR. *Bioinspiration & Biomimetics,* 15**,** 035001.

TAN, X., CARPENTER, M., THON, J. & ALEQUIN-RAMOS, F. Analytical modeling and experimental studies of robotic fish turning. 2010 IEEE International Conference on Robotics and Automation, 2010. IEEE, 102-108.

TIAN, R., LI, L., WANG, W., CHANG, X., RAVI, S. & XIE, G. 2020. CFD based parameter tuning for motion control of robotic fish. *Bioinspiration & Biomimetics,* 15**,** 026008.

TOKIĆ, G. & YUE, D. K. 2012. Optimal shape and motion of undulatory swimming organisms. *Proceedings of the Royal Society B: Biological Sciences,* 279**,** 3065-3074.

TOLKOFF, S. W. 1999. *Robotics and power measurements of the RoboTuna.* Massachusetts Institute of Technology.

TRIANTAFYLLOU, M. S. & TRIANTAFYLLOU, G. S. 1995. An efficient swimming machine. *Scientific american,* 272**,** 64-70.

TYTELL, E. D. & LAUDER, G. V. 2004. The hydrodynamics of eel swimming: I. Wake structure. *Journal of Experimental Biology,* 207**,** 1825-1841.

UEKERMANN, B., BUNGARTZ, H.-J., YAU, L. C., CHOURDAKIS, G. & RUSCH, A. Official preCICE adapters for standard open-source solvers. Proceedings of the 7th GACM colloquium on computational mechanics for young scientists from academia, 2017.

WALKER, J. A. 2000. Does a rigid body limit maneuverability? *Journal of Experimental Biology,* 203**,** 3391-3396.

WANG, J., JIANG, Z., YANG, Y. & HU, W. A Review on Bio-inspired Fluid Mechanics via Deep Reinforcement Learning. International Conference on Bio-Inspired Computing: Theories and Applications, 2022. Springer, 290-304.

WANG, R., WANG, S., WANG, Y., CHENG, L. & TAN, M. 2020. Development and motion control of biomimetic underwater robots: A survey. *IEEE Transactions on Systems, Man, and Cybernetics: Systems,* 52**,** 833-844.

WEBB, P. W. & WEIHS, D. 2015. Stability versus maneuvering: challenges for stability during swimming by fishes. *Integrative and Comparative Biology,* 55**,** 753-764.

WEIHS, D. 1972. A hydrodynamical analysis of fish turning manoeuvres. *Proceedings of the Royal Society of London. Series B. Biological Sciences,* 182**,** 59-72.

WEIHS, D. 1973. Hydromechanics of fish schooling. *Nature,* 241**,** 290-291.

WOLF, Z. & LAUDER, G. V. 2022. A Fish-Like Soft-Robotic Model Generates a Diversity of Swimming Patterns. *Integrative and Comparative Biology,* 62**,** 735-748.

WRIGHT, M., GORMA, W., LUO, Y., POST, M., XIAO, Q. & DURRANT, A. Multi-actuated AUV body for windfarm inspection: lessons from the bio-inspired RoboFish field trials. 2020 IEEE/OES Autonomous Underwater Vehicles Symposium (AUV), 2020a. IEEE, 1-6.

WRIGHT, M., LUO, Y., XIAO, Q., POST, M., GORMA, W., DURRANT, A. & YUE, H. CFD-FSI analysis on motion control of bio-inspired underwater AUV system utilizing PID control. 2020 IEEE/OES Autonomous Underwater Vehicles Symposium (AUV), 2020b. IEEE, 1-6.

WRIGHT, M., XIAO, Q., SAISHUAI, D., HONG, Y., MARK, P. & BODHI, S. 2023a. Design and Development of Modular Magnetic Bio-Inspired Autonomous Underwater Robot – MMBAUV. *Ocean Engineering*.

WRIGHT, M., XIAO, Q. & ZHU, Q. 2023b. Combined hydrodynamic and control analysis on optimal kinematic parameters for bio-inspired autonomous underwater vehicle manoeuvring. *Frontiers in Physics,* 11.

WU, J., SHU, C. & ZHAO, N. 2014. Numerical study of flow control via the interaction between a circular cylinder and a flexible plate. *Journal of Fluids and Structures,* 49**,** 594-613.

WU, T. Y.-T. 1971a. Hydromechanics of swimming propulsion. Part 1. Swimming of a two-dimensional flexible plate at variable forward speeds in an inviscid fluid. *Journal of Fluid Mechanics,* 46**,** 337-355.

WU, T. Y.-T. 1971b. Hydromechanics of swimming propulsion. Part 2. Some optimum shape problems. *Journal of Fluid Mechanics,* 46**,** 521-544.

WU, T. Y.-T. 1971c. Hydromechanics of swimming propulsion. Part 3. Swimming and optimum movements of slender fish with side fins. *Journal of fluid mechanics,* 46**,** 545-568.

YEN, T. & AZWADI, C. N. 2015. A review: the development of flapping hydrodynamics of body and caudal fin movement Fishlike structure. *Journal of Advanced Review on Scientific Research,* 8**,** 19-38.

YU-HSIANG, L., SIDDALL, R., SCHWAB, F., FUKUSHIMA, T., BANERJEE, H., BAEK, Y., VOGT, D., PARK, Y.-L. & JUSUFI, A. 2023. Modeling and Control of a Soft Robotic Fish with Integrated Soft Sensing. *Advanced Intelligent Systems,* 5.

YU, J., LIU, L., WANG, L., TAN, M. & XU, D. 2008. Turning control of a multilink biomimetic robotic fish. *IEEE Transactions on Robotics,* 24**,** 201-206.

YU, S., MA, S., LI, B. & WANG, Y. An amphibious snake-like robot: Design and motion experiments on ground and in water. 2009 International Conference on Information and Automation, 2009. IEEE, 500-505.

ZENG, Y., WANG, Y., YANG, D. & CHEN, Q. 2023. Immersed Boundary Methods for Simulations of Biological Flows in Swimming and Flying Bio-Locomotion: A Review. *Applied Sciences,* 13**,** 4208.

ZHANG, D., PAN, G., CHAO, L. & ZHANG, Y. 2018. Effects of Reynolds number and thickness on an undulatory self-propelled foil. *Physics of Fluids*, 30**,** 071902.

ZIEGLER, J. G. & NICHOLS, N. B. 1942. Optimum settings for automatic controllers. *Transactions of the American society of mechanical engineers,* 64**,** 759-765.

Appendix

Web link to Case and UDF files Section 3.1 single body simulation:

https://github.com/marvinwright/Single_body_case_and_UDF/tree/feff18de734ab9a395bc8fd5364a3471d8aa4fb8/simulation%20files